
ALMA MATER STUDIORUM - UNIVERSITÀ DI BOLOGNA
CAMPUS DI CESENA
SCUOLA DI INGEGNERIA E ARCHITETTURA

CORSO DI LAUREA MAGISTRALE IN INGEGNERIA BIOMEDICA

TITOLO DELLA TESI

**UNCERTAINTIES ANALYSIS OF
DIGITAL VOLUME CORRELATION MEASUREMENTS FOR
SYNCHROTRON-BASED TOMOGRAPHIC IMAGES OF BONE**

Tesi in

Meccanica Dei Tessuti Biologici Lm

Relatore

Prof. Luca Cristofolini

Presentata da

Comini Federica

Correlatore

Dr. Enrico Dall'Ara

Anno Accademico 2016/2017

Acknowledgements

I would like to acknowledge my supervisor Prof. Luca Cristofolini for the opportunity and for his advice during the writing of this thesis. I would like also to thank Dr. Enrico Dall'Ara of the University of Sheffield for his constantly help, guidance and support. His knowledge and motivation taught me how to deal with the difficulties that may be encountered during the research work.

My sincere thanks also go to the University of Sheffield members, in particular, to the experts who gave me technical support for this research thesis: Dr. Will Furnass, Mr. Will Griffiths and Mr. Ben Hughes. I'm grateful to Dr. Mario Giorgi for helping me with the DVC analysis and to Dr. Pinaki Bhattacharya for sharing his data.

Abstract

The evaluation of the heterogeneity of the strain inside the bone tissue is important for assessing the effect of bone pathologies and interventions and for validating computational models. Digital Volume Correlation (DVC) has been proved to be a powerful technique to measure internal displacement and strain field in bone. Recent studies have shown that the synchrotron radiation micro-computed tomography (SR-microCT) can improve the accuracy of the DVC but only zero-strain or virtually-moved test have been used to quantify the DVC uncertainties, leading to potential underestimation of the measurement errors. In this study, for the first time, the uncertainties of a global DVC approach have been evaluated on virtually deformed repeated images to account for the image noise and for a known applied deformation. Virtually-deformed tests have been carried out from repeated SR-microCT scan of bovine cortical bone specimens with a nominal resolution of 1.6 μm . Different levels and directions of deformation have been simulated and the strain fields have been computed with the Sheffield Image Registration Toolkit (ShIRT) combined with a finite element software package. The amount and distribution of the errors for each component of strain have been evaluated. The analysis showed that systematic and random errors of the normal strain components along the deformation direction were higher than the errors in the components at zero strain. The estimated systematic error, for 1% of nominal compression, was approximately 10% of the nominal applied deformation, while the random errors ranged between 10 and 15%. Higher errors have been localized in the boundary of the volumes of interest, perpendicular to the deformation direction. When 120 μm of the edge were removed from the analysis, the systematic and random errors have been reduced to approximately 6% and 7% of the applied deformation. In conclusion, when this technique is used, all the sources of errors need to be considered and, for each application, an optimization of the registration and post-processing parameters of the DVC analyses is suggested. To complete the evaluation of the DVC uncertainties, future studies should use the method presented here but applying a realistic heterogeneous strain field.

Contents

1. Introduction	3
1.1. Bone	5
1.1.1. Bone composition	5
1.1.2. Bone microscopic and macroscopic structure	6
1.2. Morphological analysis	10
1.2.1. Micro Computed Tomography (Micro-CT)	10
1.2.2. Synchrotron radiation micro-CT (SR micro-CT)	12
1.3. Strain measurements in bone	14
1.4. DVC applications	18
1.5. DVC accuracy and precision	19
1.6. Study aims	23
2. Materials and methods	24
2.1 Specimens and SR micro-CT	24
2.2 Image processing	25
2.2.1 Uniaxial deformations	26
2.2.2 Composed deformations	28
2.3 DVC protocol	28
2.4 Uncertainties analysis	32
3. Results	37
3.1 Frequency plot	37
3.2 Systematic errors	45
3.3 Random errors	48
3.4 Scalar indicators	51
3.5 Systematic and random errors for different nodal spacing	53
3.6 Spatial distribution of the errors	55
3.7 Effect of the edge	59
3.8 Composed deformation	66
4. Discussion	68
4.1 Limitations and potentials future works	77
5. Conclusion	78
Appendix	79

1. Introduction

Musculoskeletal pathologies, such as osteoporosis, osteoarthritis and bone metastases are related to the bone fracture risk. One of the main aims of bone research is to assess the risks of fracture in bone and to prevent their occurrence. The bone is a complex heterogeneous and anisotropic material and it is a result of a structural optimization, especially from the mechanical point of view (Cristofolini, 2015). Bone structure can resist complex physiological loading and regulate its mechanical resistance through remodelling.

The information of the full field strain in the bone at the organ and tissue level is important from the clinical point of view for many reasons. First, it is known that mechanical and physiological environment have a strong influence in bone remodelling. In fact, changes in bone tissue structure, shape and composition are driven by the amount and distribution of strain (Lanyon et al., 1996; Petrtyl and Danesova, 1999; Rosa et al., 2015). Moreover, the knowledge of internal strain can be useful to understanding the potential pathogenesis of bone fractures (Hussein et al. 2012; Christen et al.,2012). Furthermore, the evaluation of the bone strain and fractures mechanism at the local level may help to generate strategies for prevention and treatment (Cowen, 2001; Danesi et al., 2016).

The finite element method (FEM) is a computational technique which can be used to solve the biomedical engineering problems. In recent years, in order to estimate the bone fracture risk, these computational models have been used to predict the bone mechanical properties (Bessho et al., 2007; Falcinelli et al., 2016). However, FEM verification and validation are fundamental as their output can be considered to have any clinical value (Viceconti, 2005). Validation of these computational models is usually performed only on apparent properties of the bone (e.g. stiffness and strength) which are much easier to test than the local ones.

Experimental measurements of local bone strains are needed for assessing the effect of pathologies and interventions and for validating computational models. Different techniques, such as strain gauges or digital image correlation (DIC), have been used to evaluate the strains on bone at organ- and tissue-level (Grassi and Isaksson, 2015). However, these methods offer measures only on the external surface. Digital

Volume Correlation (DVC) is a technique introduced by Bay and colleagues in the 1999 to measure displacement and strain inside the bone (Bay et al., 1999). They described this method as the three-dimensional extension of the DIC. To date, the implementation of the DVC is not unique and different algorithms have been proposed (Roberts et al., 2014). High-resolution X-ray Computed Tomography, or micro-CT, images of the bone are typically used in the correlation algorithm. These types of images allow the internal microarchitecture to be visualized, with resolutions at micrometre level. The DVC is based on tracking the displacement of the microstructural features within image volumes from two scans of the same bone sample, in both unloaded and loaded state (Grassi and Isaksson, 2015). The strain measurements are then computed from the displacements field by differentiation.

Many applications of the DVC to measure displacement and strain inside bone structures and biomaterials are reported in the literature so far (Bay et al., 1999; Liu and Morgan, 2007; Bay et al., 2008; Hussein et al., 2012; Madi et al., 2013; Gillard et al., 2014; Danesi et al., 2016; Palanca et al., 2016; Zhu et al., 2016; Tozzi et al., 2017). Recently, some studies have qualitatively compared the full field displacement and strain measurements of the DVC to same quantities predicted by the FE models generated for the same bones (Zauel et al., 2006; Jackman et al., 2016; Chen et al., 2017; Costa et al., 2017). Still low accuracy and precision is achieved for strain measures at the level of a single bone structural unit. For this reason, a direct comparison between measurements from the FE models to DVCs could be performed only for the displacement field (Chen et al., 2017; Costa et al., 2017). However, as the bone fails after a certain level of strain, the prediction of local strain becomes fundamental and an accurate DVC method is needed to evaluate the heterogeneity of the strain inside the bone, even at a local level. Two recent studies reported that high-resolution images, based on synchrotron radiation (SR micro-CT), can improve the accuracy and precision of the DVC displacement and strain measurements (Christen et al., 2012; Palanca et al., 2017). However, the estimation of DVC precision in strain measurements is usually based only on a specific case of zero-strain condition and it remains to be investigated what DVC precision and accuracy can be obtained under load.

1.1. Bone

The bone tissue is the main constituent of the skeleton and it differs from other connective tissues for mineralization of the extracellular matrix. Two types of bone tissue can be distinguished: cortical and trabecular bone which differ mainly in terms of development, density, architecture, function, proximity to the bone marrow, blood supply, rapidity of turnover time and fractures (Cowin, 2001). The following paragraphs will provide a brief description of the bone composition and structure at both microscopic and macroscopic level.

1.1.1. Bone composition

The bone is constituted for 65% by inorganic components (minerals) and for 35% by organic matrix, cells, and water. The mineral part is mainly impure hydroxyapatite, $\text{Ca}_{10}(\text{PO}_4)_6(\text{OH})_2$, containing constituents such as carbonate, citrate, magnesium, fluoride, and strontium. The bone mineral is in the form of small crystals in the shape of needles, plates, and rods located within and between collagen fibres. The organic matrix consists of 90% collagen and about 10% of various noncollagenous proteins. Bone cells are fundamental for the modelling and remodelling of the extracellular matrix as well as the calcium homeostasis. The cells in the bone belong to three families: osteoblasts, osteoclasts and osteocytes. Osteoblasts are bone-forming cells that synthesize and secrete unmineralized bone matrix, participate in the calcification and resorption of bone, and regulate the flux of calcium and phosphate across the bone. Osteoclasts are multinucleated giant cells and their function is to resorb both the mineral and organic component of the bone. Lastly, osteocytes are the most abundant cell type in mature bone and they are involved in the homeostatic, morphogenetic, and restructuring processes of bone mass. Basically, the osteocytes play a key role in the biological and mechanical regulation of bones (Cowin, 2001).

Both the mineral and organic parts of bone have important mechanical functions. The mineral part gives stiffness, which is fundamental for the support function of the bones as well as the transmission of muscular forces. On the other hand, the collagen provides tenacity to the bone, necessary to protect the soft tissues of the cranial, thoracic and pelvic cavities.

1.1.2. Bone microscopic and macroscopic structure

Bone tissue at the microscopic level is classified into two types: woven and lamellar (Cowin, 2001). The first one consists in a matrix of interwoven coarse collagen fibres and the osteocytes have a random distribution. Lamellar bone is made up of unit layers (lamellae), each lamella is approximately 3 to 7 μ m thick and contains fine fibres that run in approximately the same direction. The woven bone is less organized and shorter-lived than lamellar bone. In the developing embryo the bone is the woven type and then resorbed and replaced by lamellar bone.

The lamellae of the cortical bone appear in different patterns to form three structures: osteon, circumferential lamellae, and interstitial lamellae (Figure 1). In the osteon, or Haversian system, the lamellae are willing in circular rings surrounding a longitudinally vascular channel, the Haversian canal. Within this canal run blood, lymphatics vessels and nerves. Haversian canals are interconnected by transverse canals, also called the Volkmann canals. The circumferential lamellae consist on several layers of lamellae extending around the circumference of the bone shaft. The interstitial lamellae are angular fragments of bone composed of the remnants of past generations of osteons or circumferential lamellae and they fill the gaps between Haversian systems.

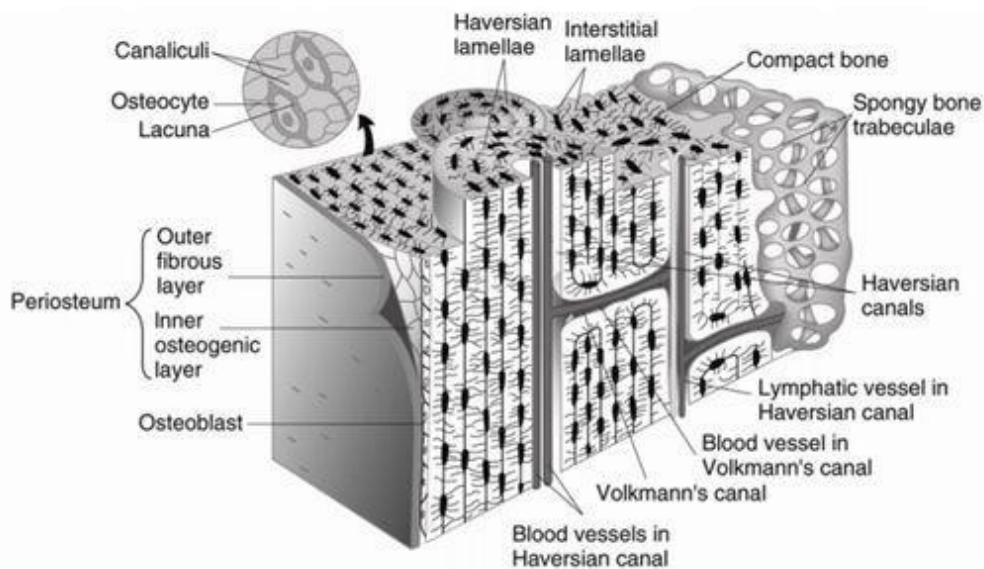


Figure 1: Diagram of cortical and trabecular bone of a sector of a long bone. (Tortora 1983)

Throughout woven and lamellar bone there are the lacunae, small cavities, in which osteocytes are entrapped. Radiating from the lacunae are tiny canals, or canaliculi, into which the long cytoplasmic processes of the osteocytes extend. These canals and the Haversian and Volkmann channels, form a 3D network that provides supply to the cells. The outer surface of most bone is covered by the periosteum which is a sheet of fibrous connective tissue and an inner cellular or cambium layer of undifferentiated cells. The periosteum has the potential to form bone during growth and fracture healing. The marrow cavity of bones is lined with a thin cellular layer called the endosteum which is a membrane of bone surface cells.

At the macroscopic level, the bone can be classified as cortical (or compact) or trabecular (or spongy). The distribution of cortical and trabecular bone varies significantly between different bones. Approximately 80% of the skeletal mass in the adult human skeleton is cortical bone and the remaining 20% is trabecular bone (Cowin, 2001). These types of bone tissue can be easily distinguished by their degree of porosity and density (Figure 2). The cortical bone is very dense and with a low porosity (5-10%), while the trabecular bone appears as a sponge with a porosity that varies between 45-95%.

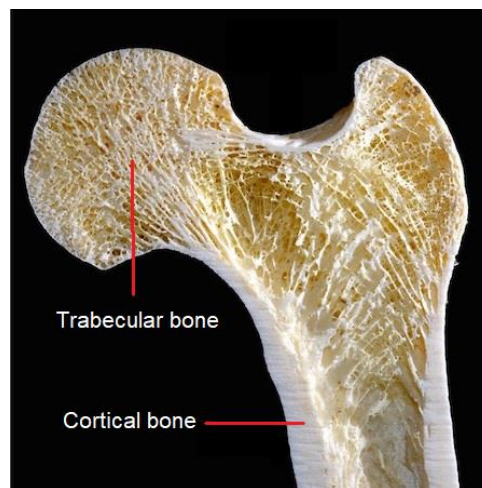


Figure 2: Cross-section of human femoral head showing trabecular and cortical bone. Source from http://medcell.med.yale.edu/systems_cell_biology/bone_lab.php

In the trabecular bone, the structural unit is the trabecular packet (Figure 3). In general, it lacks osteonal structure and consists of a mosaic of angular segments of parallel sheets of lamellae preferentially aligned with the orientation of the trabeculae.

The ideal trabecular packet is shaped like a shallow crescent with a radius of 600 μm and is about 50 μm thick and 1 mm long. The trabecular packets are hold together with cement lines, layer of mineralized matrix deficient in collagen fibres. Trabecular bone is not populated by the Haversian or Volkmann channels and the osteocytes are feed directly from the marrow.

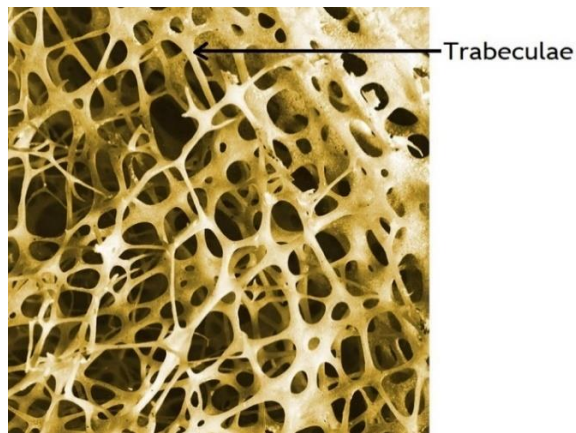


Figure 3: Scanning electron micrograph (SEM) of trabecular bone of the human shin. Source from <https://fineartamerica.com/featured/7-sem-of-human-shin-bone-science-source.html>.

Cortical bone cortical is a dense, solid mass with only microscopic channels and the main structural unit of cortical bone is the osteon or Haversian system (Figure 4). Osteons form approximately two thirds of the cortical bone volume; the remaining one third consist of interstitial and circumferential lamellae. A typical osteon is a cylinder about 200 or 250 μm in diameter and it is made up of 20 to 30 concentric lamellae. Each osteon is surrounding by a cement line, a 1- to 2- μm -thick. The Haversian canals are interconnected by the transverse Volkmann's canals within run blood vessels, lymphatics and nerves.

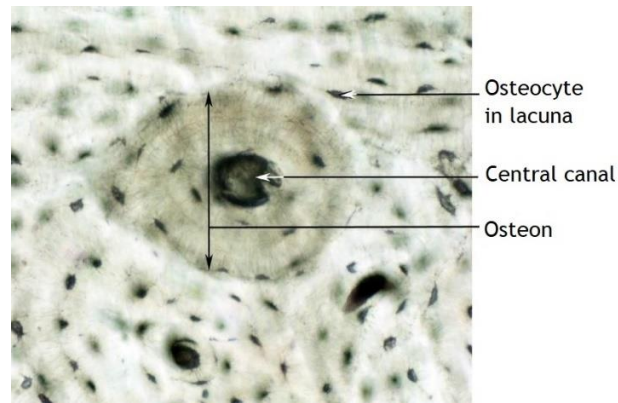


Figure 4: Cross-section of human compact bone shows the Haversian system (or osteon), the central canal and the lacunae. Source from <https://mesa-anatomy.weebly.com/supportive-connective-tissue.html>

Plexiform or laminar bone is a type of bone tissue in cortical bone of the long bones in large rapidly growing mammals such as cows and pigs and less frequently in the bones of primates, including humans (Figure 5). Plexiform bone consists of alternating layers of parallel-fibred bone and lamellae forming a brick-like structure. Each "brick" bone is about 125 μm across. This type bone also contains cores of non-lamellar bone and blood vessels surrounded by intercalating lamella bone. For instance, a bovine cortical bone may present microstructures with haversian bone, plexiform bone, or both together depending on the position considered. The two microstructures of haversian and plexiform bone have different mechanical properties (Kim et al., 2007). The fatigue strength of plexiform bone is higher than that of haversian bone.

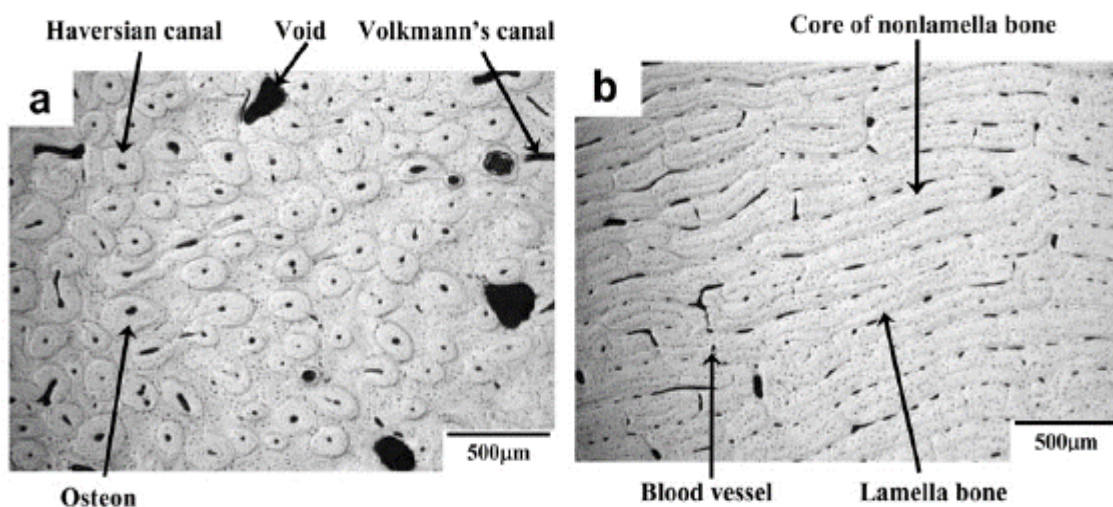


Figure 5: Optical micrographs of: (a) haversian and (b) plexiform bones of posterior and anterior of bovine femoral compact bones (Kim et al., 2007).

1.2. Morphological analysis

Micro-computed tomography (micro-CT) has become a standard tool for the evaluation of bone morphology and microstructure (Bouxsein et al., 2010). This type of imaging technique allows the three-dimensional (3D) nature of the bone structure to be visualised with high resolutions and in a non-destructive way. Different micro-CT systems with different hardware and scanning modalities are available and can achieve different spatial resolution (signal-to-noise ratio). The synchrotron radiation micro-CT (SR micro-CT) technique has also been used to investigate bone micro-architecture. The choice of spatial resolution is fundamental to observe in the image the features of a given structure. In standard laboratory micro-CT systems trabecular bone is generally imaged with voxel size between 5 μm and 20 μm , corresponding to fields of view of several centimeters but to visualize imaging lacunae and canaliculi in cortical bone, spatial resolutions at the micrometer or the nanometer scale is required, achievable with Synchrotron technology or nano-CT systems (Peyrin et al. 2014, Dong et al., 2014).

1.2.1. Micro Computed Tomography (Micro-CT)

Micro-CT systems use similar technology as clinical CT but allow to achieve better resolution. It is a powerful imaging technique for the characterization of different types of materials from the microstructural point of view. Similarly to clinical CT, micro-CT techniques is based on the interaction of the X-rays with the sample. A tomographic system, without considering the computer for the acquisition and reconstruction of images, is mainly composed by three elements: the X-ray source, the sample rotation system and the detector (Figure 6).

In most standard desktop micro-CT system, the sample is placed between the source and the detector on a rotary table. The angle of rotation of the sample and the rotation step between the individual projection images are parameters that can be chosen in most scanners. The detector has the function of measuring the intensity of the transmitted X-rays after they have interacted with the sample. Currently, there is a wide range of detector systems with properties that are very different from each other. At each rotation step the detector acquires a two-dimensional image, called projections, which are used to reconstruct a three-dimensional image of the same object.

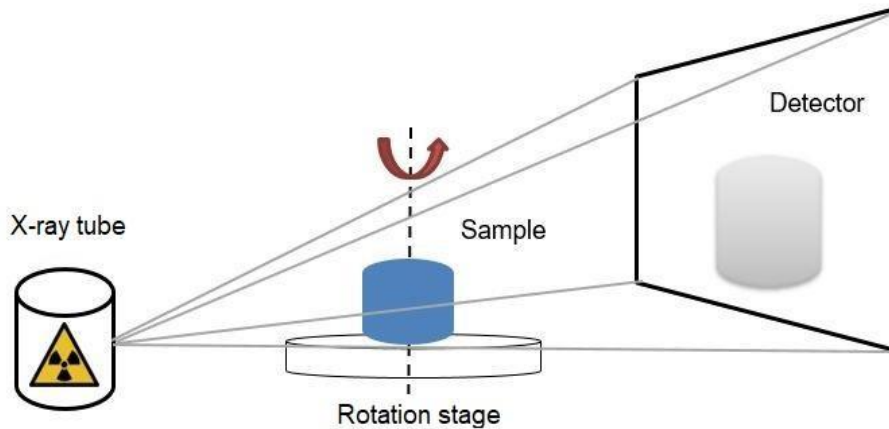


Figure 6: Configuration of a micro-CT scanner with a sample rotating within a stationary X-ray system

Typically, micro-CT systems operate in the range of 20 to 100 kVp, and the attenuation of the X-ray photons as they pass through material can be caused by either absorption or scattering depending on their energy (Bouxsein et al., 2010). The interaction of lower energy X-rays (less than 50 keV) is dominated by the photoelectric effect and depends on the atomic number of the materials. The photoelectric effect occurs when a photon interacts with an electron of the innermost orbits of the material's atom. In the collision, the photon is absorbed with the consequent emission of an electron (called photoelectron). At low energies, only small objects can be observed, otherwise noise becomes too large to allow quantitative analysis. The interaction of higher-energy X-rays (higher than 90 keV) is dominated by Compton scattering, where the attenuation is approximately proportional to the density of the material. The Compton effect consists in the inelastic collision of a photon with an electron belonging to an external orbital of the material's atom. In the interaction, the photon is diffused in a different direction and with a different wavelength, while the electron is put in motion with a certain kinetic energy. In the medium range of X-ray energy (from 50 to 90 keV), both the photoelectric effect and Compton scattering contribute to attenuation.

After acquiring the X-ray projection images, the computerised reconstruction of the 3D stack of images from the projection images is performed. The image reconstruction usually includes a beam hardening compensation. This artefact resulting from the fact that the X-ray tubes used in the μ CT systems do not produce X-rays of a single energy, but a spectrum of energies. A voxel is defined as the discrete unit of the

scan volume that is the result of the tomographic reconstruction. Typically, voxels from micro-CT images have all three dimensions equal and therefore are described as isotropic voxels. The resolution of the image is defined as the smallest feature that can be resolved in the image. Hence, the resolution and voxel size are not equivalent, and their relationship depends on several factors (i.e., mean absorption of sample, detector noise, reconstruction algorithm, X-ray focal spot size and shape, detector aperture, and scanner geometry) (Bouxsein et al., 2010). Small voxel size usually leads to high scan resolution; however, this requires longer acquisition times because more sample's projections need to be collected and processed. Therefore, a best compromise between the minimum resolution acceptable and the scan time should be found.

1.2.2. Synchrotron radiation micro-CT (SR micro-CT)

Synchrotron radiation or synchrotron light is an electromagnetic radiation generated by charged particles, usually electrons, moved at very high speeds in a large ring (in the order of kilometres). In the synchrotron facilities an electron gun produces electrons and a linear accelerator (LINAC) accelerates them into the booster ring (Figure 7). The electrons move at an increased rate until almost at the speed of light and system of deflecting magnets curves the path of electrons, forcing them to remain on a circular trajectory. When electrons change their direction, they emit a very high energy radiation. The flux and brilliance of the emitted radiations are increased, and the wavelength band reduce on the X-ray region. At last, the filtered X-rays are addressed in the experimental stations, located at the end of the beamline.



Figure 7: Diamond Light Source, UK. Source from: <http://www.diamond.ac.uk/Home/About.html>.

Using synchrotron sources provides several advantages to the micro-CT compared to the conventional X-rays tubes, especially to achieve images with spatial resolution below the micrometer (Figure 8). First, synchrotron sources offer a photon flux several orders of magnitude higher that both limit the scan times and increase the signal to noise ratio. Moreover, with a synchrotron source it is possible to obtain a monochromatic X-rays beam, that is important to limit the image artifacts such as beam-hardening, which is often a serious limitation for analysis conducted with laboratory X-rays systems that employ a polychromatic beam.

During the past decade, SR micro-CT has been used for the assessment of structure and mineralization in human or animal trabecular bone (Peyrin et al., 2014). Recently, its application on cortical bone allowed to explore the 3D osteocyte lacunar morphometric properties and distributions in human femoral bone with nominal voxel size of 1.4 μm (Dong et al., 2014). Consequently, SR micro-CT offers extremely high-resolution imaging of microarchitecture and mineral density in excised bone specimens. Nevertheless, the main disadvantages of this technique are its limited availability of the access to a synchrotron source as well as the costs (Bouxseis et al., 2010). Moreover, technical expertise needed to set properly the scan parameters to avoid damaging the sample due to the radiations.

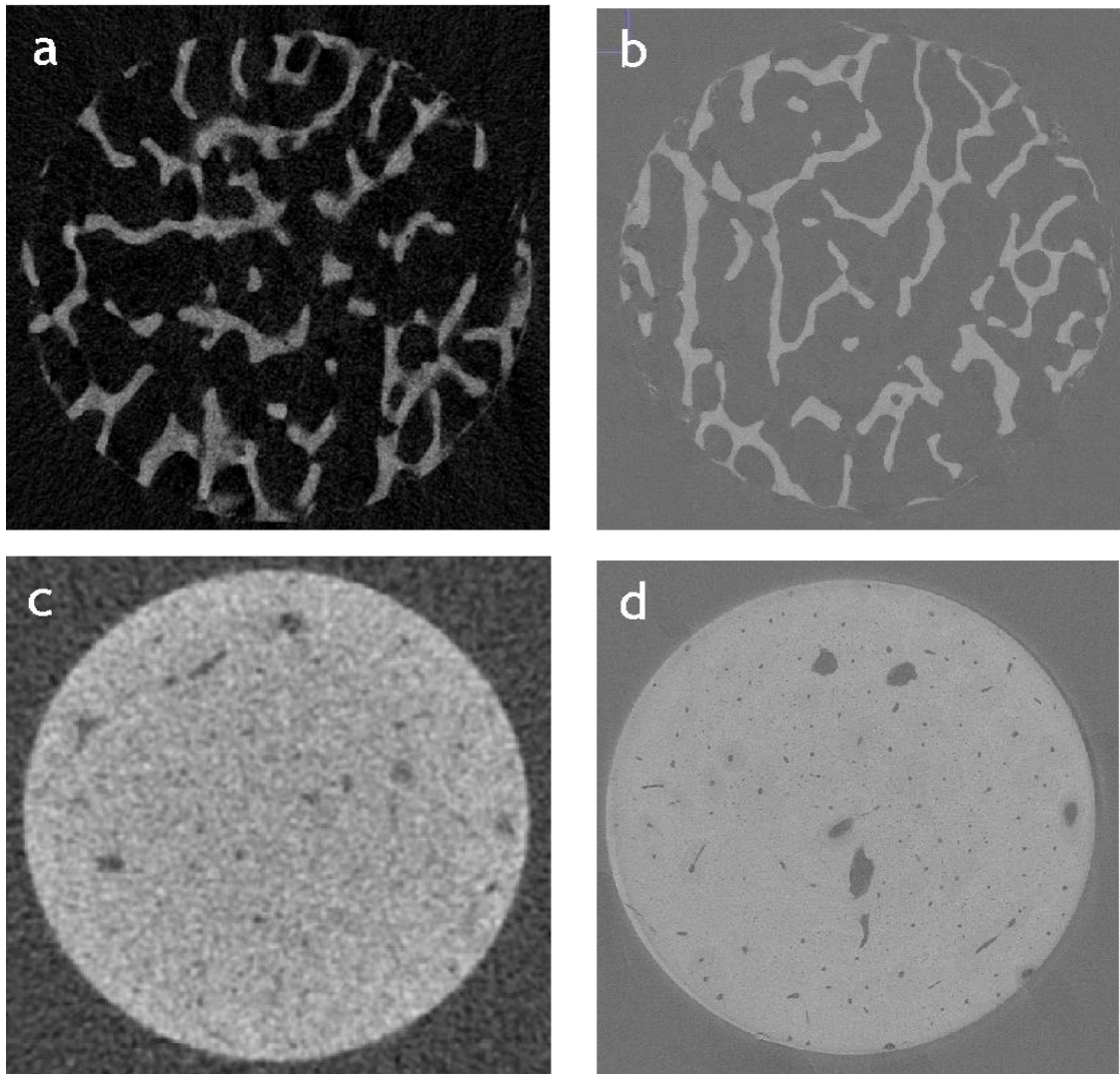


Figure 8: Trabecular (a) and cortical (c) bone scanned with laboratory micro-computed tomography (μ CT) at $10\ \mu\text{m}$ voxel size (Dall'Ara et al., 2014). Trabecular (b) and cortical (d) bone scanned with synchrotron light μ CT (SR μ CT) at $1.6\ \mu\text{m}$ voxel size (Palanca et al., 2017). The figures show the difference in terms of resolution between the μ CT and SR μ CT images. Indeed, in the cortical bone image scanned with SR μ CT (d) it is possible to identify a greater number of features (i.e. osteocyte lacunar and canaliculi) compared to the same tissue image scanned with μ CT.

1.3. Strain measurements in bone

To date, some methods have been used to measure the strains on bone at organ- and tissue-level (Grassi and Isaksson, 2015) (Table 1). Strain gauges (SGs) are the first to be used in bone biomechanics for strain measurements and they are still considered the gold standard for their accuracy and high frequency response (Cordey and Gautier, 1999; Cristofolini et al., 2009) (Figure 9). Nevertheless, SGs have a non-negligible

stiffness that can affect the strain measurement. Moreover, SGs application is limited mainly for the discreteness of measurements.

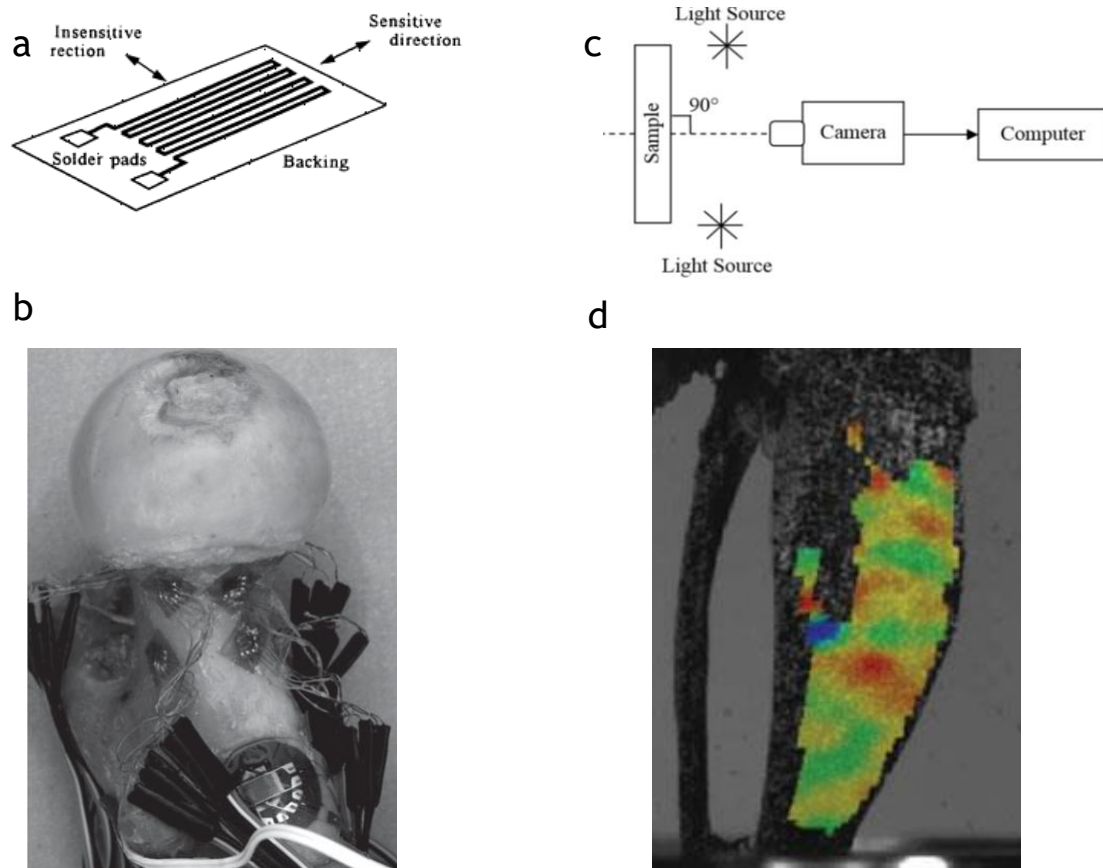


Figure 9: a: A schematic representation of a strain gauge. b: Strain gauges are bonded in the different regions of the proximal femur used for point-wise measurement of strain on the bone surface (Cristofolini et al., 2010). c: A schematic diagram of the experimental set-up for 2D-DIC system (Khoo et al., 2016). d: Mouse tibia surface strain measured with the digital image correlation technique (Pereira et al., 2015).

Fibre Bragg grating sensors (FBGS) can be a possible alternative to the strain gauges for measures at the interface between two materials (Fresvig et al., 2008). This is possible thanks to the absence of damageable electrical circuitry. However, FBGS application in bone biomechanics is still restricted for their lower accuracy and precision compared to strain gauges. Digital Image Correlation (DIC) is a non-contact method, which allows to measure strain over a large portion of the surface of the specimen (Palanca et al., 2016) (Figure 9). With this technique, one digital image is mapped onto another and the transformation field is determined by maximizing a correlation coefficient. Hence, the “reinforcement effect” does not occur when this

technique is used. In order to make the area of the specimen surface univocally identifiable, a speckle pattern is usually added. The spatial resolution of the DIC depends on the quality of the acquired images, on the applied speckle, and on the parameters of the correlation algorithm that should be optimized for every specific application.

However, all the methods mentioned above can measure strain only on the external surface of the bone specimens. The Digital Volume Correlation is the extension of the DIC to the third spatial dimension (Bay et al., 1999). DVC application on bone is recent and, to date known, it is the only method that can measure the internal strain field. Two volume images, one undeformed and one deformed, are used as the input of the DVC algorithm. The power of this technique is particularly due to the high resolution computed tomography (micro-CT or SR micro-CT) that allows slice images and 3D volumes of the internal microarchitecture to be generated, with resolutions of micrometre level. Therefore, the DVC is able to correlate the natural features in the 3D images, without the need of adding speckles. In the local DVC approach, the 3D volume is divided in to several sub-volumes which are registered and represented as a discrete function: $f(x, y, z)$ and $g(x + i, y + j, z + k)$ for the offset (i, j, k) in the x, y and z direction respectively (Figure 10). The displacement measurement step involves minimization of an objective function that quantifies the match between original and deformed subvolumes with respect to a set of affine transformation parameters (Bay, 2008). Finally, strains are estimated at all the measurement locations from the displacement vector field.

In order to recognize features in the two images and estimate the displacements and strain 3D fields, different DVC approaches with a number of computational strategies have been developed so far (Roberts et al., 2014; Palanca et al., 2015). The principal limit of the DVC is that the measurements are affected by the noise of the tomographic images (Dall'Ara et al. 2014). Since his introduction, a number of studies were performed to estimate the DVC accuracy and precision. Some examples are given in the next paragraph to show how the displacement and strain measurement errors are evaluated.

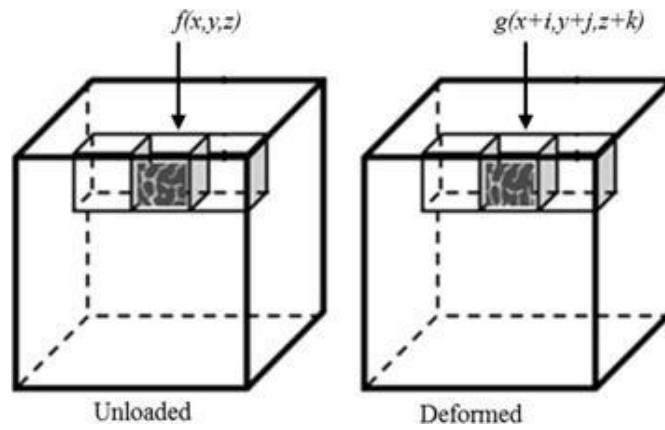


Figure 10: In the DVC algorithm, the image volumes are divided into sub-volumes represented with the functions $f(x, y, z)$ and $g(x+i, y+j, z+k)$ in the unloaded and deformed images respectively. An average displacement is computed for each subvolumes by finding the offset (i,j,k) that maximises a cross-correlation function (Gillard et al., 2014).

	<i>ADVANTAGES</i>	<i>LIMITATIONS</i>
Strain Gauges	<ul style="list-style-type: none"> - Gold standard for their accuracy and repeatability 	<ul style="list-style-type: none"> - Discreteness of the measurement - Reinforcing effect
Fibre Bragg Grating Sensors	<ul style="list-style-type: none"> - Absence of damageable electrical circuitry - Biocompatibility 	<ul style="list-style-type: none"> - Different sensitivity between positive and negative loads - High sensitivity to temperature gradients
Digital Image Correlation	<ul style="list-style-type: none"> - Full-field strain - Non-contact method 	<ul style="list-style-type: none"> - Only 2D or surface-3D
Digital Volume Correlation	<ul style="list-style-type: none"> - Full-field 3D strain distribution - Non-contact method 	<ul style="list-style-type: none"> - Quasi-static - Noise of the tomographic images

Table 1: Comparison of the principal methods used to measure strains in bone sample

1.4. DVC applications

The DVC was introduced for the first time to determine the 3D displacement and strain fields in trabecular bone (Bay et al., 1999). Since then, DVC has seen many applications as no other methods can give measurements of displacement and strain within samples. This technique is therefore ideal to investigate the internal strain distribution and the local damage inside bone, biomaterials or at the interface between them (Bay et al., 1999; Liu and Morgan, 2007; Hussein et al., 2012; Madi et al., 2013; Gillard et al., 2014; Danesi et al., 2016; Zhu et al., 2016). Consequently, the DVC can be very useful to address clinical and preclinical problems as well as validate Finite Element models (Zauel et al., 2006; Jackman et al., 2016; Chen et al., 2017; Costa et al., 2017).

To give some example, in a recent study, in order to understand the failure mechanism in prophylactically augmented vertebrae under compression, a DVC method was used for investigating the full-field strain distribution, from the elastic regime until failure (Danesi et al., 2016) (Figure 11).

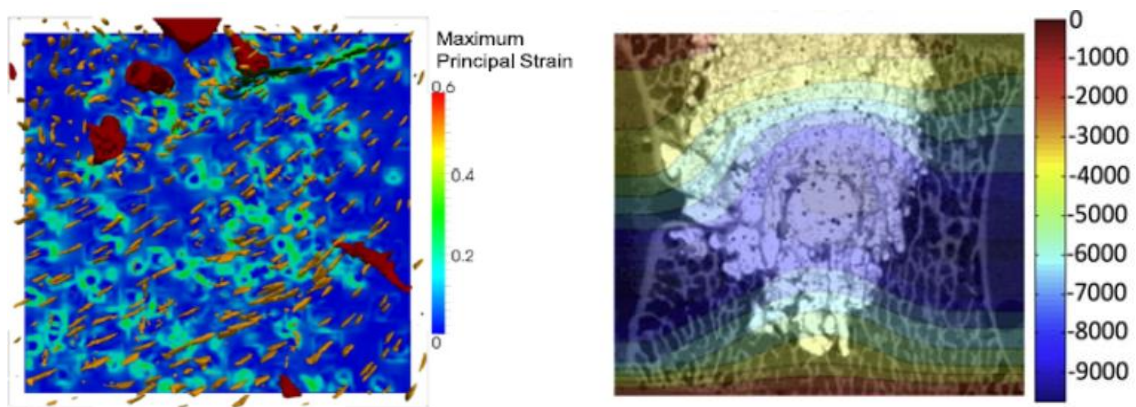


Figure 11: On the left-side: Strain map of murine cortical bone for the second load step after the initiation of the first microcracks. Transverse plane with the osteocyte lacunae (yellow), the microcrack (green) and the canals (red) (Christen et al., 2012). On the right-side: Internal strain distribution for 5% of compression in augmented vertebrae. The axial component of strain (in microstrain) is shown for the specimen over the sagittal slice (Danesi et al., 2016).

In a different study, the local strains distribution in murine femora have been measured during the initiation and propagation of microcracks using a SR-CT -based DVC (Christen et al., 2012) (Figure 11). This approach allowed to achieve spatial resolution of both displacement and strain approximately of 10 μm . Recently, a DVC

method has been used to validate a micro Finite Element models to predict the local displacement across the whole vertebral body under different degree of compression (Costa et al., 2017). The results of that study showed also a qualitative agreement between the strain distribution measured with DVC and predicted by the micro-FE models from all the specimens. However, a direct quantitative strain comparison could not be performed because, for a reasonable precision of the DVC, the nodal spacing should be 50 times higher than the element size of the micro-FE elements.

1.5. DVC accuracy and precision

Accuracy and precision of displacement and strain measurements obtained using DVC depend of several factors such as the quality of the volume images, the parameters in the correlation algorithm and the type of bone (Liu and Morgan, 2007; Roberts et al., 2014; Dall'Ara et al., 2017) (Table 2). To date, there is no gold standard for the assessment of accuracy and precision of the DVC due to the lack of other accurate technique able to measure internal displacements and strains (Palanca et al., 2015). The repeated-scans test in zero-strain condition is the most commonly adopted method for uncertainties measurement (Bay et al., 1999; Liu and Morgan, 2007; Dall'Ara et al., 2014; Palanca et al., 2015; Palanca et al., 2016). This type of test allows to evaluate the accuracy and precision including the effect due to the intrinsic noise of the micro-CT images (Dall'Ara et al., 2014). Another procedure to measure errors is the simulated-displacement test (or virtually-moved test) which is constructed from a single scan of a given specimen by translating the image volume by a uniform amount in each coordinate direction (Liu and Morgan, 2007; Dall'Ara et al., 2014; Palanca et al., 2015). This test is carried out usually to obtain a controlled displacement with a zero-strain field. However, in the simulated-displacement test the uncertainties are underestimated because the image noise is traced as a feature of the image. For this reason, in the repeated-scans test the error are generally larger than the ones compute for the simulated displacement (Dall'Ara et al., 2014).

Initially, the precision of the DVC in trabecular bone sample was measured by Bay with a repeated-scan test (Bay et al.,1999). Using an X-ray tomography with a resolution of 35 μm , in that study the strain measurement precision obtained was approximately of 300 μstrain . Afterwards, in another study the DVC has been applied at

different trabecular structures to measure displacements and strains (Liu and Morgan, 2007). Investigating several bone samples from different species and anatomical sites, that study showed how the accuracy and precision of DVC depend on the sample microstructure as well as on the computational approach. The maximum likelihood estimation (MLE) method used in that study achieve better results and, across all bone types tested, the displacement and strain precision errors ranged 1.86-3.39 μm and 345-794 $\mu\epsilon$, respectively. In particular, strain precision and accuracy were highest for specimens with lower volume fraction (BV/TV) and trabecular number (Tb.N), and higher trabecular spacing (Tb.Sp) and structural model index (SMI).

Reference	Imaging	Bone type	voxel size (μm)	Sub-volume (voxel)	Measured displacement * (μm)		Measured strain* (μstrain)	
					Accuracy	Precision	Accuracy	Precision
Bay et al., 1999	μCT	Trabecular	35	61	N.A.	1.23	N.A.	302-288
Liu and Morgan, 2007	μCT	Trabecular	36	40	-0.14	1.86-3.39	345-794	N.A.
Hussein et al., 2012	μCT	vertebral bodies	37	N.A.	21.46	41.44	740	630
Christen et al., 2012	SR- μCT	Cortical	0.74	25	0.0004	0.13	N.A.	11000-13000
Dall'Ara et al., 2014; Palanca et al., 2015	μCT	Trabecular	10	15**	N.A.	2270	~ 4000	~ 2400
		Cortical				2781	~ 5000	~ 2600
Palanca et al., 2016	μCT	vertebral bodies	39	16	N.A.	302	~ 300	~ 700
Palanca et al., 2017	SR- μCT	Trabecular	1.6	100**	N.A.	64	~ 240	~ 110
		Cortical				21	~ 55	~ 20

Table 2: Overview of the DVC accuracy and precision estimate with different parameters.

*Value referred as average of the errors across the different directions.

**Nodal Spacing used in the global approach.

For a more extensive assessment of the accuracy and precision of the DVC to measure the displacement and strain, both cortical and trabecular bone samples have been investigated (Dall'Ara et al. 2014). They found that the main source of error in the output of the DVC was due to the intrinsic noise of the micro-CT images. Moreover, that study showed that the uncertainties decreased as a power law by increasing the nodal spacing (i.e. distance between the nodes of the grid used for displacement and strain calculation), for all bone types. Therefore, a compromise between spatial resolution and measurements errors should be achieved when the DVC method is used. In that study, a nodal spacing of 600-700 μm for cortical and trabecular samples is suggested to discriminate yielded from non -yielded regions with accuracy and precision around 200 $\mu\epsilon$.

A comparative study between three different DVC computational approaches was conducted on cortical and trabecular bone samples (Palanca et al., 2015). Both repeated-scan and virtually-move test were used to quantify the accuracy and precision of the DVC approaches. Beside the different errors obtained from the three methods, it has been confirmed that the accuracy and precision tended to improve for larger sub-volume size (if the local method is used) or nodal spacing (if the global method is used) with an asymptotic trend over 30 voxels for the displacement and 50 voxels for the strains (with a voxel size of 9.96 μm). These parameter values could be used as a trade-off between spatial resolution and errors when the methods are applied to bone tissue.

In the studies mentioned above, it has been shown that with the micro-CT-based DVC uncertainties are too high for strain measurements performed at the bone structural unit level (Liu and Morgan, 2007; Dall'Ara et al., 2014; Roberts et al., 2014). Christen et al. used for the first time the synchrotron radiation-based computed tomography (SR micro-CT) to increase the spatial resolution of the DVC input images (Christen et al., 2012). In that study, a systematic error of the strain not significantly different from zero was achieved, while the precision was approximately 0.012 strains. However, to assess the accuracy and precision only a virtually-moved test was performed, which, as mentioned above, leads to underestimated errors (Dall'Ara et al., 2014). To overcome this problem, in a recent study Palanca et al. performed a zero-strain test on different bone types scanned with a SR micro-CT (Palanca et al., 2017). The uncertainties related to the strain measurements were lower than those obtained with traditional micro-CT images for all bone types with a spatial resolution of the measures around 40 μm to

keep uncertainties below 200 microstrain. The greatest improvement was found for cortical bone samples because at that resolution more features were identified in the bone microstructure, helping the correlation algorithm. In order to measure the DVC uncertainties under load, a virtually-compressed and a virtually-compressed-repeated test were performed on cortical bone sample (Palanca et al., 2017- Supplementary material). With the latter method, larger systematic and random errors were obtained due to the effect of the image noise. While this approach is an elegant way of testing the precision of the DVC measurements for under load, its application is limited to the mentioned study and more loading levels and mechanisms need to be explored to fully characterize the outcomes of DVC algorithms applied to SR micro-CT images (Dall'Ara et al., 2017).

1.6. Study aims

The Digital Volume Correlation provides internal displacement and strain fields of the bone. Many applications might take advantage from this method as the validation of the computational models. Using micro-CT images, acceptable precision on displacement measurements have been achieved with the DVC. However, for the strain field high uncertainties have been found and a compromise should be accepted between spatial resolution and precision of measurement. Recent studies have shown that the synchrotron radiation micro-CT can reduce the errors of the DVC, especially in the cortical bone. With this approach, adequately low uncertainties in the strain measures can be achieved with spatial resolution around 40 μm . Nevertheless, the accuracy of the DVC approach to measure internal strain of loaded bone structures is still unknown.

The main goal of this work is to develop a method for evaluating the accuracy and precision of SR micro-CT image-based DVC. In this study, different levels and directions of virtually affine deformations are imposed on repeated scans of cortical bone specimens to measure the uncertainties of the DVC.

2. Materials and methods

To evaluate the uncertainties of the DVC strain measurements, a new method has been designed in this study. Virtually-deformed tests have been carried out from repeated SR micro-CT scan of cortical bone specimens. Different direction and magnitude of simulated strain have been tested. Afterwards, the full-field strain distributions have been computed with a global DVC protocol.

2.1 Specimens and SR micro-CT

The specimens used in this project to measure the DVC uncertainties were prepared and imaged in a previous work as described in Palanca et al., 2017. Briefly, four 3 mm in diameter and 12 mm in length cortical bone cylinders have been extracted from the diaphysis of a fresh bovine femur (18 months old, killed for alimentary purposes). Tomography scans were performed at the Diamond-Manchester Imaging Beamline 113-2 of the Diamond Light Source, UK. The samples were aligned with the osteons parallel to the rotation axis during data collection. A filtered (950 μm C, 2 mm Al, 20 μm Ni) polychromatic ‘pink’ beam (5–35 keV) of parallel geometry was used with an undulator gap of 5 mm. The propagation distance was approximately 10 mm. Projections were acquired using a pco.edge 5.5 detector (PCO AG, Germany) coupled to a 750 μm -thick CdWO_4 scintillator, with visual optics providing 4x total magnification and a field of view of 4.2x3.5 mm. 4001 projection images were collected at equally-spaced angles over 180 degrees of continuous rotation, with an exposure time of 53 ms. With these parameters an effective voxels size of 1.6 μm was obtained. Each specimen was scanned twice under zero-strain conditions and without any repositioning between the two scans (Scan1 and Scan2).

Two cubic volumes of interest (VOIs), with side lengths of 1000 voxels, were cropped from the middle of each reconstructed image. Only one VOI for each couple of scans has been used in this study.

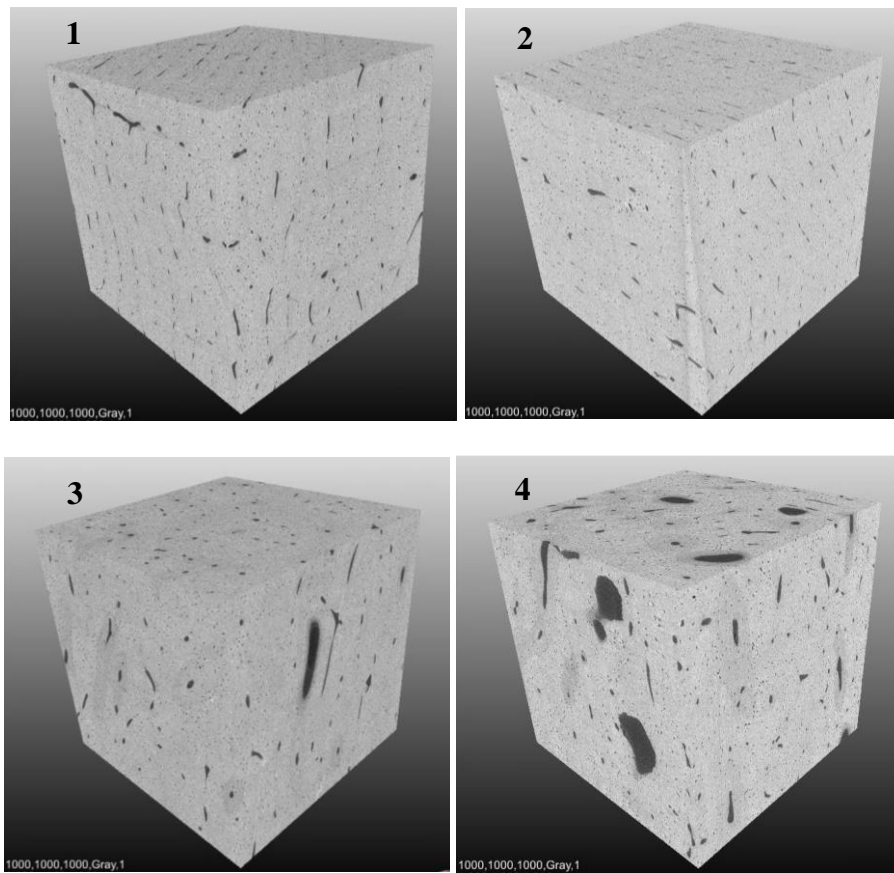


Figure 12: 3D representation of the VOIs of the four cortical bone specimens used in this study. Cortical bone scanned with SR-microCT at $1.6 \mu\text{m}$ voxel size. The side length of each cross section is 1000 voxels. The cube is therefore 1.6 mm in side.

The 3D reconstructions of the four cortical bone specimens are reported in Figure 12. It is possible to note the differences in terms of features' shape and orientation. The characteristics of the specimens depend on where they have been cored. In particular, they may exhibit a more regular and periodic structure, typical of the plexiform bone (see Specimen 1 and Specimen 2), a more Haversian structure (Specimen 4) or both (see Specimen 3).

2.2 Image processing

In order to evaluate the DVC measurement uncertainties under load, the following procedure has been applied to the cortical bone specimens. The virtually-

deformed-repeated analysis has been performed by registering the original scan (Scan1) with the Scan2 virtually deformed. As explained in the Introduction, this type of test allows to include the effect of the image noise in the DVC uncertainties analysis. Virtual deformations on the repeated scans (Scan 2) were applied using MeVisLab (MeVis Medical Solutions AG, Germany), which includes several modules for the processing and visualization of medical images. In this study, different conditions of load application (single compression and composed deformation), loading directions and load levels have been simulated.

2.2.1 Uniaxial deformations

First, the repeated scans (i.e. Scan 2 of each specimen) have been axially compressed applying 1%, 2% and 3% of deformation. These deformations have been performed separately along X, Y and Z axis, while the other directions were unstrained. Overall, nine deformation conditions have been carried out (Table 3).

Virtual compression

Direction	X	Y	Z
Levels	1%	1%	1%
	2%	2%	2%
	3%	3%	3%

Table 3: Uniaxial compression conditions for each specimen. Three levels of deformation (1%, 2% and 3%) along the three Cartesian directions (X, Y and Z) have been used.

First of all, the module *ImageLoad* allow to open the image file in different format (in this study DICOM) (Figure 13). Then, the compressions have been applied at the repeated scans using the module *AffineTransformation3D*. In MeVisLab the three-dimensional affine transformation is performed through a single matrix multiplication:

$$\begin{pmatrix} v'_x \\ v'_y \\ v'_z \\ 1 \end{pmatrix} = \begin{pmatrix} & t_x \\ M & t_y \\ & t_z \\ 0 & 0 & 0 & 1 \end{pmatrix} \begin{pmatrix} v_x \\ v_y \\ v_z \\ 1 \end{pmatrix}$$

The order for constructing the matrix is shearing, rotation, scaling and translation. To achieve sub-voxel resolution, trilinear interpolation is applied in the input volume using that module. The origin of the coordinate system is in the center of the output volume. Changing the coefficients of this matrix, it is possible to apply various levels of compression in different directions. The coefficients (c) have been computed as:

$$c = \frac{1}{1 - d}$$

Where d is the deformation imposed. Accordingly, along the directions in which a compression is not desired, the coefficients have value 1. Lastly, the deformed image can be store in a specific file format with the module *ImageSave* (in this study DICOM).

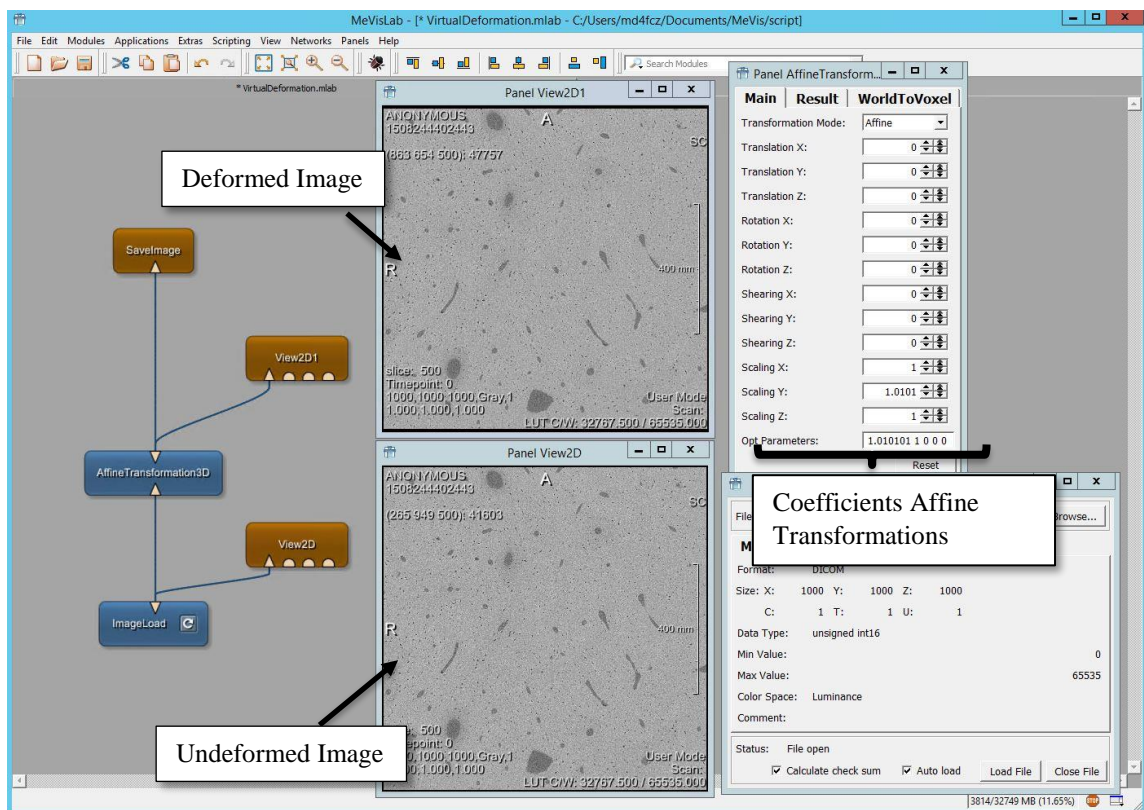


Figure 13: Screenshot of MeVisLab script used to apply the single compressions at the repeated scans. In this particular example compression of 1% along Y has been applied.

2.2.2 Composed deformations

A different analysis has been carried out to evaluate the possible effect of simultaneous deformations on the DVC uncertainties. Compressions in the three normal directions (X, Y and Z) within the MeVisLab framework have been performed on the repeated scan of one specimen (Specimen 3). In this case, one level of compression (1%) along three different direction has been simulated simultaneously. The coefficients have been computed as shown in the previous paragraph.

2.3 DVC protocol

In this study a global DVC protocol has been used to compute the strain field: ShIRT-FE (Dall’Ara et al., 2014). It is a combination of an elastic registration software known as Sheffield Image Registration Toolkit (ShIRT) (Barber and Hose, 2005; Barber et al., 2007) and a Finite Element (FE) software package (ANSYS Mechanical APDL v. 14.0, Ansys, Inc., USA). In this DVC approach a homogeneous cubic grid with a certain nodal spacing (NS) is superimposed to the two input images (Scan 1 and Scan 2). Therefore, ShIRT computes the displacements at each node of the grid by solving the registration equations as describe in Barber et al., 2007. Briefly, the procedure consists in finding the displacement functions $u(x, y, z)$, $v(x, y, z)$, and $w(x, y, z)$ that map the fixed image $f(x, y, z)$ into the moving image $m(x', y', z')$ and, to account changes in the gray levels, an additional intensity displacement function $c(x, y, z)$ is also included in the equation:

$$\mathbf{f}(x, y, z) - \mathbf{m}(x, y, z) \approx \frac{1}{2} \left(u \left(\frac{\partial \mathbf{f}}{\partial x} + \frac{\partial \mathbf{m}}{\partial x} \right) + v \left(\frac{\partial \mathbf{f}}{\partial y} + \frac{\partial \mathbf{m}}{\partial y} \right) + w \left(\frac{\partial \mathbf{f}}{\partial z} + \frac{\partial \mathbf{m}}{\partial z} \right) - c(\mathbf{f} + \mathbf{m}) \right) \quad (1)$$

This equation can be defined for each image voxel. However, there are four unknowns for each equation (u , v , w , c) and the resulting system becomes undetermined. The rank of the problem is reduced by expanding the functions u , v and w in terms of a set of local basis functions. In particular, ShIRT uses tri-linear basis functions centered on the nodes of a superimposed regular cubic grid to interpolate the displacements.

$$u(x, y, z) = \sum_i a_{xi} \varphi_i(x, y, z) \quad (2)$$

$$v(x, y, z) = \sum_i a_{yi} \varphi_i(x, y, z) \quad (3)$$

$$w(x, y, z) = \sum_i a_{zi} \varphi_i(x, y, z) \quad (4)$$

In the equations the term $\varphi_i(x, y, z)$ is the i th basis function centered at the node with coordinate x_i, y_i, z_i . The coefficients a_{ji} of the displacement function are the new unknowns. The Equation (1) can be now written in matrix notation (capital letters represent tensors, low case letters represent vectors) as

$$\mathbf{f} - \mathbf{m} = \mathbf{T}\mathbf{a} \quad (5)$$

where the matrix \mathbf{T} is derived from integrals of the image gradients multiplied by the basis functions.

The resolution of the mapping is defined as the spacing between the nodes. If that value is small, then the equation (5) become ill-posed. Therefore, a further constraint is applied by ShIRT to smoothness on the mappings. The result of adding this constraint is to convert the equation (5) to the form:

$$\mathbf{T}^T(\mathbf{f} - \mathbf{m}) = (\mathbf{T}^T\mathbf{T} + \lambda\mathbf{L}^T\mathbf{L})\mathbf{a} \quad (6)$$

where \mathbf{L} is the Laplacian operator, and λ is a parameter that weights the smoothing. Given a starting value of \mathbf{a} , a correct solution can be computed iteratively. If \mathbf{a}_n is the value of the displacements after n iterations, the updated value is:

$$\mathbf{a}_{n+1} = \mathbf{a}_n + \Delta\mathbf{a} \quad (7)$$

where

$$\Delta\mathbf{a} = [\mathbf{T}^T\mathbf{T} + \lambda\mathbf{L}^T\mathbf{L}]^{-1}(\mathbf{T}^T(\mathbf{f} - \mathbf{m}(\mathbf{a}_n)) - \lambda\mathbf{L}^T\mathbf{L}\mathbf{a}_n) \quad (8)$$

To avoid an accumulation of the interpolation errors, at each stage $\mathbf{m}(\mathbf{a}_n)$ is calculated by applying the current \mathbf{a} to the original image \mathbf{m} . Iteration stops when the average absolute value of the difference between \mathbf{a}_{n+1} and \mathbf{a}_n is below 0.1 voxels. After that,

the six components of strain at each node of the grid are computed by differentiating the displacement field with ANSYS. The strain vector for a three-dimensional domain is given by

$$\{\boldsymbol{\varepsilon}\} = [\varepsilon_x \quad \varepsilon_y \quad \varepsilon_z \quad \gamma_{xy} \quad \gamma_{yz} \quad \gamma_{zx}]^T$$

where ε_x , ε_y and ε_z are the normal strain component and γ_{xy} , γ_{yz} and γ_{zx} are the shear strain components, expressed as partial derivatives of the displacements u , v and w .

$$\begin{aligned} \varepsilon_x &= \frac{\partial u}{\partial x} & \varepsilon_y &= \frac{\partial v}{\partial y} & \varepsilon_z &= \frac{\partial w}{\partial z} \\ \gamma_{xy} &= \frac{\partial u}{\partial y} + \frac{\partial v}{\partial x} & \gamma_{yz} &= \frac{\partial v}{\partial z} + \frac{\partial w}{\partial y} & \gamma_{zx} &= \frac{\partial w}{\partial x} + \frac{\partial u}{\partial z} \end{aligned}$$

In this study, the University of Sheffield high performance computing server has been used to perform the DVC analysis (Figure 14). An input file has been prepared with the image parameters and the adjustable registration parameters (image voxel size, NS and number of iterations) and the path of the three input images: the original scan (Scan 1), the deformed scan (Scan 2) and the mask (not used in this study because the bone tissue was distributed over the whole image). With a semiautomatic procedure, ShIRT has been launched to estimate the displacements field and then ANSYS has been run to compute the strains. In this work, a nodal space of 25 voxels (40 μm) has been used for all the DVC analysis. As shown in a previous zero-strain study (Palanca et al., 2017) this value of NS can be taken as a best compromise between spatial resolution and errors. The number of iterations selected for all the registrations was 100.

Moreover, for the registration at the 1% of uniaxial deformations along x y and z, different values of NS (from 15 to 125 voxels) have been used in order to evaluate the effect of the NS on the DVC uncertainties using virtually loaded images. Also, the zero strain condition tests (Scan1 – Scan 2 not deformed) have been carried out to compare the result obtained in this study with the previous ones reported by Palanca et al., 2017 to make sure the new semi-automatic algorithm provides the expected values and for training purpose.

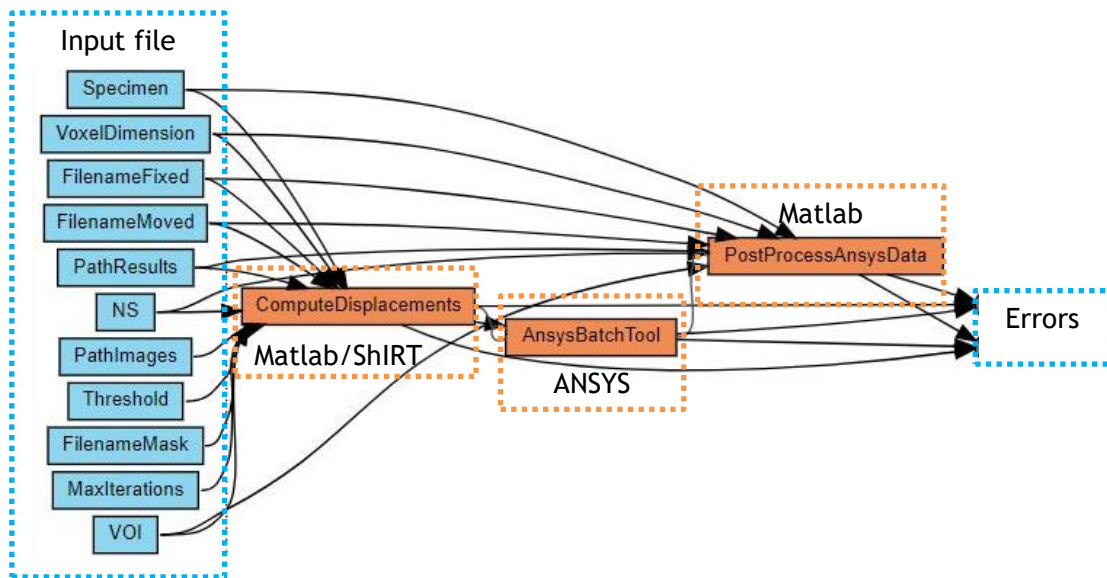


Figure 14: Schematic representations of the DVC analysis performed in this study. After setting the parameters and the input images, ShIRT is launched to estimate the displacements. Then ANSYS compute the six components of strain and the post processing for the uncertainties analysis is performed with Matlab.

2.4 Uncertainties analysis

The accuracy and the precision of the DVC to measure stains were evaluated with a home-written script MatLab R2017b (The MathWorks, Inc.). As mentioned above, the strains are computed at each node of a grid placed across the image (Figure 15). When this grid is created, automatically the first node is placed in the center of the image and then nodes are added at distance proportional to the NS on each direction until one layer of nodes lay outside the image. The origin of the coordinate system is at the top left corner of the image.

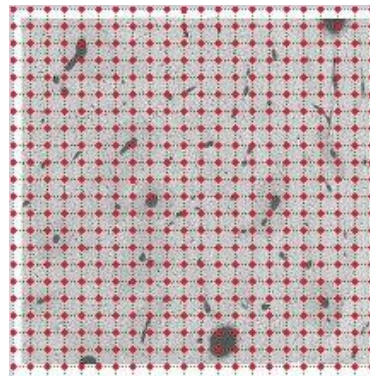


Figure 15: Schematic representation of the homogeneous cubic grid with a certain nodal spacing (NS) superimposed to one input image (2D representation).

When the image is virtually compressed, in order to replace the moved bone tissue, black voxels have been added in the planes perpendicular to the deformation direction (Figure 17). For this reason, before quantifying the errors, a procedure of removing layers was adopted in a Matlab script, excluding the nodes in the border which correspond to those positions in the deformed image. In fact, these measures are more influenced by the error, due to the lack of features in the border along the compression direction. In particular, the layers of nodes were removed according to the defined NS in the registration and the level and the direction of the applied compression. The script reads the result file of the strain field compute by Ansys. The result file is composed by different columns; the first one specifies the number of the node of the grid, then the other columns indicate the correspondent six independent component of the strain tensor.

The information of the spatial position of the corresponding nodes of the grid can be read in a different file in which the number of the node is associated with his coordinates, as shown in Figure 16.

Node	x [um]	y [um]	z [um]	u [um]	v [um]	w [um]
1	0.800	0.800	0.800	-0.44381014	0.11462426	-0.88345812
2	0.800	40.800	0.800	-0.32364049	0.27503644	-0.88184026
3	0.800	80.800	0.800	-0.27812164	0.24278959	-0.91490592
4	0.800	120.800	0.800	-0.32778897	0.30132845	-0.86921793
5	0.800	160.800	0.800	-0.30195665	0.22318584	-0.83673770
6	0.800	200.800	0.800	-0.33850684	0.24078331	-0.83913687
7	0.800	240.800	0.800	-0.31517119	0.17179590	-0.83664524
8	0.800	280.800	0.800	-0.20539619	0.21502002	-0.86158050
9	0.800	320.800	0.800	-0.18382664	0.26516525	-0.77830551

Figure 16: Example of the first lines of the output files that contain the numbers of the node (Node) and the coordinates of the nodes (x, y and z). In the same file is also possible read the displacements of each node (u, v and w).

The Nodal Spacing, the voxel size, the number of voxel that composed the VOI and the nominal strain applied must be specified in the script. This allows to exclude the values that correspond to strain measurements in the nodes outside of the bone tissue in the virtually deformed image due to the compression (Figure 17). In case of composed deformation, as the compression has been performed in all the three directions, that procedure has been performed in all the boundaries (Figure 17).

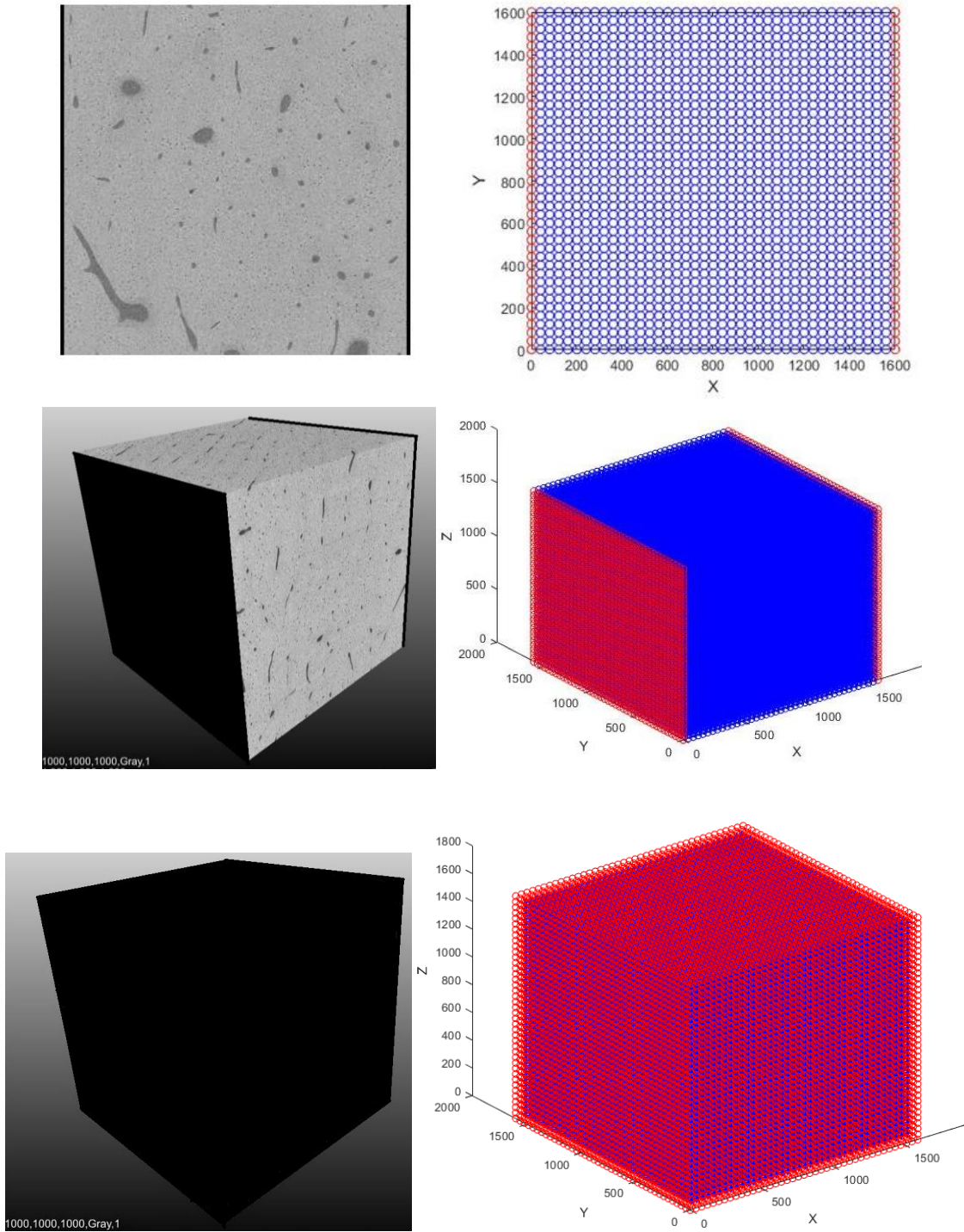


Figure 17: On the left side is shown the VOI after 1% of compression along X (represented in 2D and 3D) and after 1% of compression along X, Y and Z. On the right side, the representation of the spatial distribution of the strain measurements (represented in 2D and 3D). The nodes of the border removed along the direction of compression have been highlighted in red.

Afterwards, the uncertainties analysis of the DVC for strain measurements is performed computing different metrics. First, for each specimen, the systematic and random error were quantified for each component of strain as in (Gillard et al., 2014; Palanca et al., 2015; Palanca et al., 2016; Tozzi et al., 2017; Palanca et al., 2017). This type of analysis is conducted to find out any potential anisotropy in the DVC strain measurements when a deformation is applied. The systematic error for each component of strain has been computed as average of the respective component of strain on the evaluated nodes, subtracting the nominal value. In a similar way, the random error for each component of strain has been calculated as standard deviation of the respective component of strain on the evaluated nodes, subtracting the nominal value. The systematic or random percentage errors have been computed as the percentage ratio between the systematic or random errors computed over the nodes of the DVC grid and the nominal applied deformation.

In order to allow the comparison between this work and other study in the literature, two different metrics were used to account simultaneously for the errors along the six independent components of strain: the mean absolute error (MAER) and the standard deviation of the error (SDER). The first one, referred as “accuracy” in (Liu and Morgan, 2007), is compute as average of the average of the absolute value of the six components of strain in each node.

$$MAER = \frac{1}{N} \sum_{k=1}^N \left(\frac{1}{6} \sum_{c=1}^6 |\varepsilon_{c,k}| \right)$$

Where ε_c represents the six independent components of strain and N is the number of measurement points. The SDER, referred as “precision” in (Liu and Morgan, 2007), is calculated as standard deviation of the average of the absolute values of the six components of strain in each node.

$$SDER = \sqrt{\frac{1}{N} \sum_{k=1}^N \left(\frac{1}{6} \sum_{c=1}^6 |\varepsilon_{c,k}| - MAER \right)^2}$$

In this study, the results are reported as median and standard deviation of the errors computed among the values found for the four specimens for each component of strain. The frequency plots have been represented for each component of strain and each specimen in order to evaluate the peaks and the tails in the strain distribution and give a first estimation of either systematic and random errors. Moreover, to assess the effect of the NS on the DVC uncertainties, the trend of the systematic and random errors in function of different NS have been shown in the results.

The spatial distribution of the six strain components in different section planes of each VOIs has been analyzed with Ansys Workbench post-processing functions. This allowed to locate any error concentration inside the specimens.

Lastly, as a further evaluation of the uncertainties, more layers of nodes have been removed from the strain measurements along the deformation direction (Figure 18). Trends of the systematic and random error of the strain components have been reported in function of the number of levels of nodes removed from the border.

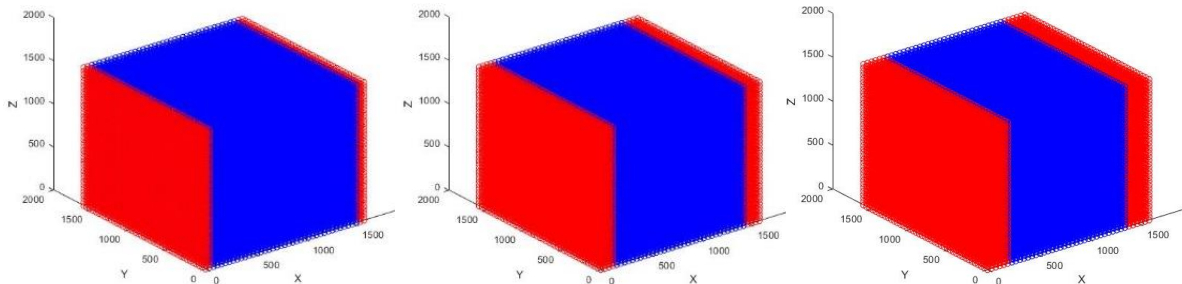


Figure 18: Layers of nodes in the border removed from the uncertainties analysis have been highlighted in red. Here the deformation was along Y. Instead, the blue

3. Results

3.1 Frequency plot

The normal and shear strain components distributions (EPELX, EPELY, EPELZ, EPELXY, EPELYZ and EPELXZ) for different directions (X, Y and Z) and level (1%, 2% and 3%) of virtual deformation have been visualised out for all the specimens. The frequency plot of the nominal strain components, along the direction of deformation showed a more pronounced peak in the nominal strain and, for the other deformation directions, the peaks were located around 0 microstrain (Figure 19, Figure 20 and Figure 21). Moreover, the shape of the distribution was more symmetric in the components where no deformation is applied. Shorter peaks at higher strain value were observed in the strain distributions for the components along the deformation direction.

Along one deformation direction, the frequency plot of the normal strain components highlights the shift of the central peak towards the increasing the level of deformation (1%, 2% and 3%) (Figure 22, Figure 23, Figure 24). Similar trends have been obtained in the frequency plot of the strain components in all the specimens used. For this reason, only one case has been reported here (Specimen 2).

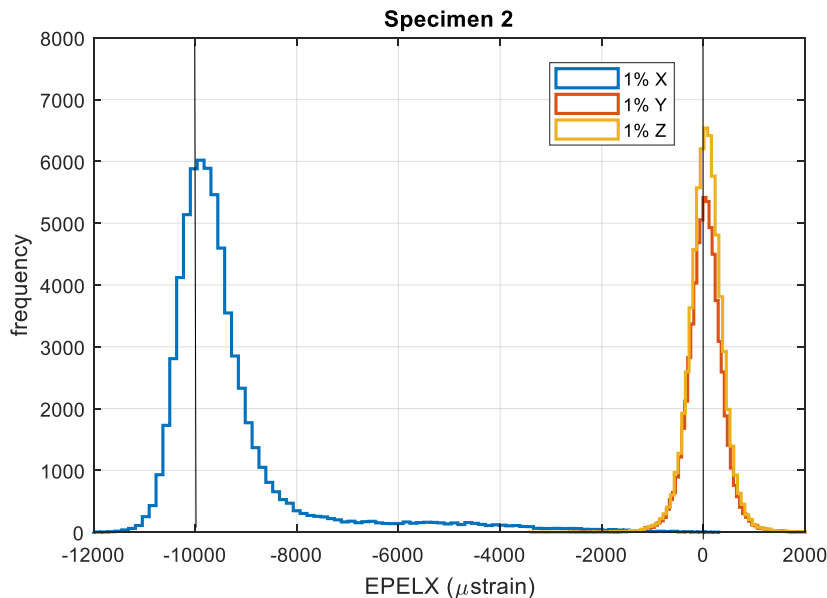


Figure 19: Frequency plot of the normal strain component along X in the Specimen 2 for 1% of deformation along X, Y and Z. The results for the other specimens showed similar trends. The black vertical lines highlight the nominal virtual deformation applied on the strain component considered.

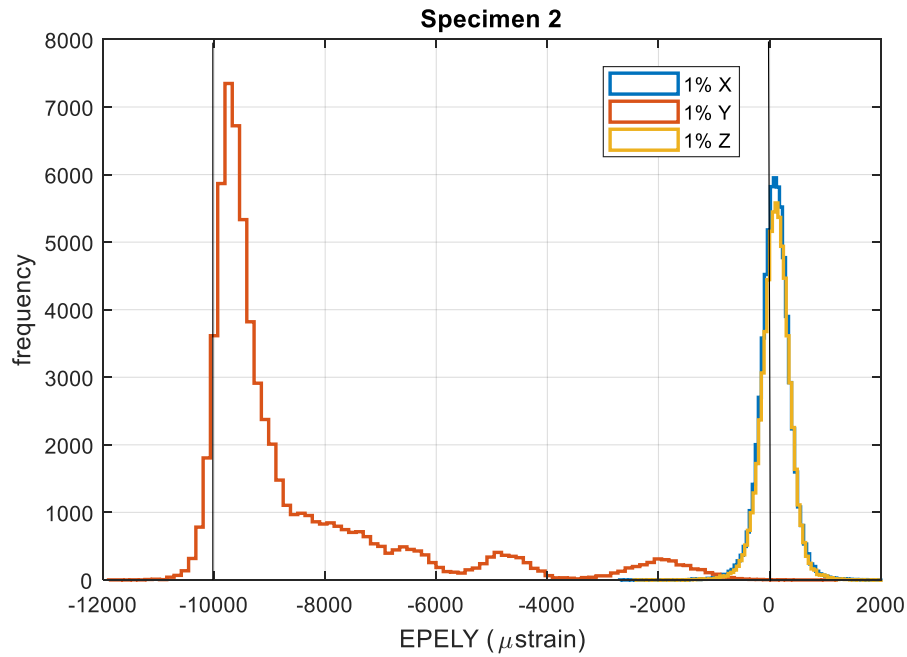


Figure 20: Frequency plot of the normal strain component along Y in the Specimen 2 for 1% of deformation along X , Y and Z . The results for the other specimens showed similar trends. The black vertical lines highlight the nominal virtual deformation applied on the strain component considered.

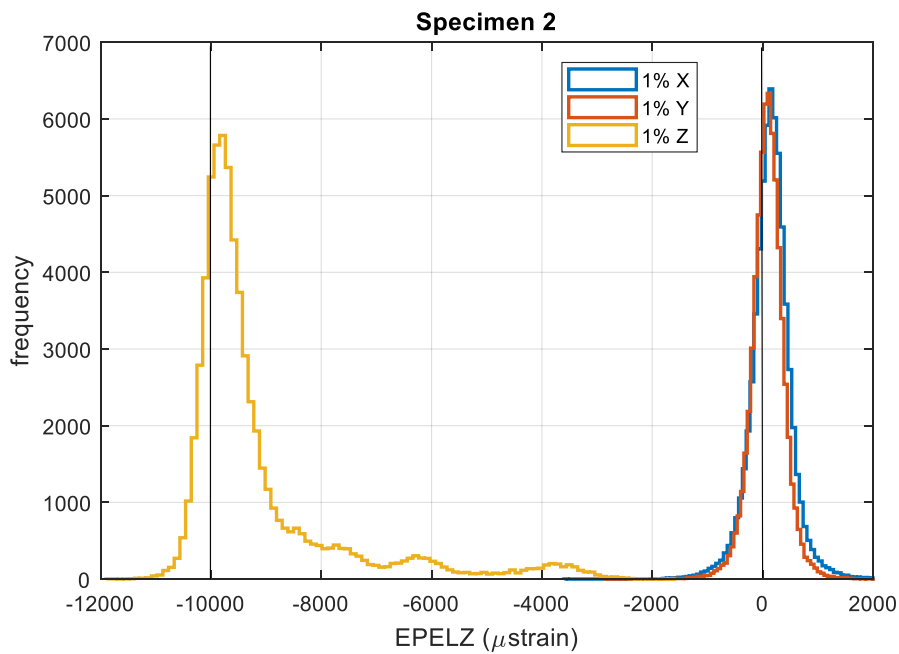


Figure 21: Frequency plot of the normal strain component along Z in the Specimen 2 for 1% of deformation along X , Y and Z . The results for the other specimens showed similar trends. The black vertical lines highlight the nominal virtual deformation applied on the strain component considered.

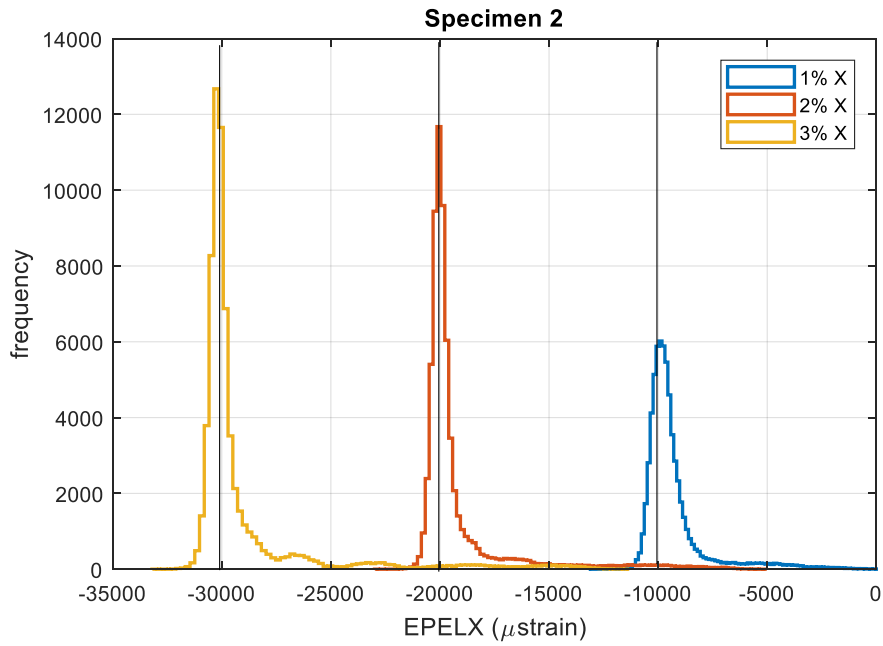


Figure 22: Frequency plot of the normal strain component along X in the Specimen 2 for 1%, 2% and 3% of deformation along X. The results for the other specimens showed similar trends. The black vertical lines highlight the nominal virtual deformation applied on the strain component considered.

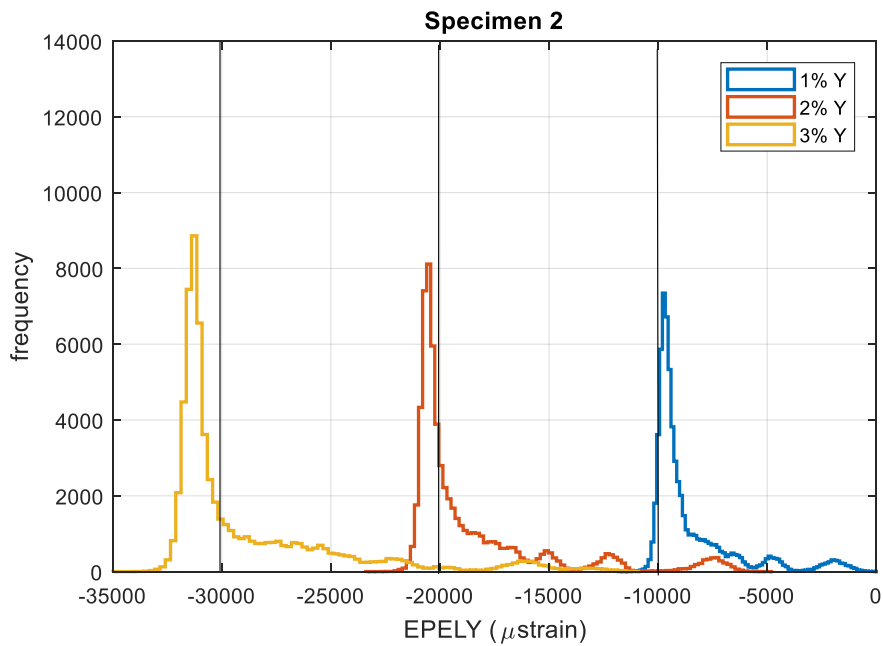


Figure 23: Frequency plot of the normal strain component along Y in the Specimen 2 for 1%, 2% and 3% of deformation along Y. The results for the other specimens showed similar trends. The black vertical lines highlight the nominal virtual deformation applied on the strain component considered.

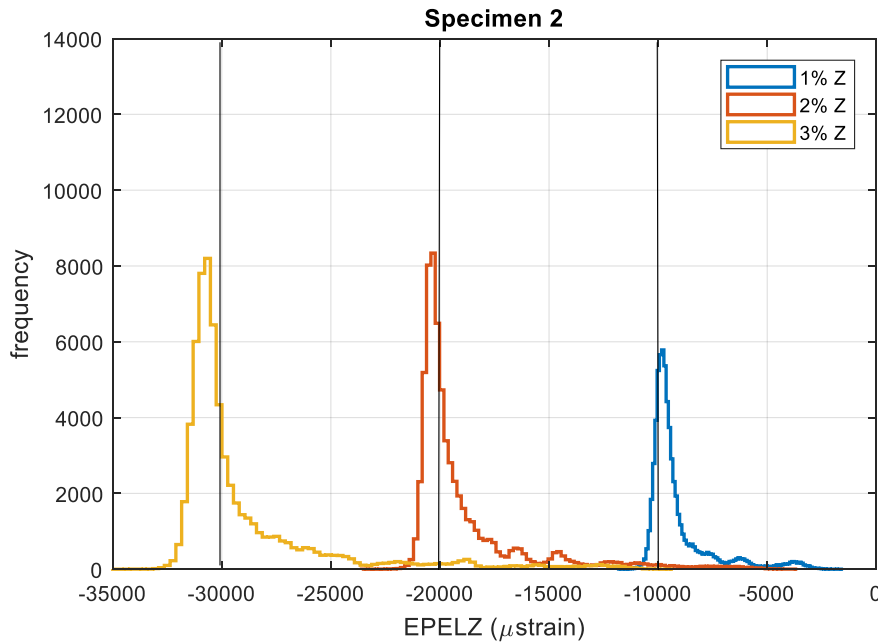


Figure 24: Frequency plot of the normal strain component along Z in the Specimen 2 for 1%, 2% and 3% of deformation along Z. The results for the other specimens showed similar trends. The black vertical lines highlight the nominal virtual deformation applied on the strain component considered.

The distributions of the shear strain components (EPELXY, EPELYZ and EPELXZ), for different direction and magnitude of simulated stain, showed a similar pattern (Figure 25, Figure 26 and Figure 27). In fact, in all the shear strain components the frequency plot presented a gaussian distribution shape with a peak collocated approximately in 0 microstrain. The frequency plots were similar almost in all the specimens except for one (Specimen 1) who showed a different pattern only in the XY shear strain component for deformation along X and Y (Figure 28).

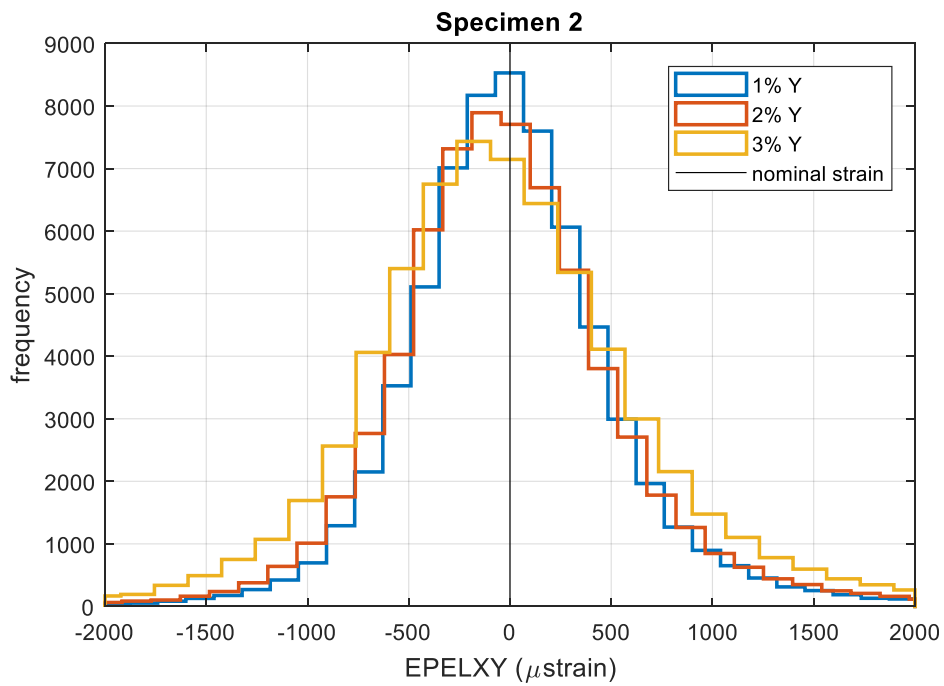
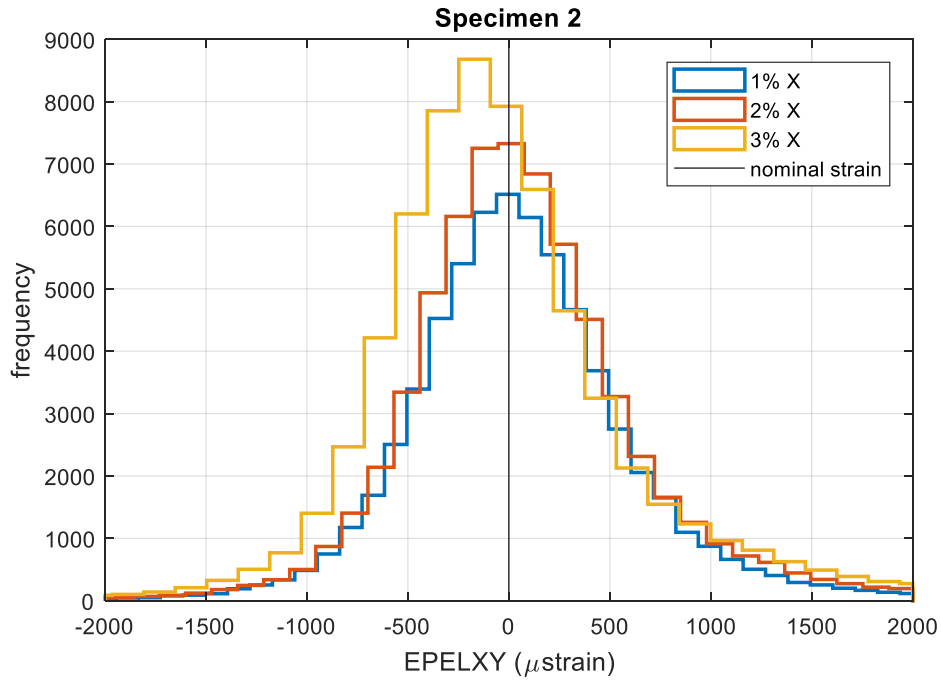


Figure 25: Frequency plot of the shear strain component along XY in the Specimen 2 for 1%, 2% and 3% of deformation along X (on the top) and along Y (on the bottom). The black vertical line highlights the nominal virtual deformation applied on the strain component considered.

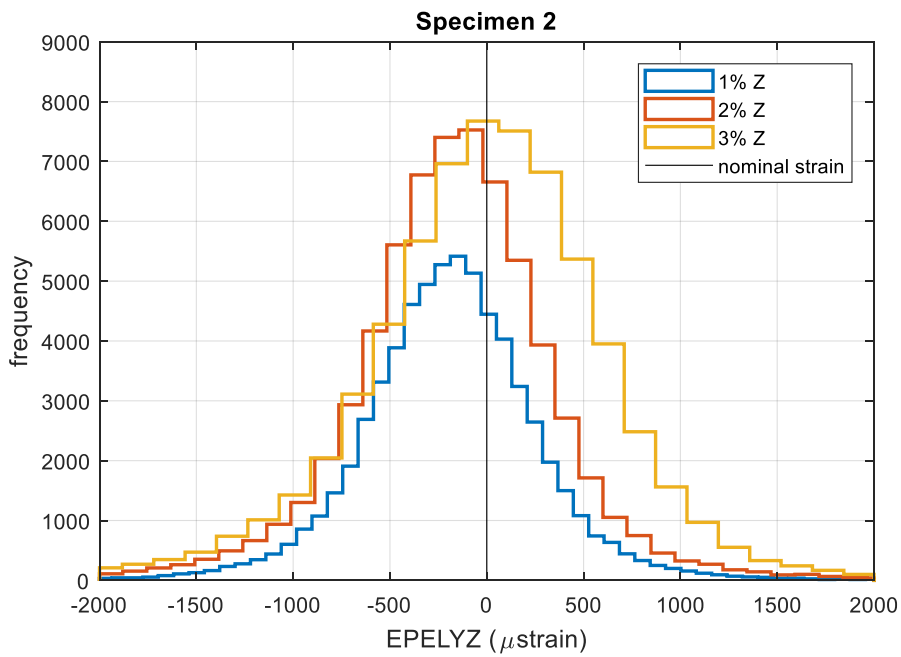
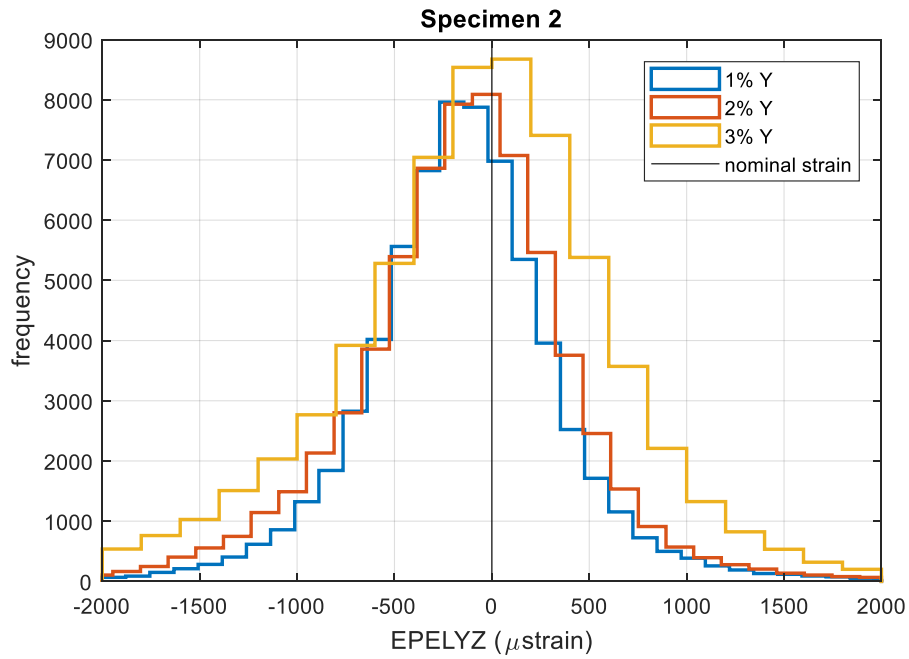


Figure 26: Frequency plot of the shear strain component along YZ in the Specimen 2 for 1%, 2% and 3% of deformation along Y (on the top) and along Z (on the bottom). The black vertical line highlights the nominal virtual deformation applied on the strain component considered.

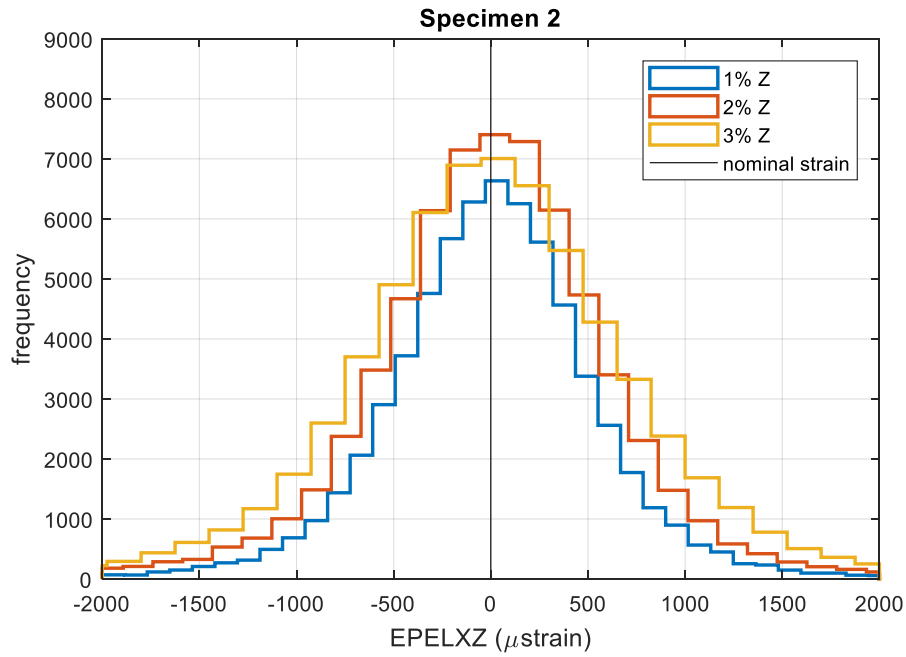
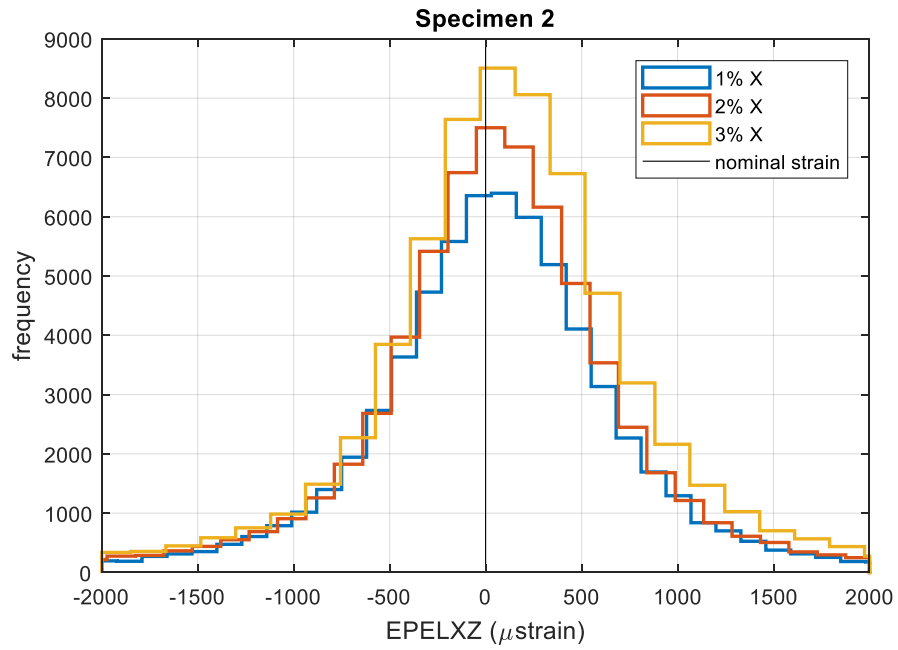


Figure 27: Frequency plot of the shear strain component along XZ in the Specimen 2 for 1%, 2% and 3% of deformation along X (on the top) and along Z (on the bottom). The black vertical line highlights the nominal virtual deformation applied on the strain component considered.

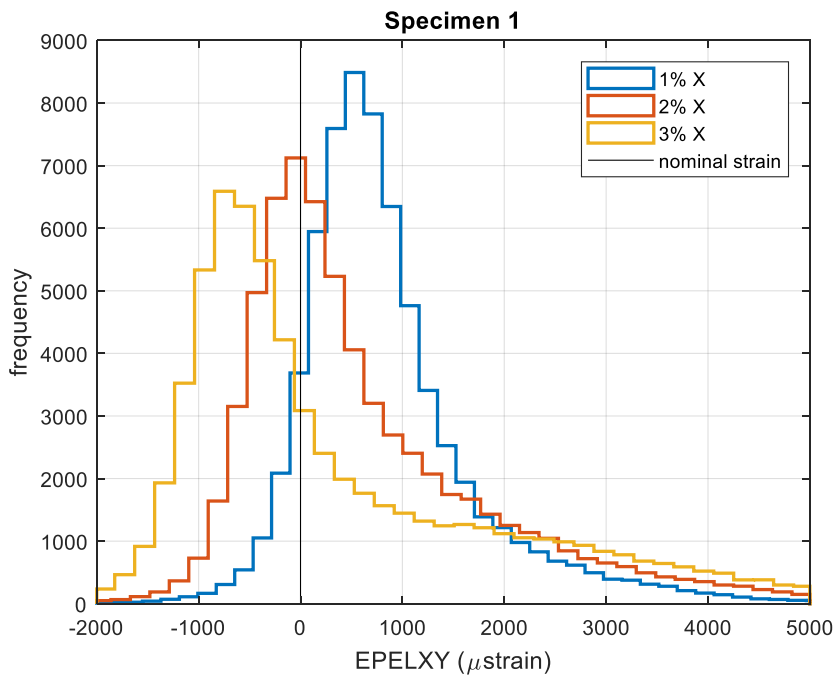
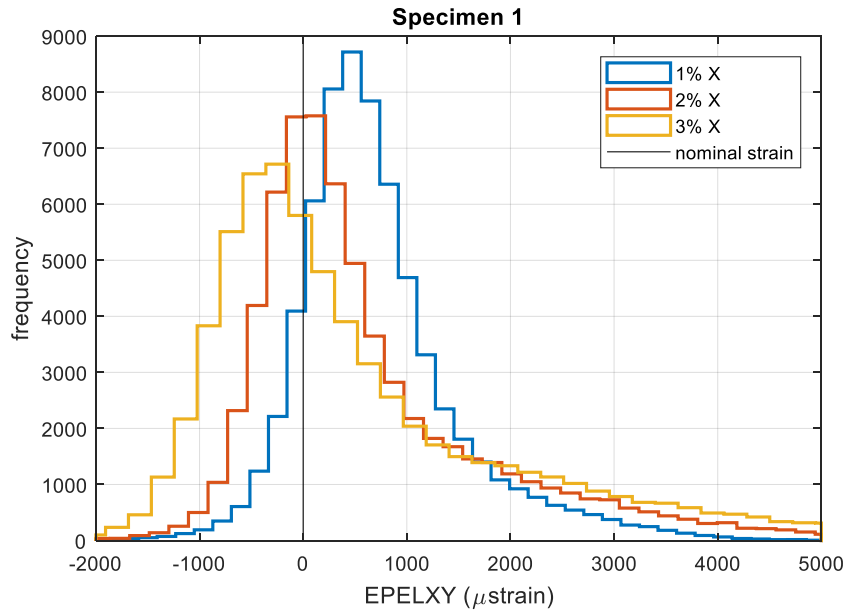


Figure 28: Frequency plot of the shear strain component along XY in the Specimen 1 for 1%, 2% and 3% of deformation along X (on the top) and along Y (on the bottom). The black vertical line highlights the nominal virtual deformation applied on the strain component considered.

3.2 Systematic errors

Median and standard deviation of the systematic error of each component of strain have been evaluated for the four specimens, at every deformation level and direction simulated (Figure 29, Figure 30 and Figure 31). The systematic errors of the normal strain components along the deformation direction were higher compared to the those computed for other strain components, at each deformation level and direction.

The systematic errors of the normal strain component along X were 714 ± 210 , 864 ± 193 and 985 ± 131 microstrain for 1%, 2% and 3% of nominal deformation along X, respectively. Systematic errors of 1064 ± 273 , 1126 ± 171 and 1091 ± 96 microstrain have been found in the normal strain component along Y for 1%, 2% and 3% of deformation along Y, respectively. Finally, along Z the systematic errors computed for the normal strain component along Z were 775 ± 211 , 1036 ± 165 and 974 ± 191 microstrain for 1%, 2% and 3% of deformation, respectively. Lower median errors were found for the components of the strains with nominal values of 0 for tests performed along each normal direction and for each deformation level (range: -160 to 147 microstrain).

Moreover, high values of standard deviation in the shear strain component along XY have been observed, for the tests with simulated deformations along X or Y, at each level tested (Figure 29 and Figure 30). This is mainly due to the high values of uncertainties for one of the specimens (Specimen 1) (see Table 1 in the Appendix).

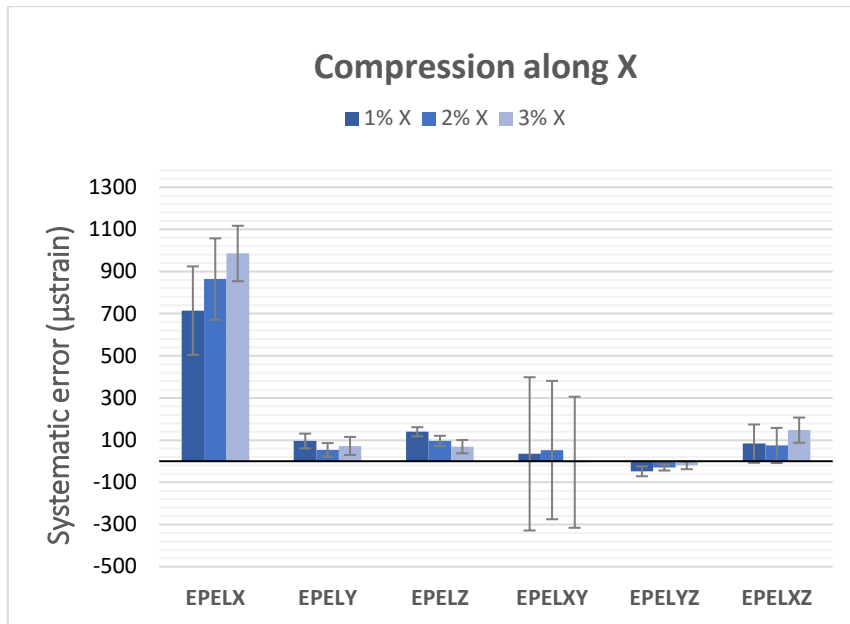


Figure 29: Median and standard deviation of the systematic error of each component of strain for 1%, 2% and 3% of deformation along X, computed over the four specimens.

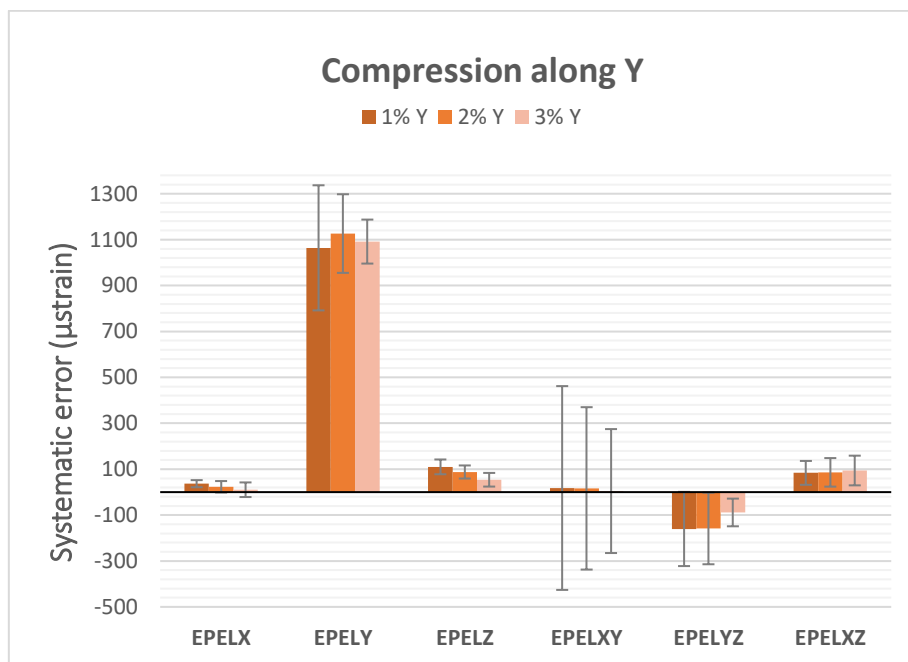


Figure 30: Median and standard deviation of the systematic error of each component of strain for 1%, 2% and 3% of deformation along Y, computed over the four specimens.

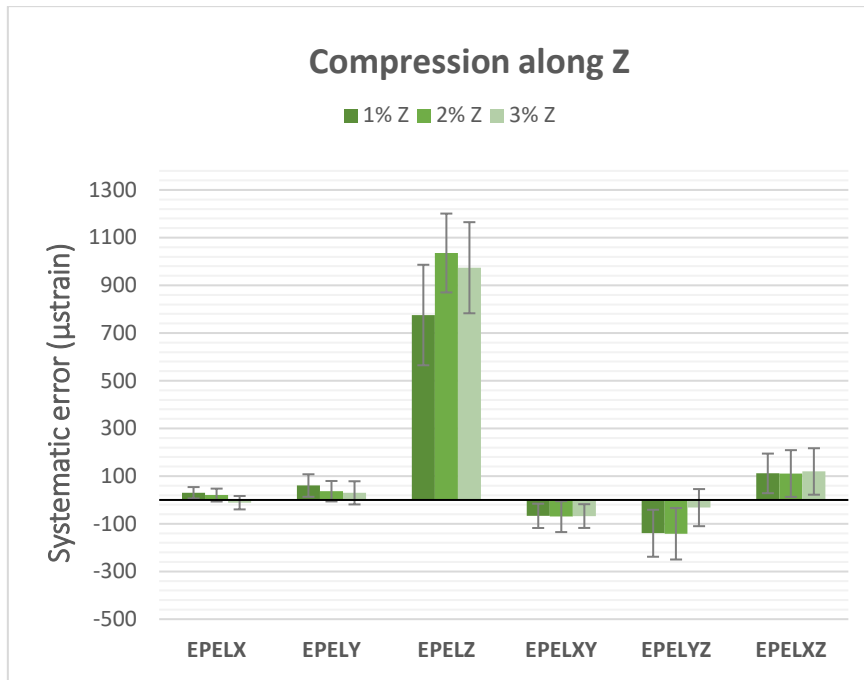


Figure 31: Median and standard deviation of the systematic error of each component of strain for 1%, 2% and 3% of deformation along Z, computed over the four specimens.

The systematic errors percentage, reported as median and standard deviation for the four specimens, have been calculated for the normal strain component along the deformation direction (Figure 32). The systematic error percentage, of imposed strain, in absolute value decreased with increasing level of simulated strain (between -10.6 and -7.1 % for 1% of deformation, between -5.6 and -4.3 % for 2% of deformation, and between -3.6 and -3.2 % for 3% of deformation).

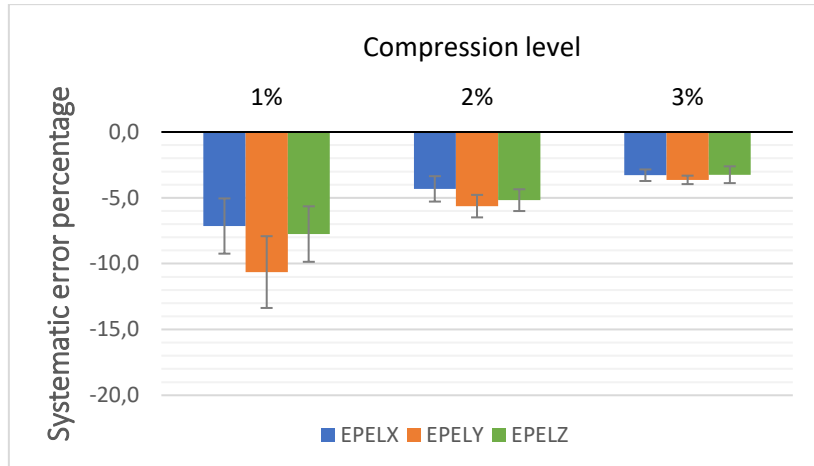


Figure 32: Median and standard deviation of the systematic error percentage of the normal strain components in the direction of deformation at different levels of simulate strain (1%, 2% and 3%), computed over the four specimens.

3.3 Random errors

For each deformation level and direction, median and standard deviation, among the four specimens, of the random error have been reported for the six components of strain (Figure 33, Figure 34 and Figure 35). The random errors of the normal strain components along the direction of deformation, were higher than those computed for the other strain components. This has been observed at each level of deformation in all the directions.

Moreover, for the normal strain components along the deformation direction, the random errors were higher for increased level of deformation, in each direction tested. In fact, the larger random errors were found in the normal strain components for 3% of deformation (3215 ± 219 , 3553 ± 359 and 3697 ± 405 microstrain for X, Y and Z deformation directions, respectively). For the 2% of deformation the random errors were 2465 ± 194 , 2745 ± 315 and 2802 ± 244 microstrain for X, Y and Z deformation directions, respectively. Finally, smaller random errors have been found for 1% of deformation: 1524 ± 65 , 1673 ± 220 and 1412 ± 175 microstrain for X, Y and Z deformation directions, respectively. Lower median random errors were found for the strain components with nominal values of 0 for tests performed along each deformation direction and for each level tested (range: 325 to 964 microstrain).

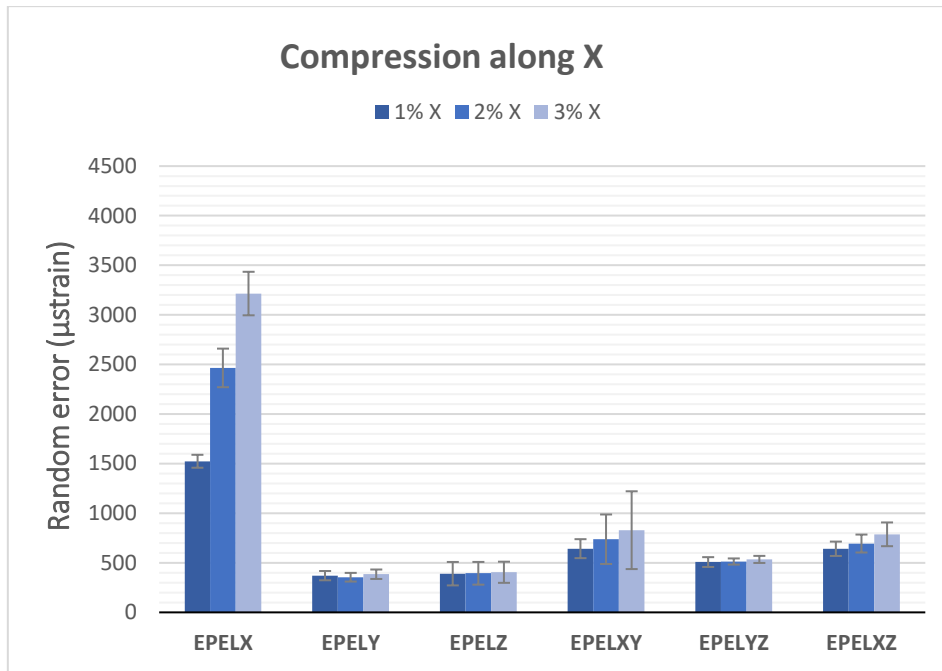


Figure 33: Median and standard deviation of the random error of each component of strain for 1%, 2% and 3% of deformation along X, computed over the four specimens.

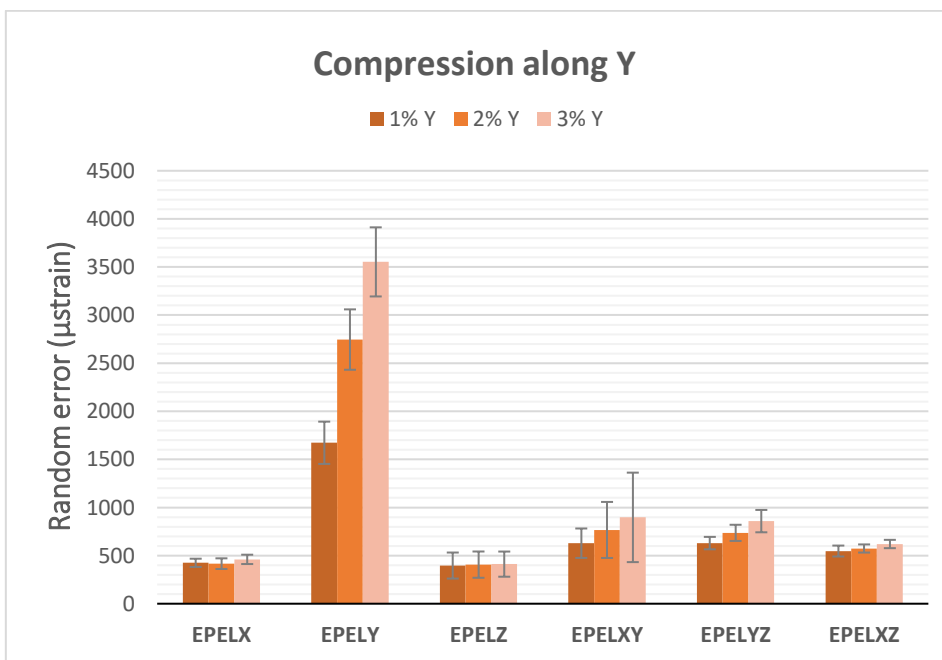


Figure 34: Median and standard deviation of the random error of each component of strain for 1%, 2% and 3% of deformation along Y, computed over the four specimens.

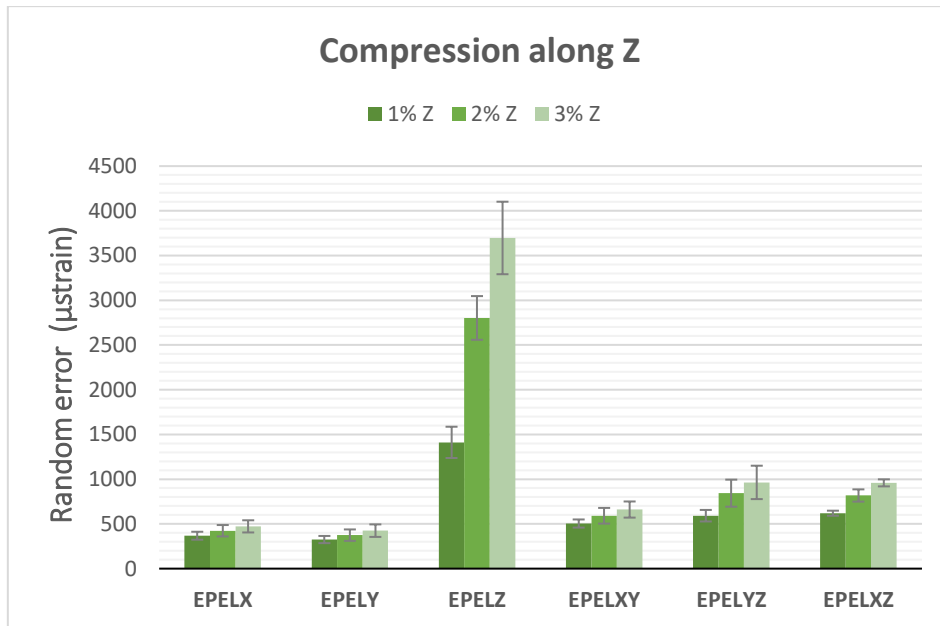


Figure 34: Median and standard deviation of the random error of each component of strain for 1%, 2% and 3% of deformation along Y, computed over the four specimens.

The medians and standard deviations, among the four specimens, of the random error percentage, have been calculated for the normal strain component along the deformation direction (Figure 36). For all the deformation levels and directions, the random error percentage ranged between 10-16 %. Moreover, in most directions, it slightly decreased with increased deformation level.

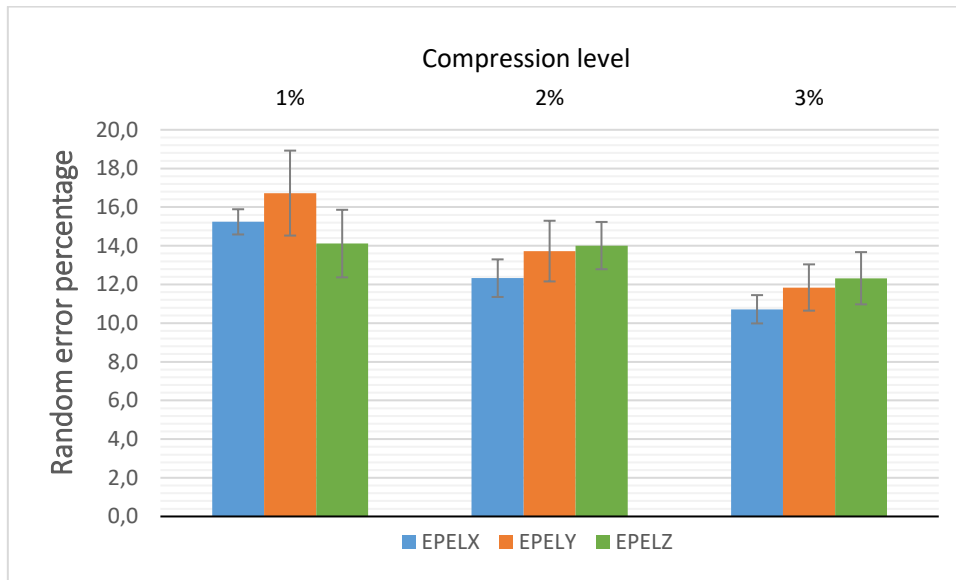


Figure 36: Median and standard deviation of the random error percentage of the normal strain components in the direction of deformation at different deformation levels (1%, 2% and 3%), computed over the four specimens.

3.4 Scalar indicators

The mean absolute error (MAER) and the standard deviation of the error (SDER) have been reported in terms of median and standard deviation among the four specimens (Figure 37 and Figure 38). As expected, higher value of MAER and SDER have been found in virtually deformed test, compare to the same value computed in zero-strain condition. This was mainly due to the normal strain component along the direction of deformation, as shown in the previous paragraphs (Systematic Errors and Random errors), which reported much higher errors. Additionally, both MAER and SDER increment with the deformation applied, in each direction tested.

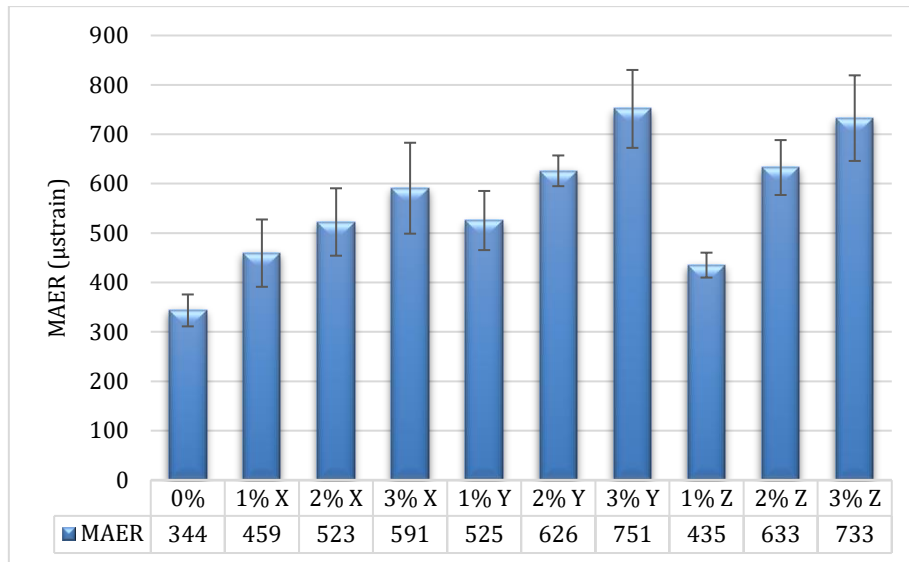


Figure 37: Median and standard deviation among the four specimens, of the mean absolute error (MAER) express in microstrain and compute for each level and direction of deformation.

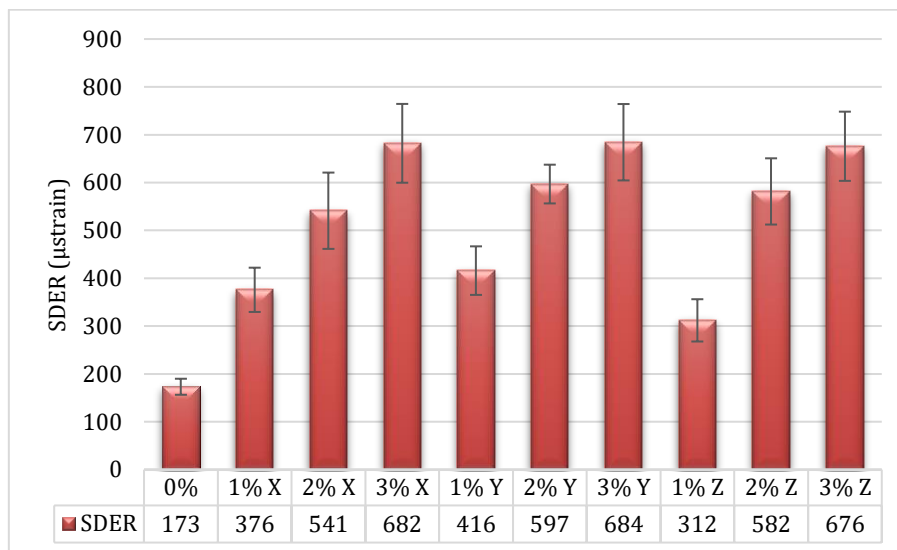


Figure 38: Median and standard deviation among the four specimens, of the standard deviation of the error (SDER) express in microstrain and compute for each level and direction of deformation.

3.5 Systematic and random errors for different nodal spacing

The median and the standard deviation over the four specimens of the systematic and random errors of the strain components have been computed for different NS (Figure 39). In particular, NS of 25, 50, 75 and 100 voxels have been used, which correspond to 40, 80, 100 and 120 μm , respectively. This analysis has been carried out for 1% of deformation along the different directions (X, Y and Z). For every NS used and deformation conditions, the systematic and random errors in the normal strain components along the directions of simulated deformation were higher than the ones computed for other strain components.

Similar values of systematic and random errors were found in function of the NS. Slightly lower systematic errors have been obtained with NS of 25 voxels, at each deformation direction. Conversely, lower random errors in the normal strain components along the deformation directions have been reached with NS equal to 100 voxels. For all the conditions tested, the systematic and random errors in the normal strain components along the deformation directions were higher for NS of 75 voxels.

The uncertainties associated with the shear strain components were one or two orders of magnitude lower than those associated to the normal strain component along the deformation direction (see Figure 1-Appendix).

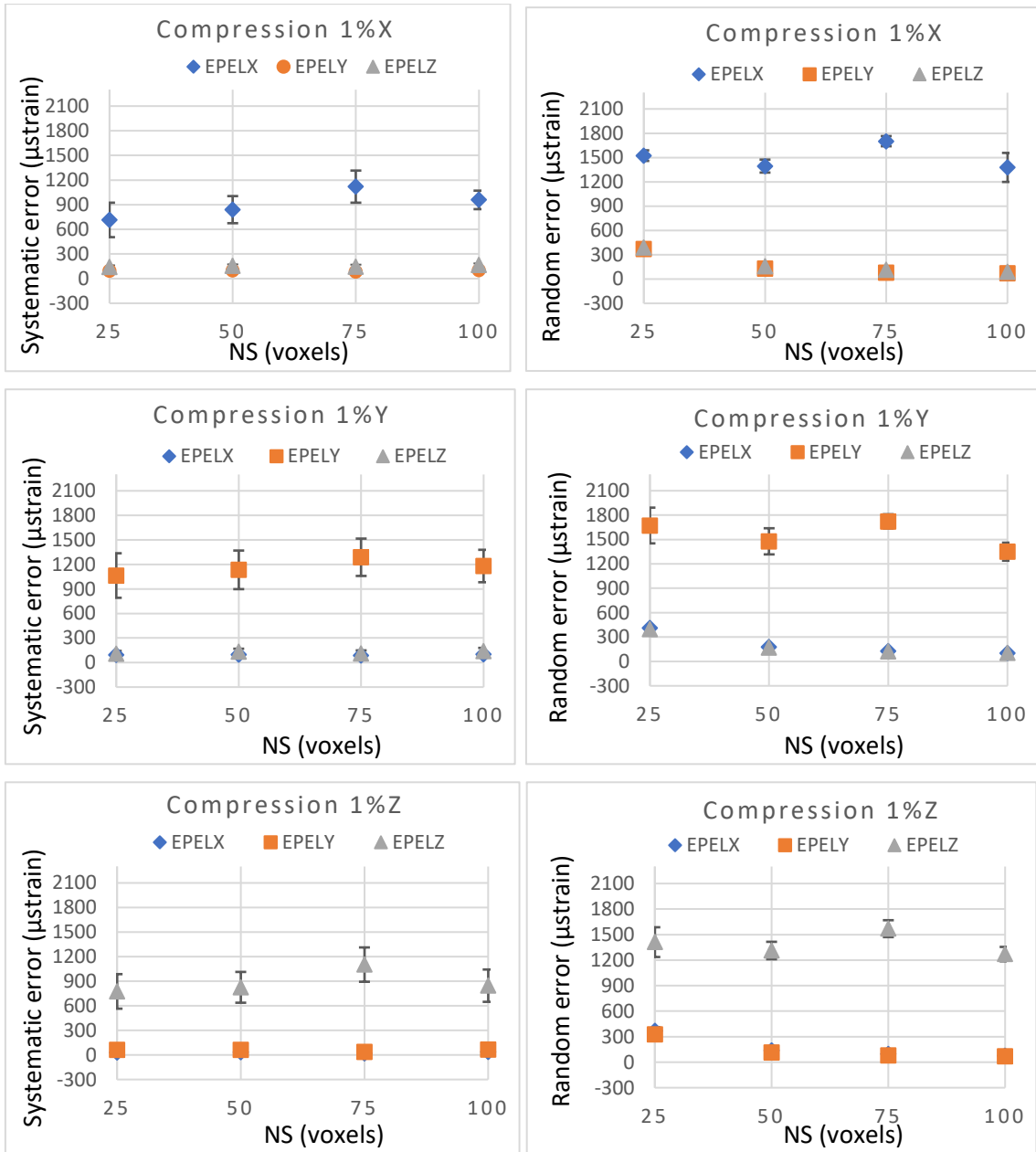


Figure 39: Mean and standard deviation of the systematic and random errors for the normal strain components (EPELX, EPEPLY and EPELZ) for different NS, computed over the four specimens. The conditions tested were 1% of virtual deformation along X, Y and Z.

3.6 Spatial distribution of the errors

The spatial distributions of the normal strain components along the deformation direction, in the middle sections of the volume of interest (VOI), have been reported for the analysis performed with NS of 25 voxels, in each condition of simulated strain (Figure 40, Figure 41 and Figure 42). All the distributions showed higher values of strain in the border, along the direction of deformation. Indeed, the errors found correspond mainly to values in the boundary regions along the deformation directions. Negative strain values appear in the centre of the section, according to the simulated deformations (-10000, -20000 and -30000 microstrain).

Also, for each condition tested, the strain distribution within the VOI appeared asymmetrical relative to the axis perpendicular to the direction of deformation. Moreover, small regions where the errors are concentrated, can be visualized in the VOIs sections (Figure 41). These zones remain in the same positions with increasing levels of simulated deformation.

Similar distribution of the normal strain component along the deformation direction has been observed for all the VOI specimens. For that reason, only one case has been reported (Specimen 2).

Finally, no concentration of errors for all the shear strain components have been shown within the VOIs sections for the different deformation condition tested. Comparable distributions have been observed between the specimens except for one (Specimen 1) (see Figure 2 and Figure 3 - Appendix).

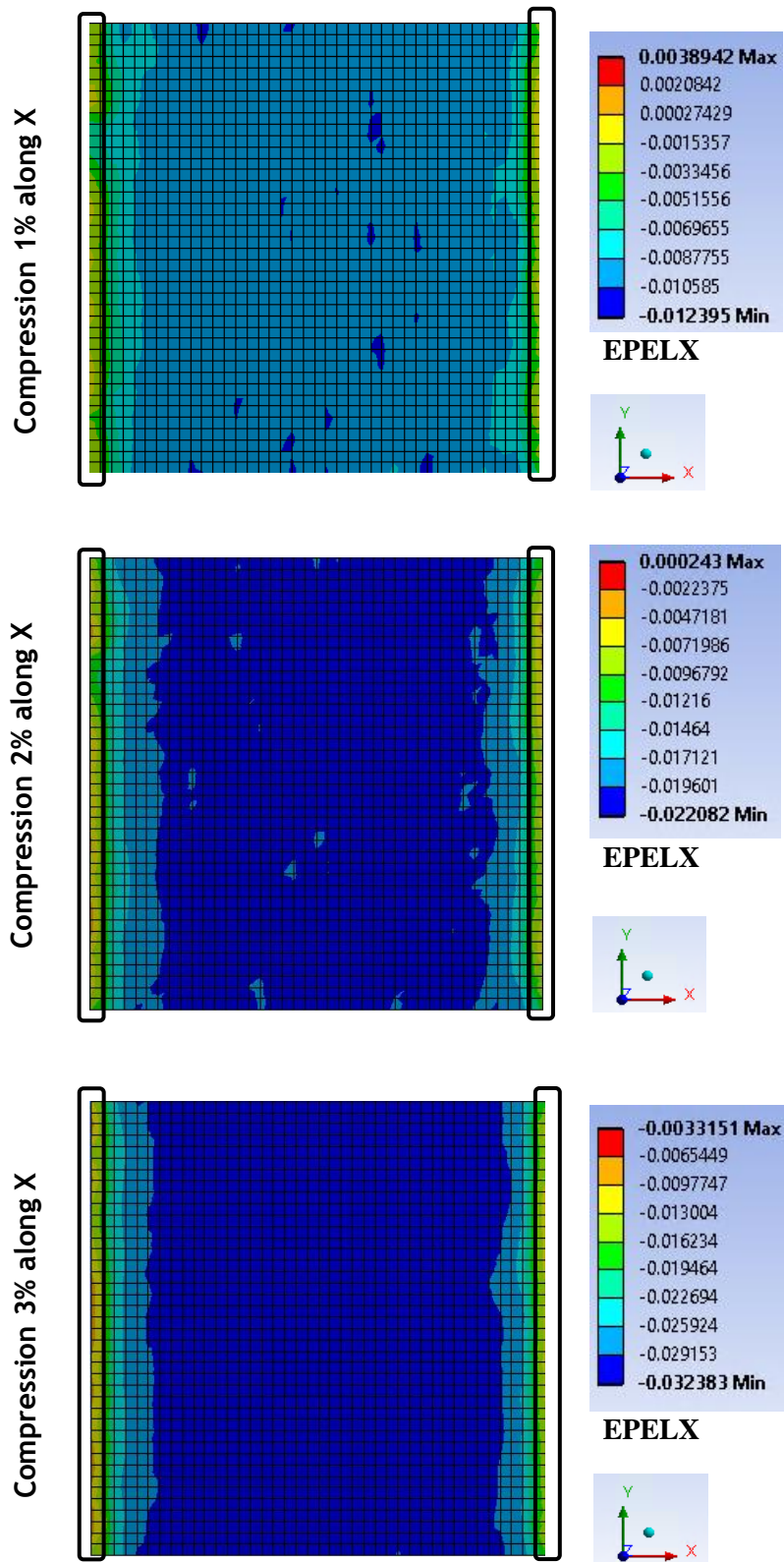


Figure 40: Spatial distribution of the normal strain component along X (EPELX), for the analysis of 25 voxels of NS, in the middle XY section of the Specimen 2 for 1% (top), 2% (middle) and 3% (bottom) of deformation along X. The black boxes highlight the removed layers nodes along the deformation direction.

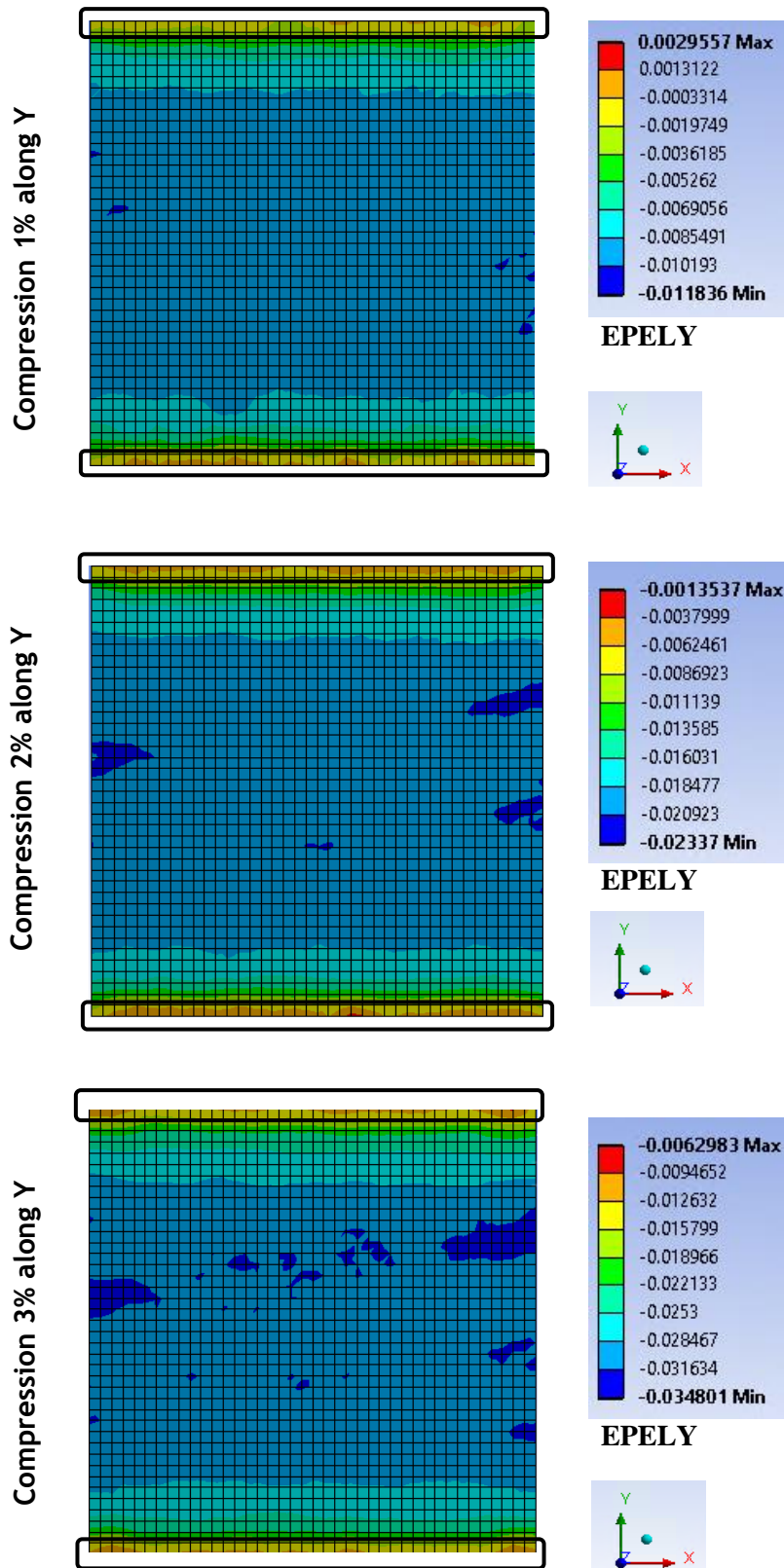


Figure 41: Spatial distribution of the normal strain component along Y (EPELY), for the analysis of 25 voxels of NS, in the middle XY section of the Specimen 2 for 1% (top), 2% (middle) and 3% (bottom) of deformation along Y. The black boxes highlight the removed layers nodes along the deformation direction.

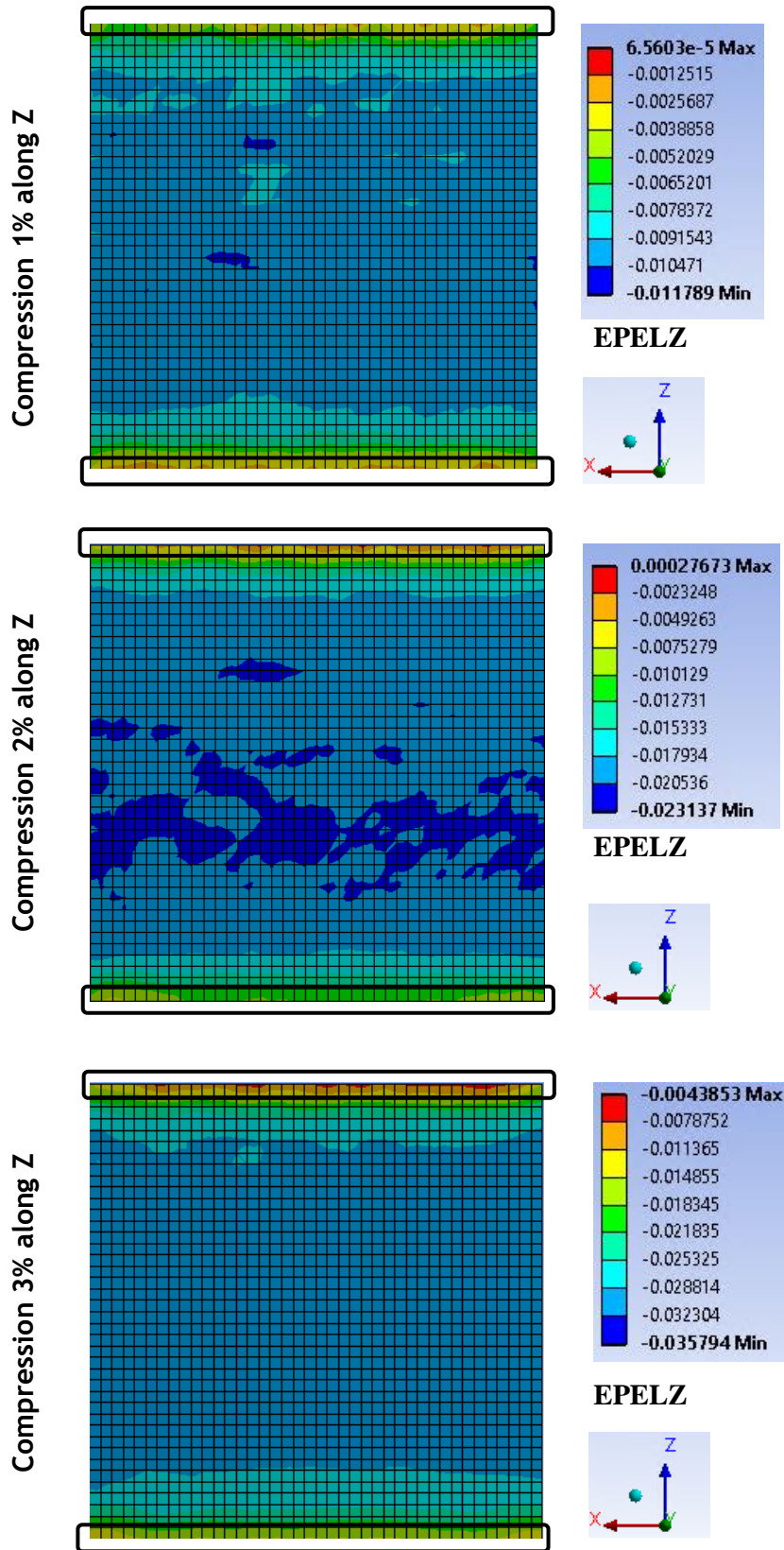


Figure 42: Spatial distribution of the normal strain component along Z (EPELZ), for the analysis of 25 voxels of NS, in the middle XZ section of the Specimen 2 for 1% (top), 2% (middle) and 3% (bottom) of deformation along Z. The black boxes highlight the removed layers nodes along the deformation direction.

3.7 Effect of the edge

Various layers of nodes in the most external cells perpendicular to the deformation direction have been removed from the strain uncertainties analysis for analysis performed with NS of 25 voxels (Figure 43, Figure 44 and Figure 45), in order to evaluate potential border effects. The layers removed have been removed symmetrically from both borders and have been expressed in physical dimension (μm). Similar trends of the systematic and random error have been found in all the specimens, therefore only one case is reported here (Specimen 2).

The systematic error of the normal strain component along the deformation direction showed a decreasing trend with increasing number layers of nodes were removed from the border. For the first layers, the systematic errors have shown a steep reduction, which then was attenuated until reaching a sort of plateau. Unexpectedly, for 2% of deformation along all the three directions, the systematic errors became negative at approximately 480 μm of the VOI excluded from the analysis (6 layers of nodes removed from both sides of the image). Similarly, for 3% of deformation along all the three directions the systematic errors turned into negative value approximately at 320 μm of the VOI removed (4 layers of nodes removed from both sides of the image). The systematic errors of the other strain components, for all the levels and directions of deformation, remained almost constant with increasing number of the removed layers of nodes.

As expected, the random error of the normal strain components along the deformation direction decreased with increased number of removed layers. The random errors of the other strain components, in all the condition tested, slightly decreased when the layers removed increased. The value where the random error of the normal strain component reaches the random error of the other strain component, depends on the level as well as the direction of deformation. This point ranged between 240 and 560 μm .

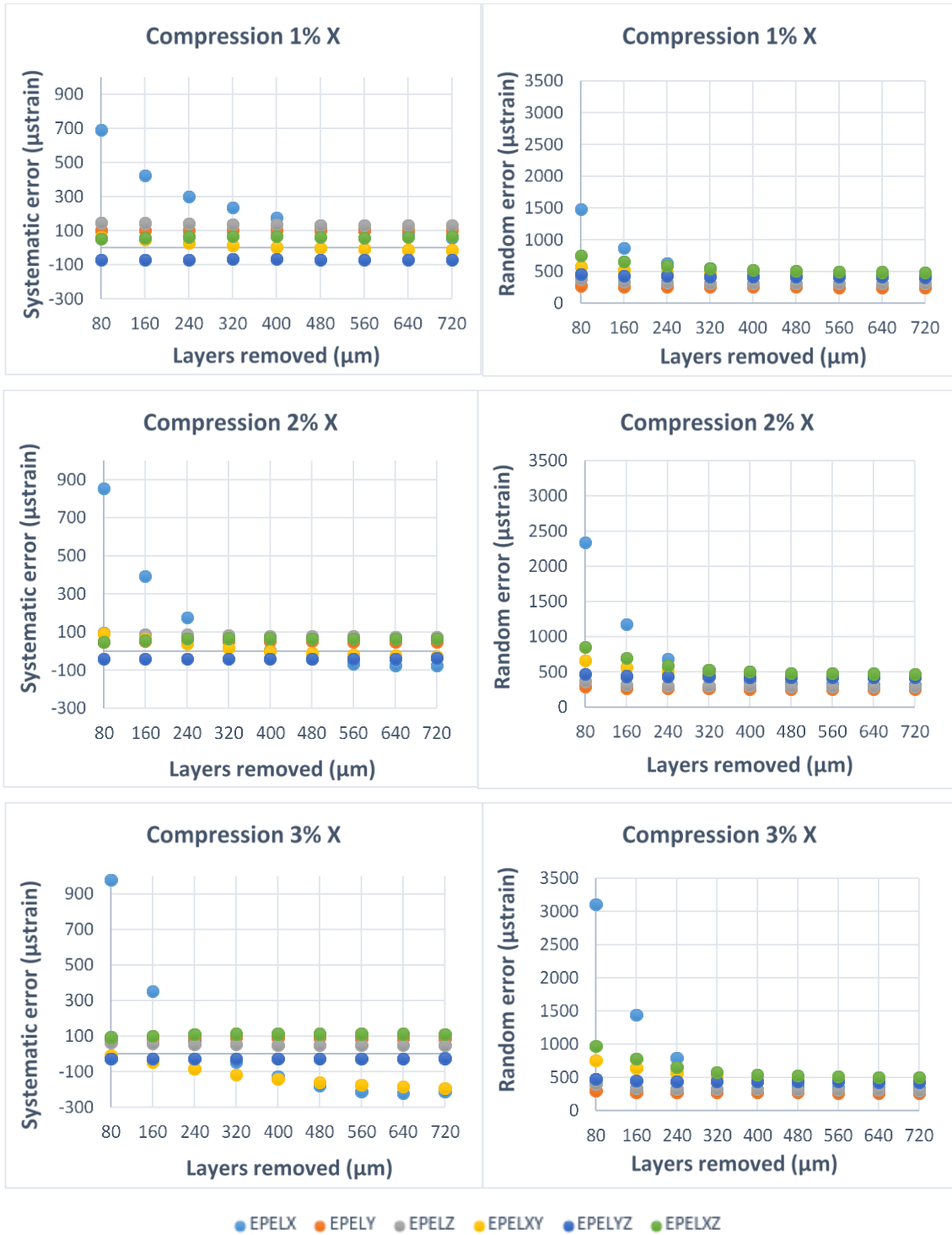


Figure 43: Systematic and random errors of the six components of strain, for each level of deformation along X, in function of the layers of the Specimen 2 VOI removed in the deformation direction (X).

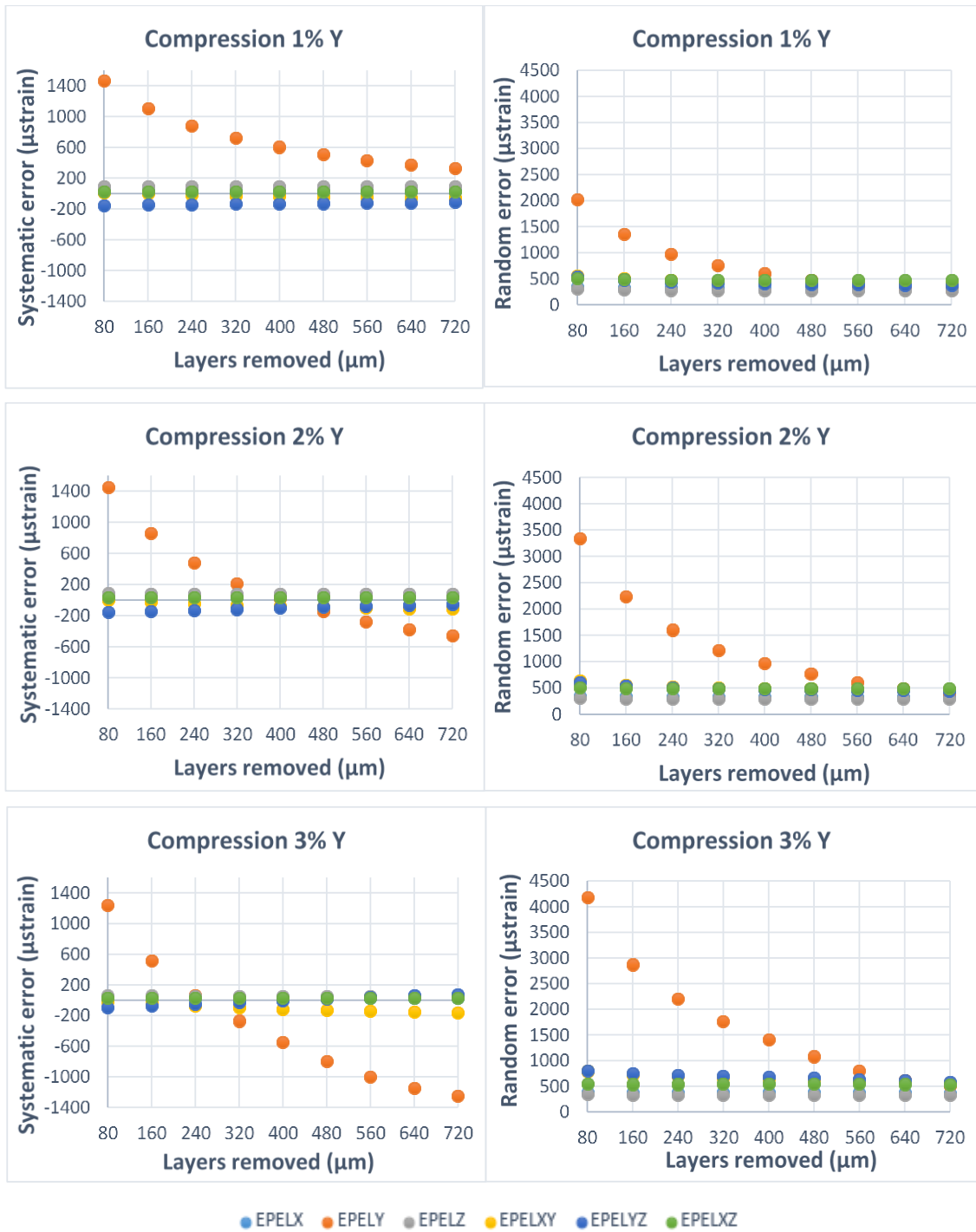


Figure 44: Systematic and random errors of the six components of strain, for each level of deformation along Y, in function of the layers of the Specimen 2 VOI removed in the deformation direction (Y).

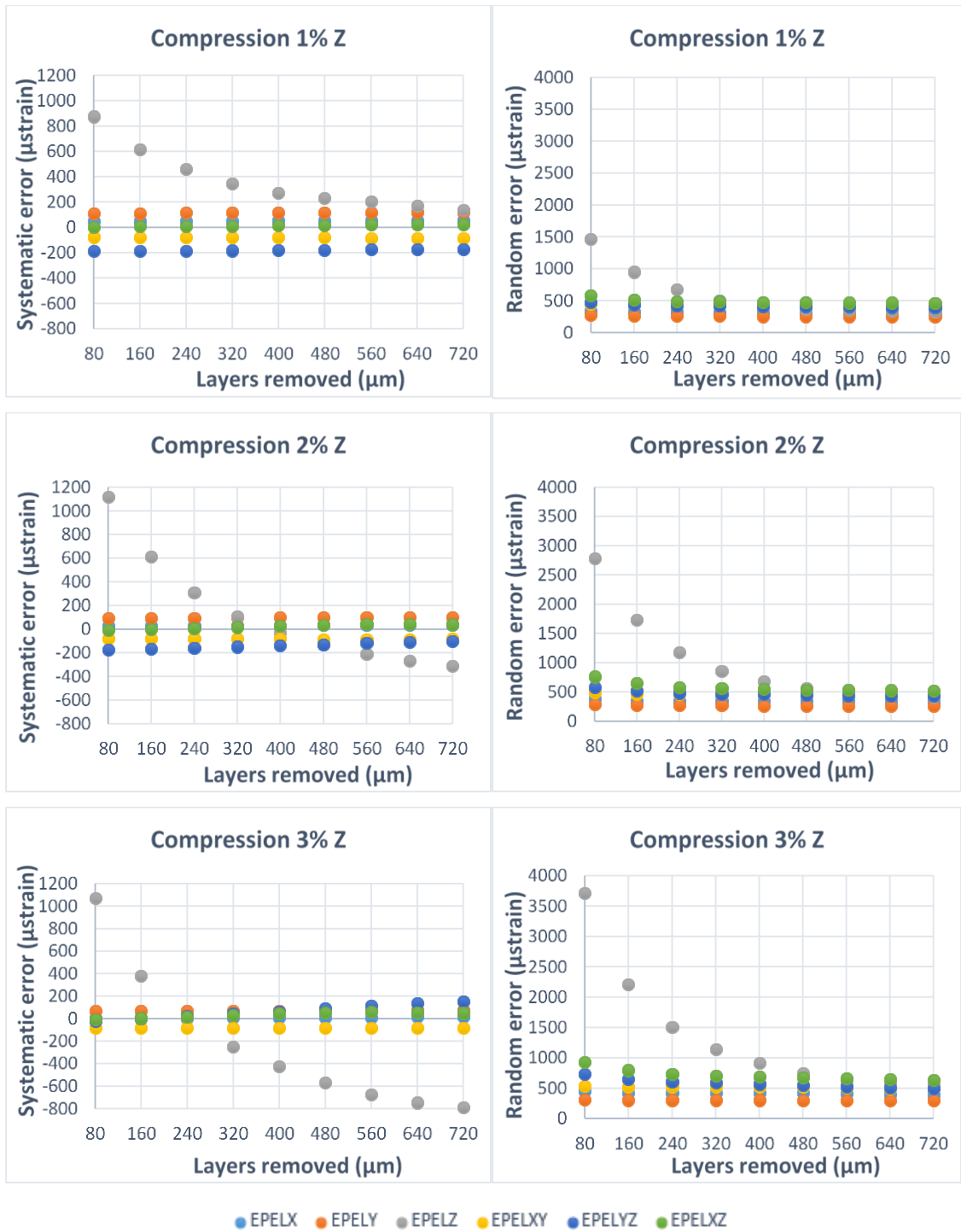


Figure 45: Systematic and random errors of the six components of strain, for each level of deformation along Z, in function of the layers of the Specimen 2 VOI removed in the deformation direction (Z).

In order to better understand the effect removing the layers of nodes on the uncertainties, some examples of the frequency plots have been reported (Figure 46, Figure 47, Figure 48 and Figure 49). The distribution of the normal strain component along the deformation direction showed how the shorter peaks, at higher strain value, have been removed when more layers of nodes are excluded from the analysis (Figure 46 and Figure 47). However, the principal peak of the strain distribution remained in the same position, even if the external nodes have been removed.

The frequency plots of the strain component along XY have been reported for the Specimen 1. In that case, the errors of the shear component have been the highest when deformation of 2% and 3% along X or Y were applied (Figure 48 and Figure 49). The strain distribution appeared more symmetric when additional layers of nodes are removed from the border. Still, the peaks in the frequency plots remained almost in the same position.

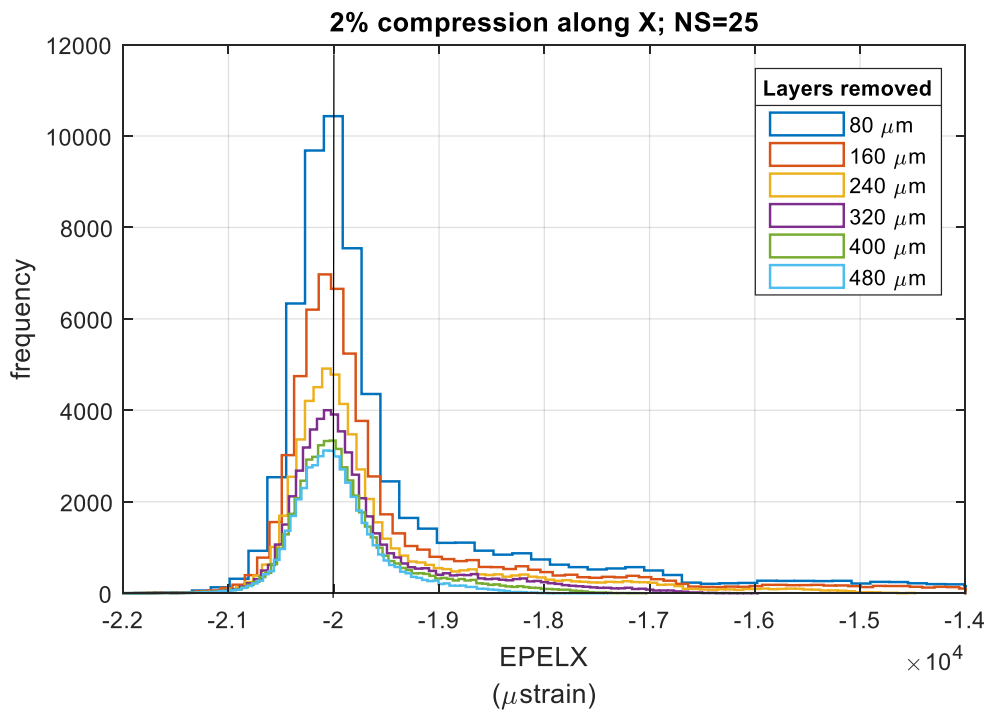


Figure 46: Frequency plots of the normal strain component along X (EPELX) after removing different layers of nodes (from 80 to 480 μm) along X. The example shown is the Specimen 1 after 2% of deformation along X. The black vertical line highlights the nominal virtual deformation applied on the strain component considered.

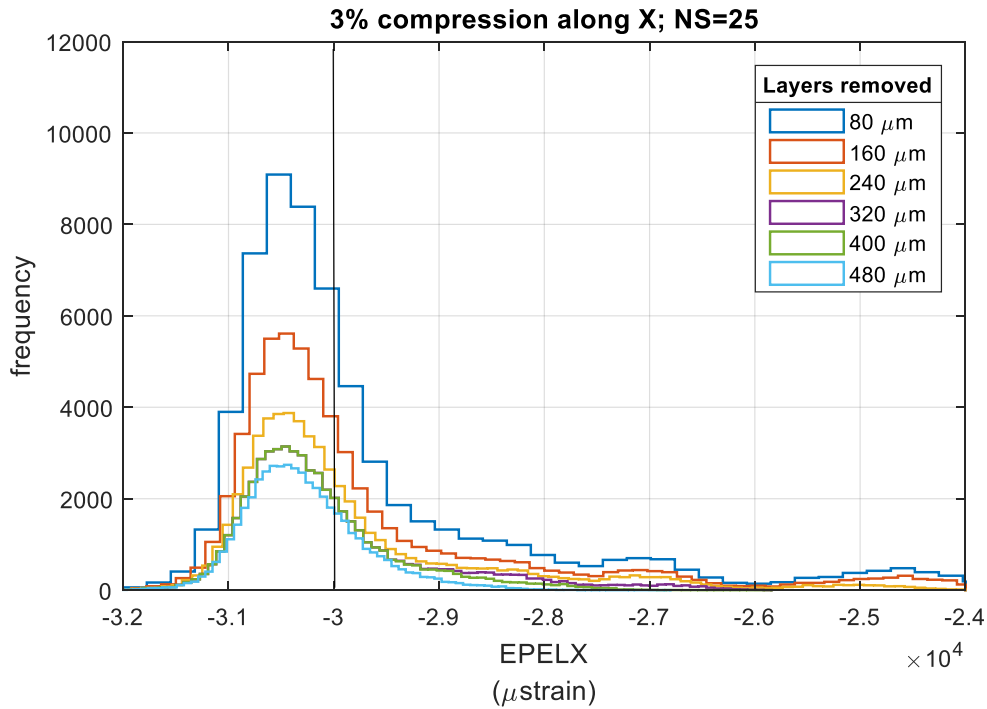


Figure 47: Frequency plots of the normal strain component along X (EPELX) after removing different layers of nodes (from 80 to 480 μm) along X. The example shown is the Specimen 1 after 3% of deformation along X. The black vertical line highlights the nominal virtual deformation applied on the strain component considered.

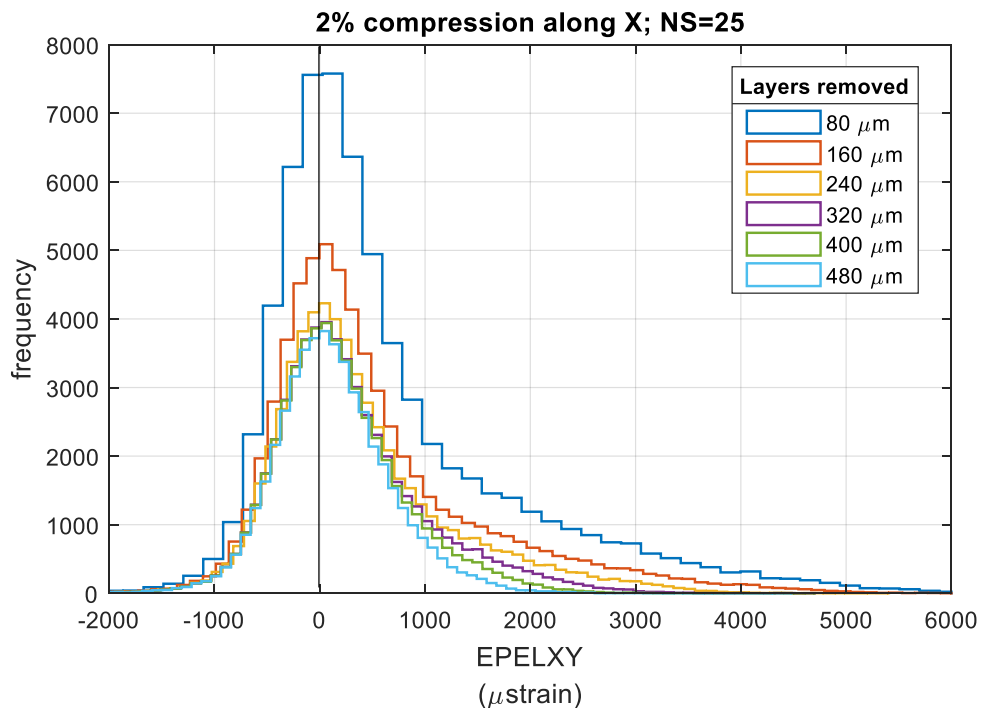


Figure 48: Frequency plots of the shear strain component along XY (EPELXY) after removing different layers of nodes (from 80 to 480 μm) along X. The example shown is the Specimen 1 after 2% of deformation along X. The black vertical line highlights the nominal virtual deformation applied on the strain component considered.

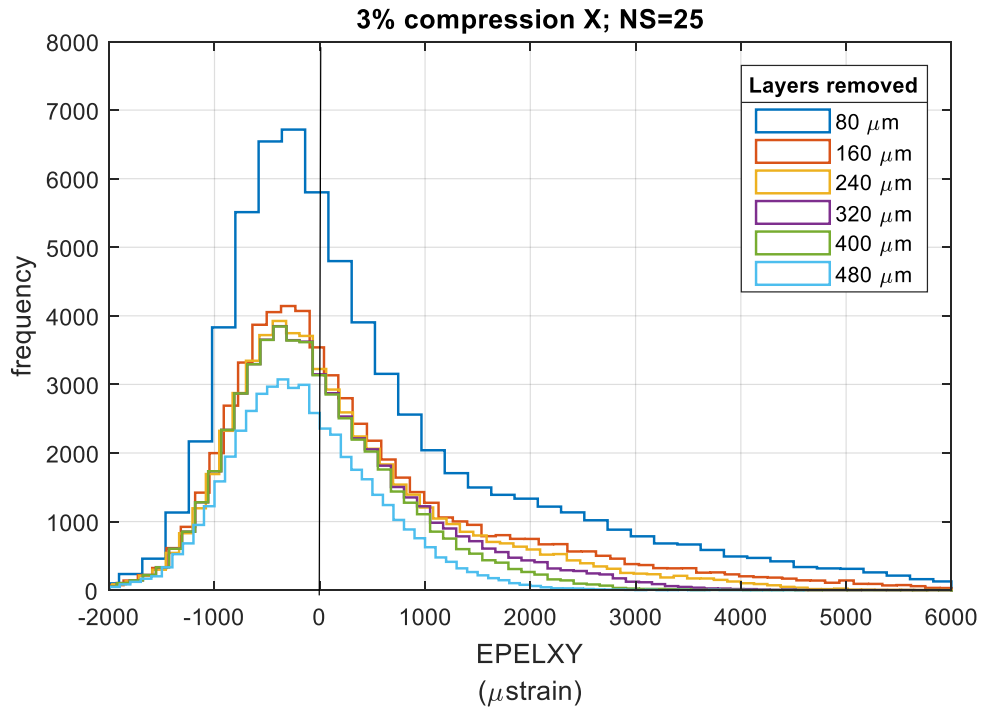


Figure 49: Frequency plots of the shear strain component along XY ($EPELXY$) after removing different layers of nodes (from 80 to 480 μm) along X. The example shown is the Specimen 1 after 3% of deformation along X. The black vertical line highlights the nominal virtual deformation applied on the strain component considered.

3.8 Composed deformation

In a further analysis, the systematic and random errors were computed after a virtual deformation in different directions (Table 4). Deformations of 1% have been performed long X, Y and Z, simultaneously. As expected, the frequency plots of all the normal strain components showed a peak approximately in the nominal strain (-10000 μ strain) (Figure 50). However, the distribution of the shear strain components appeared less centred in the nominal strain (0 μ strain) (Figure 51).

	X	Y	Z	XY	YZ	XZ
Systematic Error (μstrain)	529	731	753	44	-459	273
Random Error (μstrain)	1351	1539	1465	666	728	655

Table 4: Systematic and random errors of the all strain component computed with NS of 25 after 1% of deformation along X, Y and Z, simultaneously.

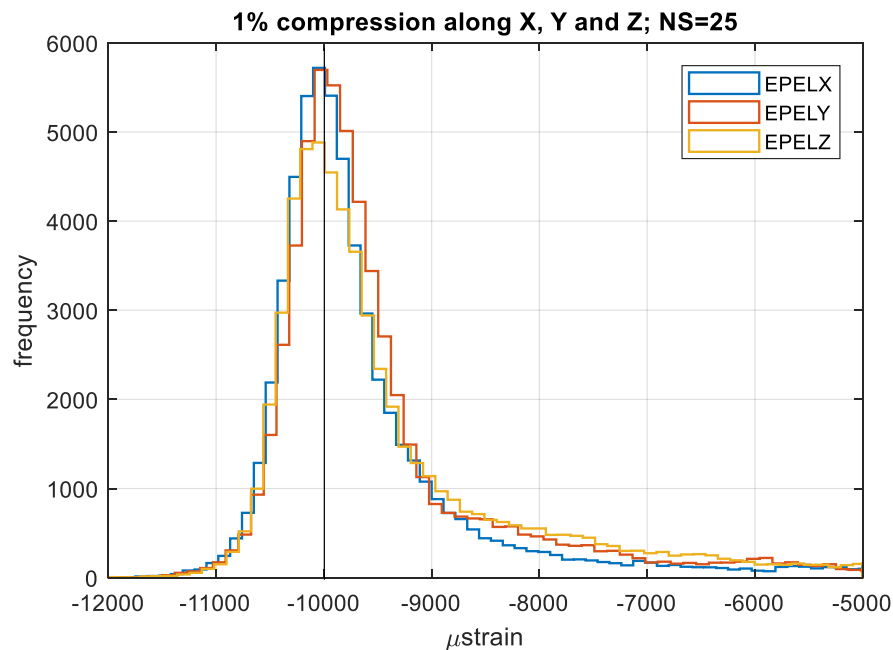


Figure 50: Frequency plot of the normal strain components (EPELX, EPELY and EPELZ) in the Specimen 3 for the simultaneous deformation of 1% along X, Y and Z. The black vertical line highlights the nominal virtual deformation applied on the strain component considered.

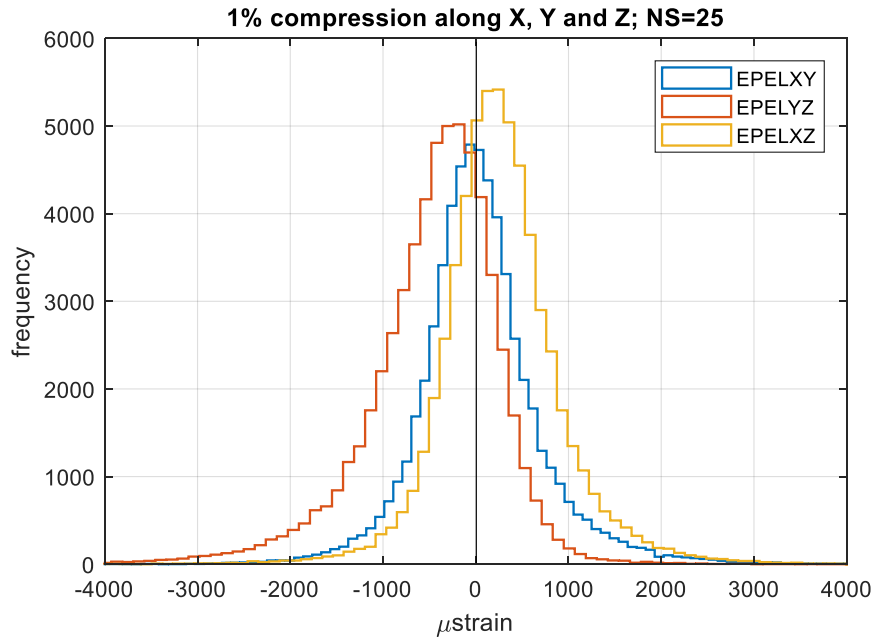


Figure 51: Frequency plot of the shear strain components (EPELXY, EPELYZ and EPELXZ) in the Specimen 3 for the simultaneous deformation of 1% along X, Y and Z. The black vertical line highlights the nominal virtual deformation applied on the strain component considered.

4. Discussion

As shown in two previous studies, using synchrotron radiation micro-CT images, the uncertainties of the DVC can be reduced, allowing strain measurements within the BSUs (Christen et al., 2012, Palanca et al., 2017). However, to evaluate the errors of this DVC approach, only zero-strain test or virtually-moved test have been used so far. In the latter case, the uncertainties are underestimated, as the image noise could be traced as a feature of the image during the registration (Dall'Ara et al., 2014). On the other hand, a zero-strain approach is based on repeated scan, so it can include the noise in the image, but it could be not enough to justify the errors, when deformation under loading needs to be computed.

In order to integrate the knowledge and the possible applications of this powerful technique, a wider evaluation of the uncertainties is required. The goal of this work was to estimate the systematic and random error on strain measures of SR micro-CT image-based DVC. Applying different virtual homogeneous deformations on the repeated scan of cortical bone specimens, the uncertainties can be evaluated and, therefore, integrated with the results of the previous studies.

Uncertainties on different components from zero-strain analyses

In order to see any directionality of the DVC uncertainties, this study was focused on the systematic and random error for the single components of strain. Using a NS of 40 μm , the zero-strain components showed systematic errors ranged between -160 and 140 microstrain. Instead, the random errors were always between 300 and 1000 microstrain. However, no prevalent direction of both systematic and random errors on the zero-strain components have been observed. Consistently, no evident difference between errors in the normal and shear strain components was found previously in the literature. For instance, a recent study evaluated the DVC errors in zero strain condition using micro-CT scans of porcine augmented vertebral bodies (Tozzi et al., 2017). In that work, the strain uncertainties for all components and all the VOIs, with a sub-volume of 48 voxels (approximately 1900 μm), were lower than 200 microstrain, using the same

global DVC approach used in this study (ShIRT-FE) and the systematic and random errors seemed not to be affected by the specific components of strain. The main reason of the lower random errors found in that study compared to the value found in the current work is the difference in the used sub-volume size (Tozzi et al. used a sub-volume size almost 50 times larger than the one used in that study).

In a different work, conducted on bovine cortical and trabecular bone specimens, using a micro-CT image-based DVC, similar errors for all the six components of strain were found (Palanca et al., 2015). In that study, in a repeated-scan-test (using a NS of approximately 500 μm), the errors were slightly larger for the normal strain component along Y (in the cortical specimen 924 and 663 microstrain for the systematic and random error, respectively), even if the axis of rotation of the specimen during the micro-CT imaging was the Z-axis. Furthermore, no difference between normal and shear components have been observed. In the last case (repeated-test) the systematic errors were higher compare to the current study. This is mainly due to the high image quality and higher signal to noise ratio that the SR-microCT allows to achieve (Palanca et al., 2017).

Finally, a previous work, conducted on trabecular bone, using a local DVC approach (DaVis-FFT), was focused on the different strain components (Gillard et al., 2014). In particular, the stationary test (or repeated scan) showed systematic error that varied between -40 and 40 microstrain with sub-volume size of 64 voxels (voxel size of 24.6 μm , for a total sub-volume size of approximately 1574 μm) and the normal component along Z direction exhibited the most variation between slices. In that study, the random errors of the strain components were up to 200 microstrain and smaller. Again, the smaller errors achieved in that study were due to the large sub-volume size used (approximately 40 times larger than the current study).

After all, the evaluation of the single strain components was important to investigate the presence of errors directionality in the DVC measurements. The results of this work can be therefore useful for further works that want to study the errors distribution in the strain components, also in different condition, in terms of resolutions or parameters within the DVC algorithm.

Effect of the virtual deformation

To better understand the effect of the virtual deformation on the DVC uncertainties, the results of this study were compared to the zero-strain tests (gold standard). Moreover, in order to give a quantitative comparison with published literature, the MAER and SDER (sometimes referred as “accuracy” and “precision” errors, respectively) have been computed. In this work, the MAER ranged between 435 (1% deformation along Z direction) and 751 (3% deformation along Y direction) microstrain while the SDER ranged between 312 (1% deformation along Z direction) and 684 (3% deformation along Y direction) microstrain, with a spatial resolution of the measure of 40 μm (nodal spacing equal to 25 voxels). Both errors were higher compared to the ones obtained in zero-strain tests with repeated SR-microCT scans of the same specimens (approximately 300 and 150 microstrain for MAER and SDER, respectively) (Palanca et al., 2017). This difference was mainly due to the higher errors in the normal strain component along the deformation direction, observed in this study.

In the first DVC application (Bay et al., 1999), the SDER was found to be approximately 300 microstrain for DVC measurements performed on microCT scans of trabecular bone specimens and by using a nodal spacing of 61 voxels, equivalent to a spatial resolution of the measurement of approximately 2 mm. Similarly, Liu and Morgan (2007) reported SDER values between 345 and 794 microstrain across different trabecular bone specimens, with a spatial resolution of the measurement of approximately 1500 μm . These results confirm that the precision obtainable with SR-microCT based DVC analyses can increase dramatically the spatial resolution of the measurements, even in case the uncertainties are evaluated under loading.

A different study performed a virtually-moved test on SR- micro CT images of femur mice specimens (Christen et al., 2012). The precision ranged between 11000 and 13000 microstrain the spatial resolution of the measure was 10 μm . Those high errors were mainly due to the higher spatial resolutions achieved in that study. In the same work, the systematic errors found were not significantly different from zero. However, measurements from virtually moved or deformed test leads to underestimate the errors, as the image noise is not considered. Instead, on the present study, for the first time, both the noise and the virtual deformation have been considered in the uncertainties analysis of a SR-micro CT image-based DVC.

Finally, the MAER and SDER (435-751 microstrain and 321-684 microstrain, respectively), obtained in the present work for loaded images and DVC nodal spacing of 40 μm , are not acceptable for applications where small strains need to be measured. For example, in case physiological deformations of approximately 2000 microstrain are looked for, a precision of 200 microstrain should be used. For such analyses a further optimisation of the scanning and DVC parameters should be performed. Nevertheless, it should be noted that high errors were localised in the border of the image (see next sections) and therefore better precision and accuracy is expected in the centre of the image. Considering that the bone yields at deformation of approximately 10000 microstrain in compression and 7000 microstrain in tension (Bayraktar et al., 2004), the DVC method would be able to discriminate between regions above yield.

Effect of the deformation level

The results showed a systematic error of the normal strain component, along the deformation direction, approximately 1000 microstrain at each tested condition, driven by large errors in the border of the image. Indeed, the systematic error percentage was reduced when the nominal deformation increased, along each direction. On the other hand, the random error increased with higher deformation levels and the random error percentage was between 10% and 15% of the applied deformation. That was consistent for all the direction of applied virtual deformation.

Although smaller errors were expected, these uncertainties would still allow for the classification of the highly deformed regions from the rest of the tissue, for correct investigations of the regions close to failure or already failed.

The effect of the nominal deformation level on the DVC uncertainties may be due to that fact that when small deformations occur, the effect of the image noise would play a large role in the DVC algorithm, and for higher level of deformation the homogeneous displacement along a certain direction may be beneficial for the DVC algorithm. However, it should be noted that the highest level of nominal deformation considered (3%) is already over the value the bone is expected to yield (which is around 1% of deformation in cortical bone) (Bayraktar et al., 2004). This test was done to investigate the uncertainties of the algorithm if applied to largely deformed specimens.

In a recent study, polymer and cemented trabecular bone specimens have been examined under step-wise uniaxial compression and the strain were computed with a local DVC approach (Davis-FFT) applied to micro-CT images (sub-volume size of 64-96 voxels, voxel size of 30 μm) (Zhu et al., 2016). Even though the input images and the DVC algorithm used in that study were substantially different than those used in this study, some similarities could be observed. In fact, in that study the authors found that the random error of the component along the direction of compression decreased with the increase of mean compressive strain, initially drastically but then gradually. Moreover, in that study, the random errors of both foam and bone–cement specimens were always below 10% of the applied strain. Considering that the uncertainties were computed with a repeated scan test, probably the errors under load would be higher, which is expected considering the lower resolution of the considered images.

Finally, the effect of the deformation level has been revealed in this work for both the systematic and random errors. The errors in the other components of strain have not shown a dependency on the level of induced nominal strain in one of the components. The results could be useful for future studies where the level of compression or virtual deformation to be applied on the specimen needs to be optimised.

Effect of the deformation direction

For all the tested conditions, no effect of the deformation direction (X, Y or Z) has been observed on the amount of systematic and random errors, for all strain components. This is probably due to the homogeneous and isotropic distributions of the features (cortical porosities) within each specimen. The independency of the uncertainties levels with respect to the deformation direction has confirmed the potential of the DVC approach to measure different loading scenarios. It remains to be investigated how much a combined deformation along more than one directions would affect the DVC uncertainties.

Furthermore, the systematic and random errors for the measurement of the normal strain component, computed after a virtual deformation in different directions simultaneously, were lower compared to the same errors after the uniaxial deformation.

This could be due to interactions between the strain component on the systematic and random errors. However, it should be considered that this test is purely theoretical as the triaxial scaling does not conserve the volume of the specimen and, therefore, is not representative of a compression applied to an incompressible material as bone.

Effect of the specimen

In general, lower variability between specimens in the systematic and random errors for the different strain components have been showed, except for one case. Indeed, for the XY shear strain component a high variability in the systematic errors has been observed for all levels of compression along X and Y and in the random error for 3% of compression along X and Y. This unexpected effect was due to one specimen (Specimen 1) associated to high value of systematic and random errors in those deformation conditions (Table 1 - Appendix). A possible explanation for this phenomenon could be the morphologic structure and orientation of the features in the VOI image of the specimen. However, to the author' best knowledge, inter-specimen variations and potential outliers have not been considered before at the local level and in different cortical structure.

A previous study conducted on microCT images of different trabecular bone structures in both simulated and real displacement fields, showed how the strain errors depended on the sample microstructure (Liu and Morgan, 2007). In particular, the accuracy and precision were highest for specimens with lower volume fraction and trabecular number, and higher trabecular spacing and structural model index. However, in that study only the evaluations of the MAER and SDER were performed and errors on the different strain components have not been performed. On the other hand, a recent study, conducted at zero strain condition on augmented porcine vertebrae (at organ level), showed how the systematic and random errors were not particularly related to the bone microarchitecture and, therefore, the local heterogeneities should not affect the precision of the DVC (Tozzi et al., 2017). Moreover, a similar works, conducted for natural and augmented porcine vertebral bodies (at the organ-level and at zero strain condition), showed a possible variability in the errors of some strain component due to higher errors in some specimens (Palanca et al., 2016), confirming the potential sensibility of the DVC outputs among the considered specimens.

Finally, the result reported in this study could suggest a possible interaction between the specimen features orientation and the uncertainties when deformation is applied. However, more specimens of cortical bone with different microstructures need to be tested to better understand the inter-specimen variability in the DVC uncertainties and confirmed this hypothesis.

Effect of the Nodal Spacing

No clear trend has been observed for both systematic and random errors in the normal strain components, along the compression directions, in function of the tested NS. Instead, the errors of the other strain component showed trends consistent with a work in the literature performed on repeated scans (Dall'Ara et al., 2014, Dall'Ara et al., 2017). That study reported that the NS choice should be a trade-off between resolution and errors of the measures. In fact, the larger is the NS, the lower is the random error. Moreover, if the NS increase, the spatial resolution of the method is reduced. The DVC algorithm trilinearly interpolates within the cell of the computational grid so, when NS increase, the DVC may miss heterogeneities in the strain field.

However, the choice of the NS is not trivial, due to the different dimensional scale of the features within the cortical bone. Indeed, the typical dimension of the osteons is 200-300 μm in diameter, the haversian canals 40-100 μm and the lacunae 10-30 μm (Cowin, 2001). The reason of the oscillatory trends in the errors of the strain components under load are still not clear. With a NS of 50 voxels (80 μm) the random error was slightly better compared to the same error compute with NS of 25 voxels (40 μm). But in the latter case the number of measurements (nodes of the computational grid) within the volume of interest was much smaller (Table 5). For NS of 75 voxels (120 μm) both systematic and random error increased. Then, for 100 voxels (160 μm) of nodal spacing an improvement in the errors have been observed. A possible explanation of this trend could be that, after a decrease as a power law, the error is oscillating around an asymptote. Therefore, further analysis, with more nodal spacing, should be performed in order to confirm this hypothesis.

Finally, even if the trends of the errors of the strain component under load are different from the component at zero strain, the NS of 25 voxels (40 μm) still provided a

good compromise between spatial resolution and errors in the strain measurements. This result confirmed what had been shown in a previous study (Palanca et al., 2017).

Nodal spacing (Voxels)	Nodal spacing (μm)	Number of nodes inside VOI	Number of nodes excluding the border
25	40	68921	65559
50	80	9261	8379
75	120	3375	2925
100	160	1331	1089

Table 5: Number of the strain measures inside the VOI (1000x1000x1000 voxels) for each nodal spacing used.

Effect of the border

The distribution of the normal strain component along the loading direction, showed that the errors were concentrate in the border of the VOI, perpendicular to the deformation directions. This effect was more evident when the level of deformation increased, and it was consistent in each specimen analysed. Moreover, this phenomenon does not involve only the first layer, but it propagates towards the centre of the image, for a few layers. In fact, if more nodes were excluded from the uncertainties analysis, both random and systematic errors decreased.

A possible explanation of this result could be linked to the DVC global approach used in this study (ShIRT). In fact, in this method each node of the computational grid is affected by the neighbour nodes (Barber and Hose, 2005; Barber et al., 2007; Dall'Ara et al., 2014) and, when the border is shifted due to the applied virtual compression, increasing the gradient in grey values between the border and the bone voxels. As a consequence, a few nodes next to the external nodes could be influence by this artefact. If this is the main reason of this observation a local DVC approach may be less influences. However, to the author's knowledge, no comparable studies on uniaxial or triaxial virtual deformed tests at the tissue level exist in literature to confirm this hypothesis.

Furthermore, in this work, uniform distributions of the components at zero strain have been shown within the considered volumes for the different tested deformations.

These results were consistent with a previous study conducted in zero-strain condition, using the same DVC approach and cortical bone specimens, (Palanca et al., 2017).

Finally, in order to avoid the errors in the border of the VOI, a certain distance from each side of the border, which should be optimised according to the different applications, is recommended.

4.1 Limitations and potentials future works

The main limitation of this work is the low number of tested specimens (only 4 specimens). More cortical bone specimens with different morphological structures need to be tested in order to clarify the effect of the specimen's properties with respect to the uncertainties analyses. This could help to justify the high variability for one strain component found in this study due to one specimen. Moreover, different specimens size should be explored in order to understand if the "border effect" described previously may depend on the physical dimension of the specimen.

Another limitation of this work is the bovine bone tissue used, instead of human ones. In order to define the exact parameters of the DVC algorithm for clinical and preclinical application, human or mice bone specimens need to be use in future studies.

Furthermore, homogeneous deformations have been virtually applied to the specimens, in particular, uniaxial affine compression and triaxial scaling. More virtual deformation scenarios (such as tension or torsion) and in different level should be tested. In particular, in future studies the uncertainties in strain measurements of the DVC algorithm should be tested under realistic heterogeneous strain field. For instance, this analysis could be done by imposing a realistic 3D field of displacements derived from finite element models applied to the bone structures (Dall'Ara et al., 2017).

Lastly, only a global DVC approach has been used in this work to estimate the uncertainties associate to the strain measures. It would be interesting to explore the uncertainties of a local DVC algorithm evaluated with virtually loaded repeated images.

5. Conclusion

A new method to evaluate the DVC accuracy and precision in strain measurements on cortical bone SR- microCT images is reported in this work. In order to better understand the DVC uncertainties, different virtual deformation have been applied on the repeated scans of cortical bone specimens.

As expected, the systematic and random errors of the normal strain components along the deformation direction were higher than the errors in the other components, in all the condition tested. The estimated systematic error for 1% of nominal compression was approximately 10% of the applied deformation, while the random errors ranged between 10 and 15%. In fact, the results of this study showed that the strain component in the deformation direction have been underestimated. These errors reduced dramatically if the first three layers of nodes (120 μ m) were removed, leading to systematic and random errors equal to approximately 6% and 7% of the applied deformation (for 1% of deformation).

The DVC is the only method able to explore the internal strain field in bone structures and the SR-microCT tomography imaging provides high-resolution inputs which lead to reduced uncertainties in the method. However, particular the results from this study highlighted the need of evaluating the uncertainties levels for different loading conditions and confirmed the need of optimising the registration and post-processing parameters of the DVC analyses for each application.

Appendix

		Systematic Error (microstrain)						Random Error (microstrain)					
		EPEL	X	Y	Z	XY	YZ	XZ	X	Y	Z	XY	YZ
Specimen 1	1% X	1117	31	107	717	-15	114	1570	369	614	802	578	644
	2% X	1246	20	84	654	-15	101	2794	336	601	1204	527	674
	3% X	1242	0	57	575	12	132	3580	370	598	1583	556	742
	1% Y	36	1182	102	858	-121	52	436	1640	621	904	686	634
	2% Y	15	1138	83	673	-83	41	384	2673	626	1294	718	584
	3% Y	-4	1103	50	491	-71	50	444	3682	636	1787	862	642
	1% Z	15	6	676	27	-90	109	306	301	1354	474	579	614
	2% Z	16	6	955	46	-108	111	344	347	2819	545	787	794
	3% Z	-27	-36	878	5	-44	81	383	395	3677	612	959	928
Specimen 2	1% X	692	100	147	63	-71	53	1478	279	377	577	458	748
	2% X	853	49	94	92	-41	49	2343	289	367	657	466	856
	3% X	980	88	66	-10	-29	94	3102	300	397	750	475	974
	1% Y	37	1465	93	16	-152	26	346	2022	307	564	537	506
	2% Y	32	1449	83	0	-153	28	344	3342	307	639	608	504
	3% Y	25	1235	58	-15	-95	28	377	4181	338	793	798	544
	1% Z	51	111	875	-77	-190	4	343	269	1469	453	472	576
	2% Z	24	93	1116	-81	-176	-10	384	287	2785	487	585	763
	3% Z	4	66	1070	-85	-21	-7	445	316	3717	538	729	933
Specimen 3	1% X	737	92	132	7	-46	233	1592	376	359	636	512	638
	2% X	856	58	98	14	-18	222	2485	373	352	726	498	715
	3% X	991	57	73	1	-17	236	3299	403	359	835	524	832
	1% Y	22	855	118	20	-468	115	414	1503	375	601	607	525
	2% Y	-6	1078	92	33	-437	131	448	2705	379	762	807	564
	3% Y	-19	1005	42	24	-202	139	482	3424	388	917	1064	613
	1% Z	2	36	898	-57	-236	208	393	349	1540	534	611	642
	2% Z	-28	9	1213	-59	-251	230	464	402	3259	637	912	841
	3% Z	-37	2	1120	-50	-164	218	540	471	4293	734	1186	1008
Specimen 4	1% X	674	109	156	-74	-50	31	1462	372	403	649	502	573
	2% X	872	98	140	-72	-41	41	2445	386	421	749	534	655
	3% X	968	92	127	-109	-22	162	3131	399	412	822	545	705
	1% Y	60	947	165	-103	-169	136	438	1705	418	657	653	570
	2% Y	53	1115	142	-105	-164	151	461	2786	434	771	755	601
	3% Y	53	1080	108	-117	-82	159	477	3415	435	878	855	628
	1% Z	46	85	445	-84	-17	114	401	352	1140	546	605	625
	2% Z	32	65	842	-99	3	111	477	432	2725	680	900	920
	3% Z	24	58	703	-110	15	158	499	454	3312	709	969	985

Table 1: Systematic and random errors of each component of strain evaluated for the four specimens, at every tested loading level and direction of compression.

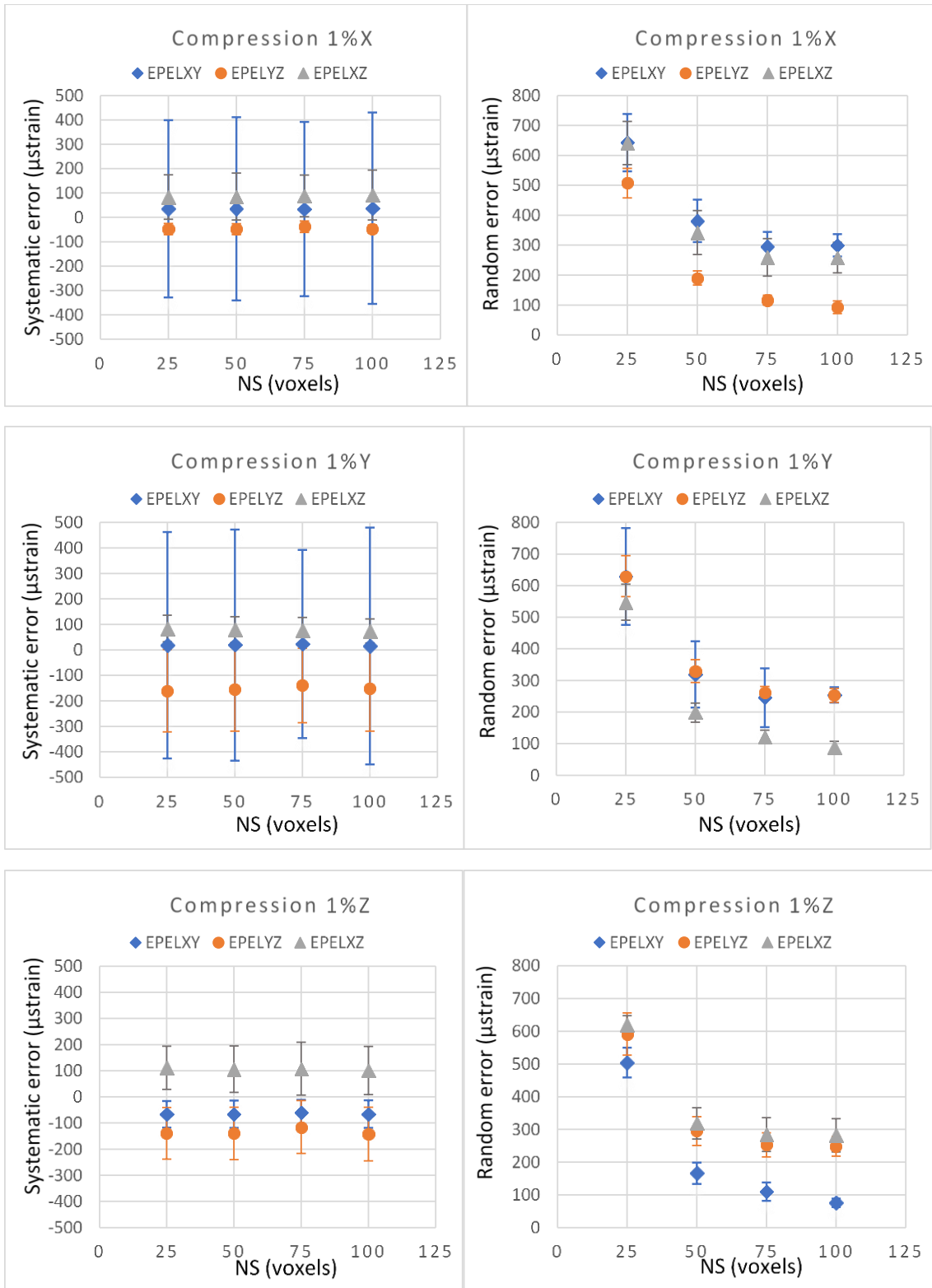


Figure 1: Mean and standard deviation of the systematic and random errors for the shear strain components (EPELXY, EPEPLYZ and EPELXZ) for different NS, computed over the four specimens. The loading conditions were 1% of compression along X, Y and Z.

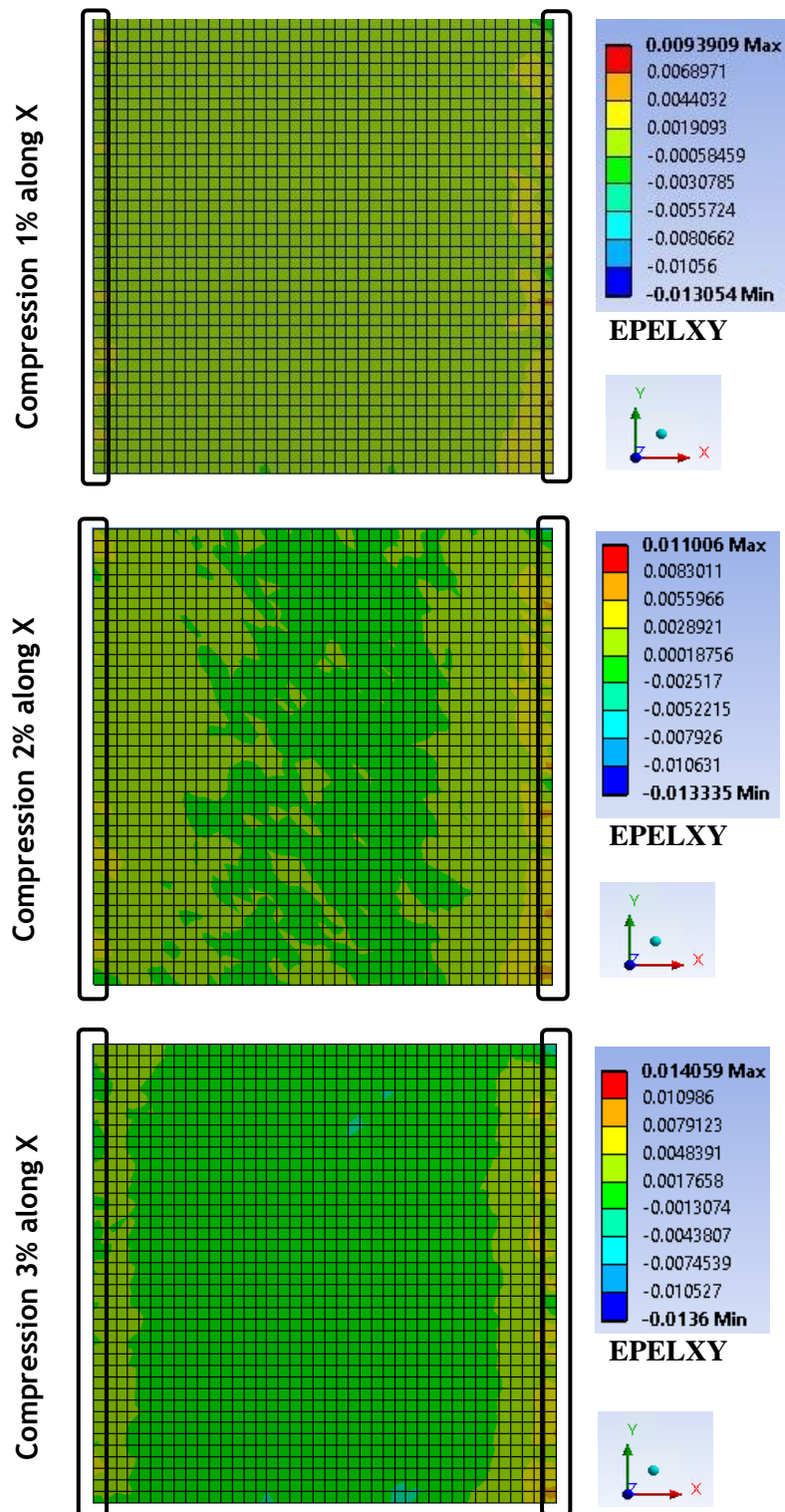


Figure 2: Spatial distribution of the shear strain component along XY ($EPELXY$), for the analysis of 25 voxels of NS, in the middle XY section of the Specimen 1 for 1% (top), 2% (middle) and 3% (bottom) of compression along X. The black boxes highlight the removed layers nodes along the loading direction

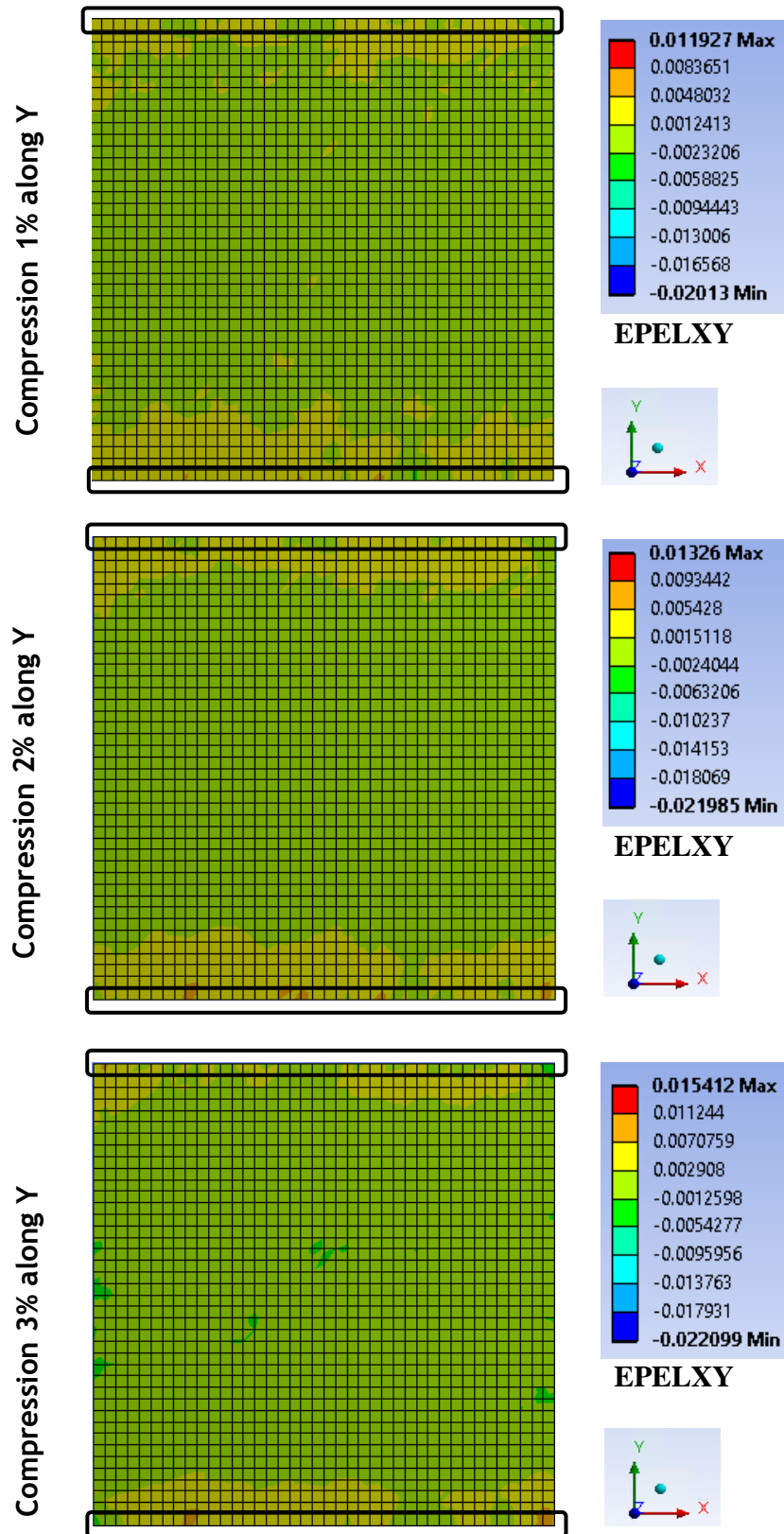


Figure 3: Spatial distribution of the shear strain component along XY (EPELXY), for the analysis of 25 voxels of NS, in the middle XY section of the Specimen 1 for 1% (top), 2% (middle) and 3% (bottom) of compression along Y. The black boxes highlight the removed layers nodes along the loading direction

References

- Barber, D.C., Oubel, E., Frangi, A.F., Hose, D.R., 2007. Efficient computational fluid dynamics mesh generation by image registration. *Med. Image Anal.* 11, 648–662.
- Barber, D.C., Hose, D.R., 2005. Automatic segmentation of medical images using image registration: diagnostic and simulation applications. *J. Med. Eng. Tech.* 29, 53–63.
- Bay, B. K., 2008. Methods and applications of digital volume correlation. *J. Strain Anal. Eng. Des.* 43, 745–760.
- Bay, B.K., Smith, T.S., Fyhrie, D.P., Saad, M., 1999. Digital volume correlation: three-dimensional strain mapping using X-ray tomography. *Exp. Mech.* 39, 217–226.
- Bessho M, Ohnishi I, Matsuyama J, Matsumoto T, Imai K, Nakamura K, 2007. Prediction of strength and strain of the proximal femur by a CT-based finite element method, *J Biomech* 40:1745–1753.
- Bouxsein M.L., Boyd S.K., Christiansen B.A., Guldberg R.E., Jepsen K.J., Müller R., 2010. Guidelines for Assessment of Bone Microstructure in Rodents Using Micro-Computed Tomography. *Journal of Bone and Mineral Research*, 25, 1468–1486.
- Chen, Y., Dall’Ara, E., Sales, E., Manda, K., Wallace, R., Pankaj, P., Viceconti, M., 2017. Micro-CT based finite element models of cancellous bone predict accurately displacement once the boundary condition is well replicated: A validation study. *J. Mech. Behavior Biomed. Mater.* 65, 644–651.
- Christen, D., Levchuk, A., Schori, S., Schneider, P., Boyd, S.K., Muller, R., 2012. Deformable image registration and 3D strain mapping for the quantitative assessment of cortical bone microdamage. *J. Mech. Behavior Biomed. Mater.* 8, 184–193.
- Cristofolini L., 2015. In vitro evidence of the structural optimization of the human skeletal bones. *Journal of Biomechanics* 48, 787–796.
- Cristofolini L., Schileo E., Juszcyk M., Taddei F., Martelli S., Viceconti M., 2010. Mechanical testing of bones: the positive synergy of finite–element models and *in vitro* experiments. *Phil. Trans. R. Soc. A* 368, 2725–2763
- Cristofolini, L., Juszcyk, M., Taddei, F., Viceconti, M., 2009. Strain distribution in the proximal human femoral metaphysis. *Proc. Inst. Mech. Eng. H* 223 (3), 273–288.
- J. Cordey and E. Gautier, 1999. Strain gauges used in the mechanical testing of bones Part h Theoretical and technical aspects. *Injury*. 30 Suppl 1:A7-13.

Costa, M.C., Tozzi, G., Cristofolini, L., Danesi, V., Viceconti, M., and Dall'Ara, E., 2017. Micro Finite Element models of the vertebral body: Validation of local displacement predictions. *PLoS One* 12(7), e0180151.

Cowin, S. C., 2001, *Bone Mechanics Handbook*, CRC Press.

Dall'Ara E., Peña-Fernández M., Palanca M., Giorgi M., Cristofolini L. and Tozzi G., 2017. Precision of Digital Volume Correlation Approaches for Strain Analysis in Bone Imaged with Micro-Computed Tomography at Different Dimensional Levels. *Front. Mater.* 4:31.

Dall'Ara, E., Barber, D., Viceconti, M., 2014. About the inevitable compromise between spatial resolution and accuracy of strain measurement for bone tissue: a 3D zero-strain study. *J. Biomech.* 47, 2956–2963.

Danesi, V., Tozzi, G., Cristofolini, L., 2016. Application of digital volume correlation to study the efficacy of prophylactic vertebral augmentation. *Clin. Biomech.* 39, 14–24.

Dong P., Hauptert S., Hesse B., Langer M., Gouttenoire PJ, Bousson V, Peyrin F., 2014. 3D osteocyte lacunar morphometric properties and distributions in human femoral cortical bone using synchrotron radiation micro-CT images. *Bone* 60, 172–185.

Falcinelli, C., Schileo, E., Baruffaldi, F., Cristofolini, L., Taddei, F., 2016. The effect of computed tomography current reduction on proximal femur subject-specific finite element models. *J. Mech. Med. Biol.* 17 (2), 1750012.

Fresvig T., Ludvigsen P., Steen H., Reikeras O., 2008. Fibre optic Bragg grating sensors: an alternative method to strain gauges for measuring deformation in bone. *Med. Eng. Phys.* 30(1), 104–108.

Gillard, F., Boardman, R., Mavrogordato, M., Hollis, D., Sinclair, I., Pierron, F., Browne, M., 2014. The application of digital volume correlation (DVC) to study the microstructural behaviour of trabecular bone during compression. *J. Mech. Behav. Biomed. Mater.* 29, 480–499.

Grassi, L., Isaksson, H., 2015. Extracting accurate strain measurements in bone mechanics: a critical review of current methods. *J. Mech. Behav. Biomed. Mater.* 50, 43–54.

Hussein, A.I., Barbone, P.E., Morgan, E.F., 2012. Digital volume correlation for study of the mechanics of whole bones. *Procedia IUTAM* 4, 116–125.

Jackman, T. M., DelMonaco, A. M., and Morgan, E. F., 2016. Accuracy of finite element analyses of CT scans in predictions of vertebral failure patterns under axial compression and anterior flexion. *J. Biomech.* 49, 267–275.

- Kim, J.H., Niinomi, M., Akahori, T., Toda, H., 2006. Fatigue properties of bovine compact bones that have different microstructures. *International Journal of Fatigue* 29, 1039-1050.
- Khoo S.W., Karuppanan S., Tan C.S., 2016. A review of surface deformation and strain measurement using two-dimensional digital image correlation. *Metrol. Meas. Syst.*, Vol. 23, No. 3, pp. 461–480.
- Lanyon, L. E., 1993. Osteocytes, strain detection, bone modeling and remodelling. *Calcif. Tissue Int.*, 53(Suppl 1): S102-S107.
- Liu, L., Morgan, E.F., 2007. Accuracy and precision of digital volume correlation in quantifying displacements and strains in trabecular bone. *J. Biomech.* 40, 3516– 3520.
- Madi, K., Tozzi, G., Zhang, Q.H., Tong, J., Cossey, A., Au, A., Hollis, D., Hild, F., 2013. Computation of full-field displacements in a scaffold implant using digital volume correlation and finite element analysis. *Med. Eng. Phys.* 35, 1298–1312.
- Palanca, M., Bodey, A.J., Giorgi, M., Viceconti, M., Lacroix, D., Cristofolini, L., Dall’Ara, E., 2017. Local displacement and strain uncertainties in different bone types by digital volume correlation of synchrotron microtomograms. *J Biomech* 58, 27-36.
- Palanca, M., Tozzi, G., Dall’Ara, E., Curto, M., Innocente, F., Danesi, V., Cristofolini, L., 2016. Digital Volume Correlation can be used to estimate local strains in natural and augmented vertebrae: an organ-level study. *J. Biomech.* 49, 3882–3890.
- Palanca M., Tozzi G., Cristofolini L., 2016. The use of digital image correlation in the biomechanical area: a review. *International Biomechanics*, 3:1, 1-21.
- Palanca, M., Tozzi, G., Cristofolini, L., Viceconti, M., Dall’Ara, E., 2015. 3D local measurements of bone strain and displacement: comparison of three digital volume correlation approaches. *J. Biomech. Eng. (ASME)* 137. 071006-071001/ 071006-071014.
- Pereira A.F., Javaheri B., Pitsillides A.A., Shefelbine S.J., 2015. Predicting cortical bone adaptation to axial loading in the mouse tibia. *J. R. Soc. Interface* 12: 20150590.
- Petrtyl M., Danesova J., 1999. Bone remodeling and bone adaptation. *Acta of Bioengineering and Biomechanics*, 1 pp. 107-116.
- Peyrin F., Dong P., Pacureanu A., Langer M., 2014. Micro- and Nano-CT for the Study of Bone Ultrastructure. *Curr Osteoporos Rep* 12:465–474.
- Roberts, B.C., Perilli, E., Reynolds, K.J., 2014. Application of the digital volume correlation technique for the measurement of displacement and strain fields in bone: a literature review. *J. Biomech.* 47, 923–934.

Rosa, N., Simoes R., Magalhães F.D., Marques A.T., 2015. From mechanical stimulus to bone formation: A review. *Med Eng Phys.* 37(8): 719-28.

Tozzi, G., Dall'Ara, E., Palanca, M., Curto, M., Innocente, F., Cristofolini, L., 2017. Strain uncertainties from two DVC approaches in prophylactically augmented vertebrae: local analysis on bone and bone-cement microstructures. *J. Mech. Behavior Biomed. Mater.* 67, 117–126.

Viceconti, M., Olsen, S., Nolte, L.-P., Burton, K., 2005. Extracting clinically relevant data from finite element simulations. *Clin. Biomech.* 20 (5), 451–454.

ZaueI, R., Yeni, Y.N., Bay, B.K., Dong, X.N., Fyhrie, D.P., 2006. Comparison of the linear finite element prediction of deformation and strain of human cancellous bone to 3D digital volume correlation measurements. *J. Biomech. Eng.* 128, 1–6.

Zhu, M. L., Zhang, Q. H., Lupton, C., and Tong, J., 2016. Spatial resolution and measurement uncertainty of strains in bone and bone-cement interface using digital volume correlation. *J. Mech. Behav. Biomed. Mater.* 57, 269–279.